Investigating the role of microcalcification in Alzheimer's disease progression

Jing Xue

University College London

Medical physics and biomedical engineering

It is submitted to University College London (UCL) in partial fulfilment of the Doctor of Philosophy degree.

Primary supervisor: Sergio Bertazzo

Secondary supervisor: Imre Lygenel

Thesis submission date: Nov 2025

Table of Contents

Declaration

I, Jing Xue, confirm that the work presented in this thesis is my own. Where information has been derived from other sources, I confirm that this has been indicated in the thesis.

The research was carried out at University College London under the supervision of Sergio Bertazzo in the Medical Physics and Biomedical Engineering department. This thesis has not been submitted in whole or in part for any degree or qualification at any other university or institution.

Any work of others used in this thesis has been duly acknowledged, and all sources of information have been specifically referenced. Where published work by others has been cited or referred to, it has been appropriately credited and is indicated in the text and bibliography.

- **Data sources:** The primary dataset was collected by me. MSc students collected a portion of the data presented in Figure 15 under my supervision in the laboratory, where I served as the second supervisor.
- **AI:** ChatGPT was used for support with the structure construction and proofreading.
- **Other:** Parts of this work were developed in conversations with my supervisors, as listed in the Acknowledgements.

Signed: Jing Xue
Date: 17th Nov 2025

Acknowledgements

This thesis represents the culmination of many years of hard work, dedication, and support from numerous individuals and institutions. I want to extend my sincere thanks to the individuals who made this journey possible.

First and foremost, I would like to express my most profound appreciation to my supervisors, **Sergio Bertazzo** and **Imre Lengyel**, for their unwavering guidance, mentorship, and patience throughout this process. Their insightful feedback, encouragement, and willingness to push me beyond my limits have been instrumental in shaping this work. I am incredibly fortunate to have had the opportunity to work under their tutelage.

I would also like to thank my thesis committee for their valuable suggestions, constructive criticism, and encouragement. Their expertise has dramatically enriched the quality of this research, and I am deeply grateful for the time and effort they invested in reviewing my work.

Special thanks go to my research group and colleagues, particularly **Elena Tsolaki,** for the stimulating discussions, collaborative spirit, and countless moments of camaraderie that made this journey more enjoyable. Your support has been invaluable both inside and outside the lab.

On a personal note, I owe my family a tremendous debt of gratitude. To my parents, **Zhenggao Xue** and **Lili Zhang,** for their endless love, encouragement, and belief in my abilities. A heartfelt thank you to my partner, **Gloria**, for her support, understanding, and encouragement throughout the thesis writing and revision process.

Abstract

Brain calcification is an emerging feature of Alzheimer's disease (AD), but its pathological significance remains largely unexplored. While AD research has predominantly focused on amyloid plaques and neurofibrillary tangles, the direct investigation of inorganic mineral deposits remains limited. This study employs materials science techniques to characterise brain calcification and assess its potential role in AD progression.

Using Scanning Electron Microscopy (SEM), Energy-Dispersive X-ray Spectroscopy (EDS), and immunofluorescence co-localisation, calcifications were identified in neuron-rich regions, primarily composed of calcium phosphate in spherical and fibrillar forms. Quantitative analysis demonstrated a clear correlation between calcification and Braak staging, with the basal ganglia and hippocampus exhibiting the most pronounced increases in late-stage AD. Simulated Body Fluid (SBF) experiments successfully replicated AD-like mineralisation under physiological conditions. These in vitro models indicated that tau phosphorylation and incubation time influence the extent and morphology of mineral deposition, suggesting a mechanistic link between protein pathology and mineral formation. Co-localisation studies further revealed a strong spatial association between calcification and phosphorylated tau (pTau) in early-stage AD. However, this correlation declined markedly in Braak stages V–VI, implying a shift towards calcification as a potentially independent pathological feature in advanced disease.

Collectively, these findings suggest that brain microcalcification is not merely incidental but may actively contribute to AD progression. This research underscores the value of incorporating materials science techniques in neuropathology studies and supports the development of novel diagnostic and therapeutic strategies targeting mineralisation processes in Alzheimer's disease.

Impact statement

This research makes a significant contribution to the understanding of Alzheimer's Disease (AD) by uncovering the previously underappreciated role of micro mineralisation in disease pathology. Moving beyond the conventional focus on β-Amyloid plaques and neurofibrillary tangles (NFTS), this study demonstrates that calcium-dominated mineral deposits are present in early stages of AD, frequently preceding the formation of NFTS and Aβ plaques. Through the use of advanced imaging and biochemical techniques, these deposits were characterised and shown to be closely associated with hyperphosphorylated tau protein aggregation, a key driver of neurodegeneration. In addition, the extent of calcification was quantitatively assessed across multiple brain regions using the AD pathological system, revealing progressive increases in calcification with advancing Braak stages.

These findings offer a novel perspective on AD pathogenesis, suggesting that mineralisation may play a critical role in both the initiation and exacerbation of disease progression. By identifying mineralisation-related biomarkers, this research provides a foundation for the development of urgently needed diagnostic tools, as global AD prevalence is projected to triple in the coming decades. Moreover, the observed interplay between mineralisation and tau pathology highlights a promising therapeutic target. Interventions aimed at disrupting mineral accumulation may prove especially effective in early Braak stages.

This study not only enhances our understanding of Alzheimer's disease (AD), but also underscores the value of a comprehensive, interdisciplinary approach to studying neurodegenerative diseases. By integrating knowledge and methodologies from neuroscience, biochemistry, and materials science, this work sets the stage for future cross-disciplinary investigations. The insights gained have the potential to transform both the diagnosis and treatment of AD and related disorders, ultimately contributing to more effective therapeutic strategies and improved patient outcome.

Scientific output

Publications

Tsolaki, E., Csincsik, L., **Xue, J**., Lengyel, I., & Bertazzo, S. (2022). Nuclear and cellular, micro and nano calcification in Alzheimer's disease patients and correlation to phosphorylated Tau. Acta Biomaterialia, 143, 138-144. https://doi.org/10.1016/j.actbio.2022.03.003

Keeling, G. P., Baark, F., Katsamenis, O. L., **Xue, J.**, Blower, P. J., & Bertazzo, S. (2023). 68Ga-bisphosphonates for the imaging of extraosseous calcification by positron emission tomography. Scientific Reports, 13(1), 1-13. https://doi.org/10.1038/s41598-023-41149-7

Poster presentation

Xue J, Mineralisation-induced tau phosphorylation: The potential mechanism of Alzheimer's Disease, 2022 Biomineralisation Conference GRC

Oral presentation

Xue J, Mineralisation-induced tau phosphorylation: The potential mechanism of Alzheimer's Disease, 2022 Biomineralisation Seminar GRS

Abbreviations

AD - Alzheimer's disease
NFTS - Neurofibrillary Tangles
WHO - World Health Organisation
Aβ - Amyloid-beta plaques
CAA - Cerebral Amyloid Angiopathy
APP - Amyloid Precursor Protein
GSK-3β - Glycogen Synthase Kinase-3β
CDK5 - Cyclin-Dependent Kinase 5
PP2A - Protein Phosphatase 2A
PHFS - Paired Helical Filaments
MCI - Mild Cognitive Impairment
CDR - Clinical Dementia Rating Scale
CDR-SB - CDR Sum of Boxes
FAQ - Functional Activities Questionnaire
ADAS-Cog - Alzheimer's Disease Assessment Scale – Cognition Subscale
MMSE - Mini-Mental State Exam
CAA - Cerebral Amyloid Angiopathy
PET - Positron Emission Tomography
CSF - Cerebrospinal Fluid
BBB - Blood-Brain Barrier
CT - Computed Tomography
MRI - Magnetic Resonance Imaging
SWI - Susceptibility-Weighted Imaging
SEM - Scanning Electron Microscopy
EDS - Energy-Dispersive X-ray Spectroscopy
pTau - hyperphosphorylation of Tau
FFPE - Formalin-Fixed Paraffin-Embedded
FEGS - Field Emission Guns
SE - Secondary Electron
BSE - Backscattered Electron
DDC Map - Density-Dependent Colour Map
TEM - Transmission Electron Microscopy
SAED - Selected Area Electron Diffraction
PMT - Photomultiplier Tube
CCD - Charge-Coupled Device
rSBF – revised Simulated Body Fluid

Chapter 1: Introduction

1.1 Background and motivation

1.1.1 Prevalence and Significance of Dementia and Alzheimer's Disease

Alzheimer's disease (AD) is the most common form of dementia, accounting for approximately 60-70% of all dementia cases worldwide [1]. It is a progressive neurodegenerative disorder characterised by the gradual deterioration of cognitive functions, including memory, reasoning, and behaviour [2-4]. The disease is named after Dr Alois Alzheimer, who described its pathological features in 1906, including amyloid plaques and neurofibrillary tangles (NFTS) [5]. Over a century later, AD remains a significant public health challenge, with no cure or effective treatment to halt its progression [6, 7].

The global burden of AD is staggering. According to the World Health Organisation (WHO) and the Alzheimer's Association, over 55 million people were living with dementia in 2020, and this number is projected to nearly triple to 139 million by 2050 [8, 9]. The rapid ageing of the global population is a key driver of the rising prevalence of AD, as advancing age remains the most significant known risk factor. Currently, a new case of dementia is diagnosed every three seconds worldwide, underscoring the urgency of addressing this growing public health crisis [6, 10, 11].

The impact of AD extends far beyond its health implications. Economically, the costs of dementia care are immense. In 2021, the total cost of Alzheimer's and other dementias in the United States alone was estimated at 355 billion. Projections suggest that this figure will exceed 1.1 trillion by 2050 [1, 2, 12]. These include direct medical expenses, long-term care, and the significant burden on unpaid caregivers, often family members. Caregivers face emotional, physical, and financial strain, with many experiencing burnout, depression, and reduced quality of life [9, 13, 14].

At a societal level, AD places immense pressure on healthcare systems and social services. This burden is particularly pronounced in low- and middle-income countries (LMICs), where approximately 60% of dementia cases currently occur [15, 16]. These regions often face significant challenges due to limited healthcare infrastructure, insufficient trained personnel, and lower public awareness. By 2050, the proportion of dementia cases in LMICs is expected to rise to 70%, further exacerbating global disparities in access to diagnosis, treatment, and long-term care [8].

On a personal level, AD profoundly affects individuals and their families. Patients experience a gradual loss of independence, memory, and identity, while caregivers endure emotional distress and financial hardship. It gradually robs individuals of their independence, dignity, and quality of life, making it one of the most devastating and emotionally taxing conditions of the time [14, 17, 18].

The pathological features of AD are well-documented and include amyloid-beta (Aβ) plaques, neurofibrillary tangles (NFTS), synaptic loss, neuroinflammation, and cerebral amyloid angiopathy (CAA) [19-22]. These hallmarks interact in complex ways to drive disease progression. The extracellular Amyloid-beta plaques consist of aggregated Aβ peptides derived from the abnormal cleavage of amyloid precursor protein (APP) [23, 24]. Aβ plaques disrupt synaptic communication, trigger neuroinflammation, and induce oxidative stress, ultimately leading to neuronal damage and death [22]. Neurofibrillary tangles (NFTS) are intracellular aggregates of hyperphosphorylated tau proteins. In healthy neurons, tau stabilises microtubules, which are essential for intracellular transport. In AD, abnormal phosphorylation causes tau to detach from microtubules, forming insoluble tangles that disrupt neuronal function and lead to cell death [19, 25, 26].

Despite decades of research on Aβ plaques and NFTS, the precise mechanisms underlying their formation and contribution to AD remain unclear. Moreover, therapies targeting these hallmarks have shown limited success, underscoring the need to explore alternative pathological mechanisms, such as mineralisation.

1.1.2 Mineralisation in Biological Systems and the Brain

Mineralisation is a natural biological process that involves the deposition of minerals, such as calcium, iron, and zinc, in tissues. While mineralisation is essential for developing and maintaining complex tissues like bones and teeth [27-29], abnormal mineral deposition in soft tissues—known as pathological mineralisation—is associated with various diseases, including cardiovascular disorders, kidney stones, and neurodegenerative conditions like AD. [30-33]

In the brain, mineralisation can occur in several forms, each with distinct implications for health and disease:

- **Dystrophic Calcification**: This type of calcification occurs in damaged or necrotic tissue and is often associated with brain injury, stroke, or neurodegenerative diseases like AD [34]. In AD, dystrophic calcification is frequently observed around Aβ plaques and in regions of neuronal death, suggesting a link between mineral deposition and disease pathology [29].
- **Metastatic Calcification**: This form results from systemic imbalances in calcium metabolism, such as those caused by hyperparathyroidism or renal failure [32, 35, 36]. While less common in the brain, metastatic calcification can occur in normal tissues and contribute to vascular abnormalities and neuronal damage [37-39].
- **Idiopathic Calcification**: Idiopathic calcification occurs without an underlying cause and is often linked to genetic factors. For example, Fahr's disease is a rare genetic disorder characterised by extensive calcifications in the basal ganglia and other brain regions, leading to neurological and psychiatric symptoms [40-42].
- **Physiological Calcification**: This benign process occurs naturally with ageing and is commonly observed in structures like the pineal gland and choroid plexus [43, 44]. While physiological calcifications are generally harmless, they can be helpful markers in neuroimaging studies [45, 46].

Idiopathic and physiological calcifications are classified as pathological calcification as they are initiated due to genetic or aging rather than any systematical and external damage caused reason. Emerging evidence suggests that pathological mineralisation plays a significant role in AD. Mineral deposits, particularly those dominated by calcium, have been identified in key brain regions affected by AD, such

as the basal ganglia, hippocampus and cortex [42, 46, 47]. These regions are critical for memory and cognitive function, and their involvement in AD underscores the potential importance of mineralisation in disease progression [48].

Several mechanisms have been proposed to explain how mineralisation contributes to AD pathology:

- **Iron Accumulation**: Iron deposits in the brain can generate reactive oxygen species (ROS), leading to oxidative stress and causing neuronal damage [49-51].
- **Ferroptosis:** Iron-mediated programmed cell death is characterised by the accumulation of toxic lipid reactive oxygen species (ROS), resulting from dysregulated iron metabolism [52, 53].
- **Calcium Dysregulation**: Disrupted calcium homeostasis can impair neuronal signalling and promote tau hyperphosphorylation, accelerating NFT formation [54, 55]
- **Interaction with Aβ Plaques**: Mineral deposits (such as calcium and iron) may interact with Aβ peptides, enhancing their aggregation and toxicity [51, 56, 57]

1.2 Aims and objectives

Despite growing interest in Alzheimer's disease (AD) pathology, the role of brain mineralisation remains significantly underexplored. Most research has concentrated on amyloid-beta (Aβ) plaques and neurofibrillary tangles (NFTs), leaving critical gaps in our understanding of how mineralisation may contribute to neurodegeneration. Within the context of AD-related mineralisation, iron accumulation has received increasing attention, often regarded as a co-factor in the development of dementia. In contrast, brain calcification has received less attention and is often dismissed as an incidental or age-related phenomenon. The few existing studies investigating calcification in AD have primarily focused on its presence, with limited exploration of underlying mechanisms or pathological significance.

This study aims to address these knowledge gaps by systematically examining the relationship between microcalcification and pathological AD progression. Through detailed characterisation of calcification particles in post-mortem brain tissue, this research seeks to uncover potential roles for calcification in disease pathology and evaluate its potential as a novel biomarker or therapeutic target in Alzheimer's disease. The main aim of this work is to quantify microcalcification in AD brains and investigate its relationship with disease severity, tissue architecture, and associated protein pathology. Further to provide new evidence regarding the potential significance of brain calcification and its possible relevance as a biological feature, potential marker, or pathological indicator within the context of Alzheimer's disease.

1.3 Thesis outline

Chapter 2: The key background information will first be presented. This includes an overview of Alzheimer's disease pathology, the phenomenon of brain mineralisation, and the current clinical landscape of AD diagnosis and treatment. These elements provide the foundation necessary to understand the motivation and relevance of the study. Additionally, a brief discussion will highlight the existing research gap that this work aims to address.

Chapter 3: This chapter outlines the application of various analytical techniques used to investigate pathological calcification, with a particular emphasis on the optimised sample preparation protocols developed for this study. It will introduce the fundamental principles of scanning and transmission electron microscopy, highlighting the type of information these methods can reveal about mineral composition, morphology, and localisation within biological tissues. Detailed protocols for preparing samples for direct physicochemical characterisation of calcifications in situ will be presented. In addition, the chapter will cover the use of biochemical methods for protein identification—specifically immunofluorescence staining—and explain their relevance in the context of studying mineral–protein interactions. Optimised protocols for preparing samples for co-localisation analysis of minerals and proteins will also be discussed.

Chapter 4: Electron microscopy-based mineral characterisation was performed on all brain tissue samples of young donors and age-matched donors and diagnosed patients to validate and expand upon findings previously reported in the literature. This was followed by quantitative analysis of calcification levels, assessed in relation to both chronological age and pathological progression as defined by Braak staging. The statistical approaches and quantification methods used to evaluate these correlations are also described in this chapter.

Chapter 5: A simulation model was established to investigate the formation of brain calcification under physiological conditions. Using Simulated Body Fluid (SBF), both brain tissue and tau protein samples were incubated to explore potential triggers of mineralisation. Microscopy techniques, including SEM and TEM, were employed to examine the morphology and distribution of calcium phosphate deposits. Finally, how protein composition and tissue-specific factors contribute to the development of pathological calcification in Alzheimer's disease are discussed.

Chapter 6: This section presents the results of electron microscopy analyses focusing on the spatial localisation of calcification, phosphorylated tau (pTau) proteins, and neurons in brain tissues from age-matched donors and Alzheimer's disease patients. Based on these observations, the potential association between mineral deposits and Alzheimer’s pathology is assessed. In addition, the co-localisation patterns of pTau and calcification are compared across clinical and pathological groups.

Chapter 7: This final chapter offers a concise summary of the key findings, outlines the study’s limitations, and highlights its scientific contributions. It also includes a brief discussion on potential directions for future research.

Appendices: The supplementary information referenced in this thesis includes detailed young control group information. Additionally, collaborative work titled "Nuclear and cellular, micro- and nano calcification in Alzheimer’s disease patients and correlation to phosphorylated Tau", conducted in partnership with Elena Tsolaki, is summarised. This project was carried out in parallel with the research discussed in the main body of the thesis.

Chapter 2: Background

2.1 Pathology of Alzheimer's Disease

2.1.1 Brain Anatomy and Alzheimer's Disease

The human brain is a highly complex organ responsible for cognition, memory, emotion, and motor coordination. It is anatomically divided into four primary lobes (frontal, parietal, temporal, and occipital) (Fig.1(a)), each responsible for distinct but interconnected roles [58].

The frontal lobe, located at the anterior part of the brain, plays a central role in higher-order executive functions, including decision-making, problem-solving, and motor control. It also affects speech production and aspects of personality and social behaviour [10, 59]. The parietal lobe, situated in the upper middle region of the brain, processes somatosensory information, such as touch, pain, temperature, and proprioception. It also contributes to spatial orientation and the integration of sensory input for motor responses [57–59]. The temporal lobe, located laterally near the ears, is essential for auditory processing, language comprehension, and the regulation of emotion. It contains several key substructures—including the hippocampus and amygdala—which are vital for memory formation and emotional memory encoding [60, 61]. Finally, the occipital lobe, positioned at the posterior of the brain, is primarily responsible for visual processing, including object recognition, colour perception, and spatial analysis [62].

In Alzheimer's disease (AD), neurodegeneration follows a predictable spatial pattern, progressively affecting specific brain regions. The hippocampus (Fig. 1(b))—a core structure for consolidating short-term to long-term memory—is among the first areas to exhibit atrophy, often correlating with early clinical symptoms such as memory loss and disorientation [63, 64]. As the disease advances, it leads to widespread cortical atrophy (Fig. 1(c)), particularly in the temporal and parietal lobes, driven by hallmark pathological features such as amyloid-beta (Aβ) plaques, neurofibrillary tangles (NFTs), and sustained neuroinflammation [6, 19, 65–67]. These pathological changes compromise synaptic integrity, disrupt neural connectivity, and ultimately result in significant neuronal loss.

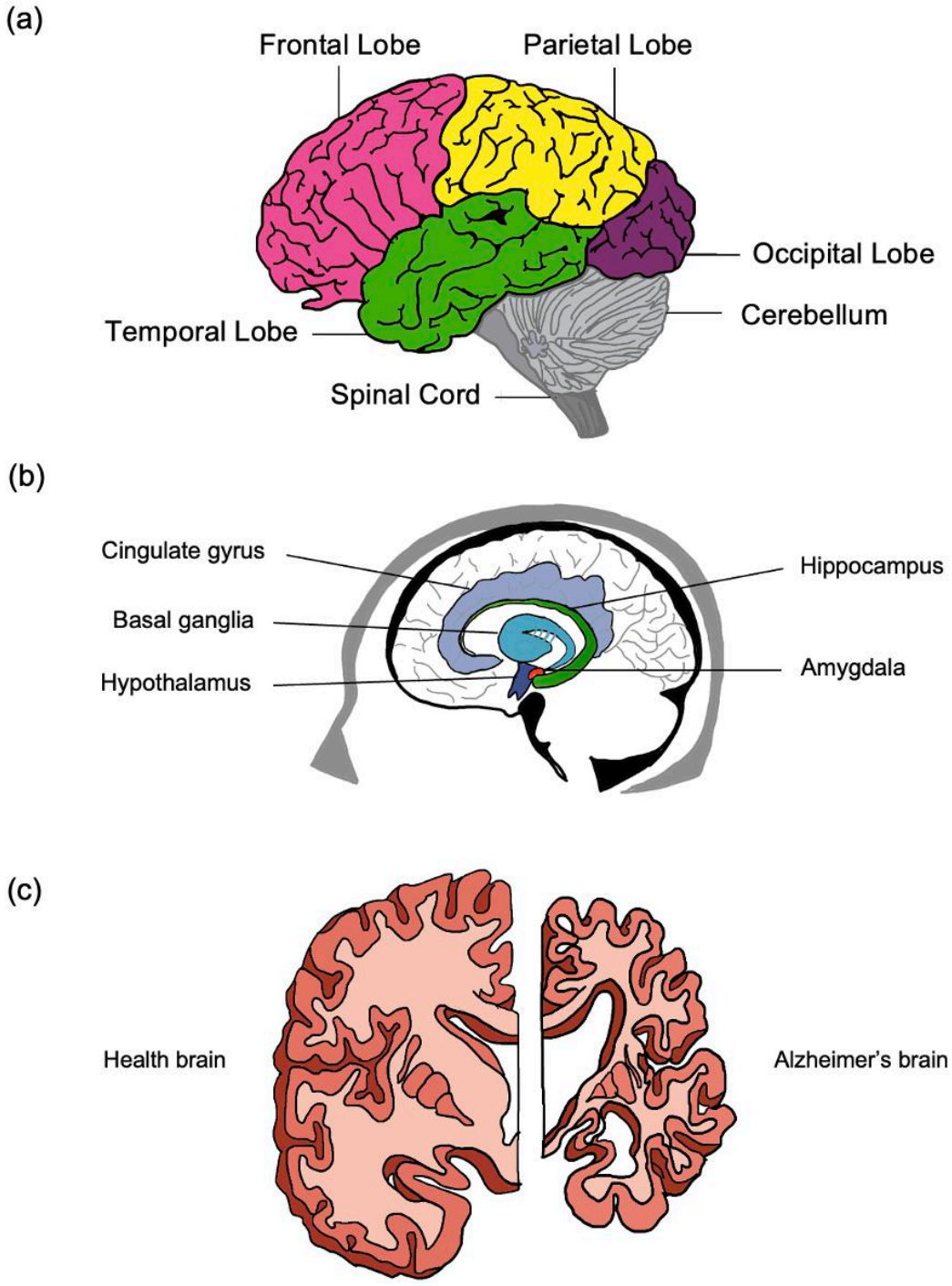

Figure 1. Graphic illustration of brain anatomy. (a) Location indication of the four brain lobes. (b) Structure of the limbic system. (c) The comparison of a healthy brain and an Alzheimer's brain

2.1.2 Role of tau phosphorylation in disease mechanisms

Tau proteins, encoded by the MAPT gene located on chromosome 17, play a vital role in stabilising microtubules within neurons, facilitating intracellular transport and maintaining neuronal structure [18, 19]. Through alternative mRNA splicing, six isoforms of tau are expressed in the adult human brain, differing in the number of microtubule-binding domains and N-terminal inserts [60]. Structurally, tau is an intrinsically disordered protein, which allows it to remain flexible and interact dynamically with various binding partners. The microtubule-binding domains, located near the C-terminal region, are essential for stabilising axonal microtubules, whereas the N-terminal region is involved in cellular signalling and interactions with other cytoskeletal components [61]. This structural versatility is critical for maintaining neuronal morphology and function [62].

In healthy brains, tau phosphorylation is tightly regulated by kinases and phosphatases, ensuring proper microtubule assembly and function [63, 64]. However, tau becomes hyperphosphorylated in AD, leading to its detachment from microtubules and subsequent aggregation into NFTS [65, 66]. This hyperphosphorylation is driven by dysregulated kinase activity, such as glycogen synthase kinase-3β (GSK-3β) and cyclin-dependent kinase 5 (CDK5), and impaired phosphatase function, such as protein phosphatase 2A (PP2A) [67-70].

Hyperphosphorylated tau loses its ability to stabilise microtubules, disrupting neuronal transport and leading to synaptic dysfunction and cell death [21, 71, 72]. The accumulation of NFTS correlates strongly with cognitive decline and disease progression, making tau pathology a central focus of AD research [20, 22, 65]. Understanding tau phosphorylation and aggregation mechanisms is essential for developing targeted therapies to halt or reverse AD progression.

Figure 2 comprehensively illustrates microtubule structure in both healthy and pathological states. In Figures 2a and 2b, microtubules are depicted under conditions of normal tau phosphorylation [63, 73], where tau proteins bind to microtubules and stabilise their structure, ensuring proper neuronal function and intracellular transport [72-74]. In contrast, Figure 2c illustrates the pathological state of hyperphosphorylation, where tau proteins become excessively phosphorylated, losing their ability to bind to microtubules. This destabilises the microtubule network, aggregating hyperphosphorylated tau into paired helical filaments (PHFS), which further assemble into neurofibrillary tangles (NFTS) [75]. These NFTS disrupt intracellular transport,

impair synaptic function, and ultimately contribute to neuronal dysfunction and cell death, which are hallmark features of AD.

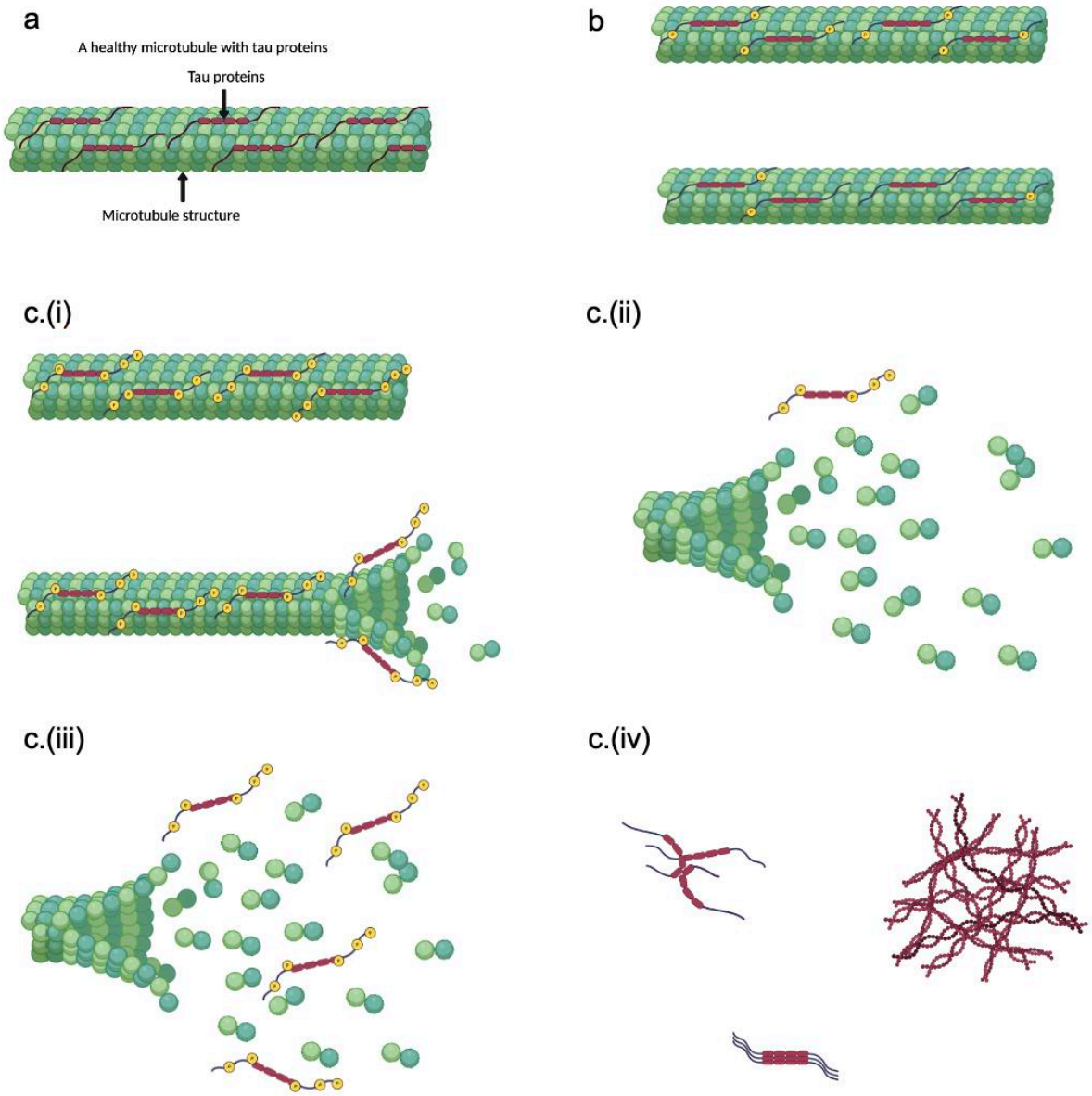

Figure 2. Microtubule structure with different forms of tau proteins. (a) Healthy microtubule with tau protein. (b) The microtubule structure, comprising phosphorylated protein and attached proteins, is under normal phosphorylation conditions. (c) The process of structural changes occurs when the microtubule structure attaches to hyperphosphorylated tau proteins. (i) Attached are hyperphosphorylated tau proteins dissociating the microtubule structure. (ii) In the initial disassembly phase, the microtubule structure breaks down, and the hyperphosphorylated tau protein detaches from the microtubule structure. (iii) In the further disassembling stage, more hyperphosphorylated tau protein loses stability and detaches from the dissociated microtubule. (iv) Detached hyperphosphorylated tau protein aggregates into paired helical filaments, the primary constituents of neurofibrillary tangles.

2.1.3 Disease progression and severity

2.1.3.1 Pathological Assessment of AD Severity

The progression and severity of Alzheimer's disease (AD) are highly variable among individuals, influenced by a complex interplay of genetic, biochemical, and environmental factors [76-79]. This variability poses significant challenges in accurately assessing disease severity and predicting clinical outcomes. Pathologists and clinicians employ different approaches to evaluate AD progression, with pathologists focusing on anatomical and histological changes in the brain while clinicians rely on cognitive and functional assessments [80, 81]. Understanding the mechanisms underlying disease progression, including the roles of tau pathology, amyloid-beta plaques, and emerging factors such as brain mineralisation, is critical for improving diagnostic accuracy and developing effective therapeutic interventions [82-86].

The pathological assessment of AD severity is primarily based on the presence and distribution of two hallmark lesions: neurofibrillary tangles (NFTS) and amyloid-beta (Aβ) plaques. NFTS comprise hyperphosphorylated tau proteins that aggregate into paired helical filaments, while Aβ plaques result from the extracellular accumulation of amyloid-beta peptides. The Braak staging system, developed by Heiko Braak and Eva Braak in the early 1990s, is widely used to classify AD progression based on the anatomical spread of tau pathology [87-89].

The Braak stages are divided into six phases: Stages I-II (Transentorhinal Stages), where the tau pathology is initially observed in the transentorhinal region, with limited hippocampus involvement, as shown in Figure 3a. These early stages are often asymptomatic, as the pathology has not yet spread to critical areas for memory and cognition [89, 90]. Figure 3b indicates that the tau pathology progresses to the entorhinal cortex and hippocampus, regions essential for memory formation at Stages III-IV (Limbic Stages). Patients in these stages typically exhibit mild cognitive impairment (MCI) and early signs of memory loss [91, 92]. At Stages V-VI (Neocortical Stages), shown in Figure 3c, tau pathology spreads to the neocortex, affecting areas responsible for higher cognitive functions such as language, reasoning, and decision-making. Patients in these advanced stages experience severe dementia and functional decline.

While the Braak staging system provides a framework for understanding tau pathology progression, it does not consistently correlate with clinical symptoms. For example, some individuals with advanced Braak stages (V-VI) exhibit only mild cognitive impairment, while others with earlier stages (III-IV) show severe dementia [6, 80]. This discrepancy suggests that additional factors, such as amyloid-beta pathology, vascular changes, and brain mineralisation, may influence disease progression and symptom severity [82, 93].

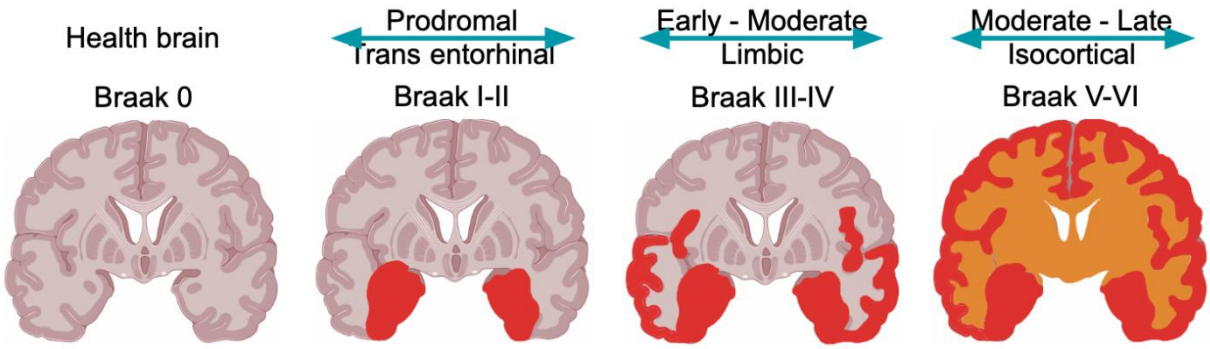

Figure 3. Tau pathology with disease progression at corresponding Braak stages. The colour represents the severity of tau pathology; red represents the most severe region. (a) Braak stage I-II, (b) Braak stage III-IV, (c) Braak stage V-VI.

2.1.3.2 Clinical Assessment of AD Severity

Clinicians assess AD severity using standardised tools that evaluate cognitive and functional performance. The Clinical Dementia Rating Scale (CDR), developed by Charles Hughes and colleagues, is one of the most widely used instruments for assessing dementia severity [94, 95]. The CDR evaluates six domains: memory, orientation, judgment and problem-solving, community affairs, home and hobbies, and personal care. Each domain is rated on a scale from 0 (no impairment) to 3 (severe impairment), and the scores are combined to generate a composite CDR score. An extension of the CDR, the CDR Sum of Boxes (CDR-SB), provides a more detailed assessment by summing the severity ratings across all domains, offering a scale from 0 to 18 [94].

Other assessment tools are commonly used in clinical settings. The Functional Activities Questionnaire (FAQ) assesses the ability to manage finances, shop, and prepare meals. The Alzheimer's Disease Assessment Scale – Cognition Subscale (ADAS-Cog) evaluates cognitive functions such as memory, language, and praxis and is considered a gold standard for assessing the efficacy of anti-dementia treatments.

The Mini-Mental State Exam (MMSE) is a brief screening tool that evaluates orientation, memory, attention, language, and visuospatial skills.

These tools provide valuable insights into the cognitive and functional impairments associated with AD, but they do not directly measure the underlying pathological changes. Integrating clinical assessments with neuroimaging and biomarker data could enhance the accuracy of Alzheimer's disease (AD) diagnosis and staging[6, 7, 45, 96].

2.1.3.3 Factors Influencing Disease Progression

A combination of genetic, biochemical, and environmental factors influences the progression of AD. Genetic mutations in genes such as APP, PSEN1, and PSEN2 are associated with early-onset familial AD, while the APOE ε4 allele is a significant risk factor for late-onset sporadic AD [4, 19]. Biochemical factors, including the accumulation of Aβ plaques and NFTS, drive neuronal dysfunction and cell death. Chronic inflammation, oxidative stress, and mitochondrial dysfunction further exacerbate disease progression [78].

Emerging evidence suggests that vascular changes, including cerebral amyloid angiopathy (CAA) and calcification, may also contribute to AD progression [22, 51]. Vascular calcification, characterised by the deposition of calcium phosphate in blood vessels, reduces cerebral blood flow and contributes to ischemic injury [38, 97, 98]. While vascular calcification has been observed in AD brains, its exact role in disease progression remains unclear. Similarly, brain mineralisation, particularly micro-calcification, has been linked to AD pathology, but further research is needed to elucidate its contribution to disease progression [99].

2.1.3.4 Discrepancies Between Pathological and Clinical Staging

One key challenge in AD research is the discrepancy between pathological and clinical staging. While the Braak staging system provides a detailed framework for assessing tau pathology, it does not consistently correlate with clinical symptoms. Studies have shown that individuals with similar Braak stages can exhibit wide variability in cognitive decline and dementia severity. This variability may be influenced by age, comorbidities, and cognitive reserve, which refers to the brain’s ability to compensate for pathology through alternative neural networks [79, 89].

Recent research has also highlighted the limitations of relying solely on tau pathology to predict clinical outcomes. For example, positron emission tomography (PET) imaging studies have shown that Aβ-positive individuals are likelier to advance Braak stages, suggesting that Aβ pathology may drive tau spread [22, 100-102]. However, the relationship between Aβ and tau pathology is complex, and additional factors, such as brain mineralisation, may play a role in modulating disease progression [79, 103, 104].

There is a growing need for integrated approaches that combine pathological, clinical, and biomarker data to address the limitations of current staging systems. Advanced neuroimaging techniques, such as tau PET and amyloid PET, enable the in vivo assessment of tau and Aβ pathology, providing valuable insights into disease progression. Similarly, emerging biomarkers, such as plasma and cerebrospinal fluid (CSF) levels of Aβ and tau, offer non-invasive methods for monitoring disease progression [49, 103].

Developing a classification system based on brain mineralisation could provide new insights into AD progression. For example, quantifying the extent and distribution of calcified deposits in the brain and correlating these findings with clinical symptoms could improve diagnostic accuracy and guide therapeutic interventions [105]. However, further research is needed to validate the role of brain mineralisation in AD and develop standardised methods for its assessment.

2.2 Brain mineralisation

2.2.1 Biochemical Pathways Linking Mineralisation to AD

Brain mineralisation involves the accumulation of minerals, primarily calcium and iron, in brain tissues. These minerals play essential physiological roles but can become pathological when their homeostasis is disrupted. Calcium, for instance, is a critical signalling molecule involved in neurotransmitter release, synaptic plasticity, and neuronal excitability [27, 32, 106]. Under normal conditions, channels, transporters, and binding proteins tightly regulate intracellular calcium levels. However, in AD, calcium dysregulation contributes to neuronal dysfunction and cell death [54, 55, 107].

Several mechanisms, including disruption of calcium homeostasis, oxidative stress, inflammation, etc., drive the brain's pathological accumulation of calcium. In genetic AD cases, mutations such as APP and PSEN1 alter calcium-signalling pathways, leading to elevated intracellular calcium levels [84, 86]. This calcium overload promotes the formation of Aβ plaques and NFTS, which are hallmarks of AD [44, 108, 109]. Additionally, increased oxidative stress enhances the permeability of cellular membranes to calcium [19, 110, 111]. Elevated intracellular calcium levels can react with intracellular phosphate ions to produce calcium phosphate deposits, a pathological mineralisation commonly observed in soft tissues during disease states.

Chronic neuroinflammation is another prominent feature of Alzheimer's disease and significantly contributes to pathological calcification. Activated microglia and astrocytes release pro-inflammatory cytokines and chemokines, which can amplify calcium dysregulation by enhancing neuronal excitotoxicity and disrupting the blood-brain barrier (BBB), further elevating intracellular calcium levels. Persistent inflammation alters neuronal metabolism, exacerbates oxidative damage, and disrupts local phosphate metabolism, creating an environment conducive to intracellular mineral deposition. Inflammatory mediators can also compromise the integrity of neuronal and glial cells, promoting calcium and phosphate accumulation within cellular and extracellular compartments, which ultimately contributes to the progressive neuronal dysfunction characteristic of AD [79, 112, 113].

Investigating the role of specific pathways in mediating neuronal calcium accumulation and mineral deposition could provide insights into the formation of calcifications as the disease progresses. Moreover, quantifying the intracellular

calcification and examining interactions between neuronal calcification and traditional AD pathological markers could inform potential new markers for diagnostic and therapeutic strategies.

2.2.2 Roles of Calcification in Alzheimer's Disease

For the past century, Alzheimer's disease (AD) research has centred around amyloid-beta (Aβ) plaques and neurofibrillary tangles (NFTS) as the primary culprits of neurodegeneration. Yet, calcification has slowly emerged from the shadows; it's the pathological deposition of calcium phosphate in brain tissues. Calcium is essential for normal physiological functions, but its uncontrolled accumulation in soft tissues has long been recognised as a sign of pathology [30]. While calcification is an expected process in bones, its presence in the brain was initially overlooked and dismissed as an incidental finding rather than a driving force in neurodegeneration. However, growing evidence now suggests that mineral dysregulation, specifically calcium phosphate deposition, plays a crucial role in AD progression. In AD, calcification has been observed in regions affected by amyloid-beta (Aβ) plaques and neurofibrillary tangles (NFTS); it was not just a coincidence. The hippocampus, basal ganglia, and cerebral cortex are central to memory and cognition, suggesting a potential link between mineral dysregulation and disease pathology [51, 114]. This section examines the various forms of calcification in Alzheimer's disease (AD), their effects on neuronal function, and their relationship to disease initiation and progression.

One of the earliest recognised forms was vascular calcification, where calcium phosphate deposits accumulated within the walls of blood vessels and are commonly associated with or because of ageing and atherosclerosis. In AD, it appeared to take on a more sinister role. Vascular calcification has been observed in regions such as the hippocampus, basal ganglia, and cerebral cortex, narrowing blood vessels, restricting oxygen and nutrient flow to already vulnerable neurons, therefore, damage extended beyond ischemia [47, 98], calcified blood vessels compromised the integrity of the blood-brain barrier (BBB), allowing toxic proteins and inflammatory molecules to leak into brain tissues, exacerbating neuronal stress and cognitive decline. [59, 111]. Imaging studies using computed tomography (CT) and magnetic resonance imaging (MRI) confirmed the association—patients with pronounced vascular calcification exhibited lower cognitive scores and accelerated disease progression [115, 116]. Calcification was not confined to blood vessels alone. As researchers shifted their

focus to the neurons, they uncovered intracellular calcification, a phenomenon in which calcium phosphate accumulated directly within neurons and glial cells. Unlike vascular calcification, which restricts blood flow, this calcification disrupts cellular functions, including calcium signalling, mitochondrial activity, and synaptic transmission, ultimately leading to neuronal death [117, 118]. However, perhaps the most intriguing discovery was its relationship with tau pathology. The same neurons burdened with NFTS also harboured calcified deposits, raising the question: Was calcification a by-product of neurodegeneration, or could it actively drive disease progression? [119, 120].

A closer look at the molecular interactions revealed a compelling connection. Calcium dysregulation activated kinases such as CaMKII and GSK-3β, enzymes known to phosphorylate tau proteins [70, 121]. The hyperphosphorylated tau aggregated into NFTS, destabilising the neuronal cytoskeleton, and leading to cell death. The cycle appeared self-reinforcing: as tau pathology progressed, intracellular calcium handling became increasingly dysregulated, leading to further calcification and accelerating neuronal loss. The absence of early-stage calcification and pTau co-analysis leaves the overall process and its potential associations uncertain, making it difficult to determine whether calcification precedes, coincides with, or results from tau pathology in the early stages of AD.

However, the most elusive form of calcification remained hidden from conventional imaging techniques—intracellular calcification, the minuscule calcium phosphate deposits dispersed throughout brain tissues [122]. Unlike the more obvious vascular and extracellular calcification, these deposits are often too small to be detected by conventional imaging techniques, which require advanced methods such as electron microscopy and histochemical staining [93, 123, 124]. Using these advanced imaging methods, researchers found that microcalcifications are clustered in regions heavily affected by Alzheimer's disease (AD), including the hippocampus and temporal lobe. Their presence in early-stage AD brains suggested that these deposits might not be just a consequence of the disease but potentially one of its instigators [122]. Further microscopy analysis of calcification across different brain regions could offer deeper insights into the relationship between microcalcification and Alzheimer's disease progression, potentially clarifying its role in disease initiation and advancement.

The evidence supporting the positive role of microcalcification in AD progression grew stronger [65, 103, 125]. The evidence supporting this notion grew

stronger. Microcalcifications were frequently found near hyperphosphorylated tau, indicating a tight association with NFTS. Their ability to interact with calcium-binding proteins raised the possibility that they could serve as nucleation sites, promoting further tau aggregation and exacerbating AD pathology [126, 127]. But tau wasn't the only player in this interaction. The same calcium disturbances that contributed to tau hyperphosphorylation also appeared to influence Aβ aggregation [24, 104, 126]. Elevated intracellular calcium levels increase the production and aggregation of Aβ peptides, leading to plaque formation [55, 128]. Based on these notions, the question "Could microcalcifications scaffold pTau and Aβ accumulation, providing a structural foundation for amyloid plaques and NFTS to develop?" has been raised.

With mounting evidence suggesting a more significant role for calcification in AD, researchers have turned to advanced imaging techniques to track its progression [124, 129]. Electron microscopy unveiled dense microcalcifications interwoven with Aβ plaques and NFTS, visually confirming their spatial relationship. Histochemical staining further reinforced the findings, showing that these mineral deposits preferentially accumulated in areas most affected by AD pathology [18]. Therefore, it is essential to investigate the physicochemical properties of calcifications in Alzheimer's disease (AD) brains and determine whether specific mineral deposits are directly linked to disease progression [130, 131]. Assessing the extent and distribution of calcifications across different brain regions could provide crucial insights into stage-dependent mineralisation patterns, shedding light on how calcification evolves as AD advances. Researchers may uncover whether microcalcifications emerge as an early pathological feature or accumulate predominantly in later stages due to widespread neurodegeneration by quantifying calcification in correlation with Braak staging. Furthermore, a detailed examination of mineral composition, such as calcium phosphate [132, 133], carbonate substitutions [134], or other trace elements [135, 136], could help distinguish pathological calcifications from incidental mineral deposits observed in normal ageing.

Beyond structural analysis, it is crucial to investigate the biochemical and cellular interactions between calcifications and key pathological markers, such as hyperphosphorylated tau (pTau) [21] [71] and amyloid beta (Aβ) [23, 104]. Microcalcifications have been found to colocalise with neurofibrillary tangles and Aβ plaques, raising the possibility that these mineral deposits play an active role in AD

pathology by influencing protein aggregation, exacerbating neuronal stress, or triggering inflammatory responses [122].

Additionally, understanding the role of calcium dysregulation [55] in AD-related mineralisation could reveal novel mechanisms underlying disease progression. Dysregulated calcium signalling has been implicated in synaptic dysfunction, mitochondrial impairment, and neuronal apoptosis, all of which are hallmarks of AD. If calcification serves as both a marker and a potential driver of these pathological processes, targeting calcium homeostasis may represent a viable therapeutic strategy.

Future research should integrate high-resolution imaging techniques, such as electron microscopy [124] and advanced spectroscopy [120], with biochemical assays to unravel the interplay between calcification and neurodegeneration. By bridging structural and molecular analyses, these studies could help determine whether calcification is a secondary consequence of AD pathology or an independent contributor to disease onset and progression.

Ultimately, uncovering the full impact of calcification in AD could lead to the identification of novel biomarkers for early diagnosis and therapeutic interventions to mitigate neuronal mineralisation, thereby preserving cognitive function and slowing disease progression.

2.2.3 Micro-calcification and tau pathology

2.2.3.1 Intracellular vs. Extracellular Calcification

Beyond the well-established hallmarks of Alzheimer's disease (AD), such as amyloid-beta (Aβ) plaques and neurofibrillary tangles (NFTS), brain calcification has emerged as a significant pathological feature with potential implications for disease progression. As discussed in Section 2.2.2, calcification in AD manifests in various forms, including vascular calcification[97, 137], atherosclerosis-related calcification[138, 139], and cellular calcification[140], all of which contribute to cognitive decline. While calcification is predominantly recognised as an extracellular process occurring within the extracellular matrix [141], emerging evidence highlights the occurrence and significance of intracellular calcification in neurodegenerative diseases, including AD. This section examines the mechanisms and implications of microcalcification, particularly its association with tau pathology, and investigates how calcium dysregulation may contribute to Alzheimer's disease (AD) progression.

Calcification in the brain can be broadly categorised into extracellular and intracellular processes, each with distinct mechanisms and pathological consequences. Extracellular calcification occurs in the interstitial spaces between cells or within the extracellular matrix and is often associated with ageing, vascular diseases, and degenerative conditions [141]. In AD, extracellular calcification is frequently observed in blood vessels (vascular calcification), reducing cerebral blood flow and ischemic injury [138]. This form of calcification is triggered by factors such as chronic inflammation, disruption of the blood-brain barrier (BBB), and vascular injury. For example, vascular calcification in the hippocampus and basal ganglia has been linked to cognitive decline and neuronal damage in AD [6].

In contrast, intracellular calcification involves the accumulation of calcium phosphate deposits within cells, including neurons and glial cells. This process occurs when calcium ions accumulate beyond the buffering capacity of cellular mechanisms, leading to the precipitation of calcium phosphate [35, 133]. Intracellular calcification has been documented in various pathological conditions, such as mitochondrial calcification in heart transplant patients undergoing cyclosporine treatment [142, 143] and pathological myocardial calcification during the perinatal period [144, 145]. In the brain, intracellular calcification has been observed in Purkinje cells, where electron-dense vesicular structures, mitochondria, and lysosomes contain significant amounts

of calcium-phosphate deposits [140]. Similarly, malakoplakia, a condition characterised by granulomatous lesions with calcified lysosomes (Michaelis–Gutmann bodies), provides another example of intracellular calcification [146, 147]. In AD, intracellular calcification has been identified in regions affected by NFTS, suggesting a potential link between calcium dysregulation and tau pathology [122]. However, the mechanisms underlying intracellular calcification in AD remain poorly understood, necessitating further investigation.

2.2.3.2 Mechanisms Linking Calcium Dysregulation to Tau Pathology

Calcium ions are pivotal in intracellular signalling, acting as second messengers that regulate essential brain activities such as neurotransmitter release, neuron excitability, and synaptic plasticity [67, 148]. Under normal conditions, calcium homeostasis is tightly controlled to maintain optimal neuronal function[108, 117]. However, in AD, calcium dysregulation leads to elevated intracellular calcium levels, which activate kinases involved in tau phosphorylation. Elevated calcium levels activate kinases such as CaMKII and PKC, which phosphorylate tau at specific sites associated with its pathological aggregation [109, 117]. For example, CaMKII phosphorylates tau at Ser262, a site critical for dissociating from microtubules and subsequent aggregation [21, 74]. GSK-3β, a kinase implicated in tau phosphorylation, is activated under conditions of calcium dysregulation [27-29]. Calcium enhances GSK-3β activity directly or through pathways involving PP2A inhibition [30-35]. The resulting increase in tau phosphorylation promotes NFT formation, a hallmark of AD.

Hyperphosphorylated tau undergoes conformational changes that promote aggregation into paired helical filaments (PHFS), the primary constituents of NFTS [36, 41]. These aggregates act as seeds, triggering the aggregation of soluble tau proteins in neighbouring neurons [44-46]. Recent studies suggest that tau aggregates can spread prion-likely, contributing to the widespread distribution of tau pathology in AD [47, 48].

Beyond its role in tau hyperphosphorylation, calcium dysregulation in AD has also been implicated in pathological mineralisation. The elevated intracellular calcium levels that result from disrupted homeostasis [108, 117] can react with intracellular phosphate groups to form calcium phosphate precipitates, leading to neuronal calcification. The accumulation of these mineral deposits further exacerbates neurotoxicity by impairing normal calcium signalling, disrupting mitochondrial function,

and triggering oxidative stress. The formation of calcium phosphate microcalcifications may also serve as nucleation [149] sites that enhance tau aggregation, creating a pathological feedback loop that accelerates disease progression.

Studies have demonstrated a strong spatial correlation between phosphorylated tau aggregates and calcium deposits in brain regions affected by Alzheimer's disease (AD) [122]. This suggests a bidirectional relationship: while tau hyperphosphorylation may promote local calcium accumulation by altering ion-binding dynamics, the resulting calcifications may, in turn, exacerbate tau aggregation by providing a scaffold for pathological protein assembly. Furthermore, mineralisation could act as a secondary stressor on neurons [150, 151], intensifying inflammation and promoting cell death, which would facilitate the extracellular release of pathological tau species and further the spread of tau pathology [152].

The interplay between calcium dysregulation, tau phosphorylation, and calcification highlights the complex network of molecular events contributing to AD progression. Future research on leveraging and refining SBF simulation methodologies could further dissect the conditions that promote AD-associated calcification [153, 154]. Investigating how systemic calcium levels, phosphate availability, and other physicochemical factors influence neuronal mineralisation could provide valuable information on disease mechanisms. Modulating the calcium environment in controlled simulations could offer a novel approach to mitigating tau aggregation and pathological calcification.

2.3 Clinical and Therapeutic Implications

2.3.1 Diagnostic potential of mineralisation markers

The diagnostic potential of mineralisation markers in Alzheimer's disease (AD) represents a promising avenue for early detection and disease monitoring. These markers, including calcium phosphate deposits [155] and tau-associated calcification [122], are strongly correlated with AD pathology and are localised in critical brain regions such as the cerebral cortex [156], hippocampus[157, 158] and basal ganglia [48, 159]. Unlike conventional biomarkers targeting amyloid-beta (Aβ) and tau proteins [20, 22] , mineralisation markers emphasise disruptions in calcium homeostasis and cellular calcification processes, offering a novel perspective on disease progression [82]. Advanced imaging techniques, including positron emission tomography (PET), magnetic resonance imaging (MRI), and computed tomography (CT), enable the precise identification and quantification of these calcifications, revealing their spatial and temporal distribution in the brain [100, 102, 160, 161]. For instance, calcium phosphate deposits—detected via Von Kossa staining [162-164] and imaging modalities like MRI [116] —are prevalent in intracellular and extracellular environments, providing insights into their role in neurodegeneration. Amyloid plaque-associated calcification, another key marker, is closely linked to Aβ pathology and can be visualised using PET tracers and immunohistochemistry [112]. Vascular calcification, detected through X-ray fluorescence microscopy [44], further highlights the interplay between cerebrovascular health and AD. However, while tau-related calcification correlates with AD progression, no dedicated imaging technique exists for its specific detection, underscoring a critical research gap.

Recent advancements in imaging technologies have enhanced the detection of brain mineralisation. PET imaging, traditionally used to track metabolic activity and amyloid plaques [34], now employs calcium-sensitive tracers like 68Ga and 18F to map calcifications [113, 165, 166]. MRI techniques such as susceptibility-weighted imaging (SWI) and T2*-weighted gradient echo sequences excel in visualising microcalcifications by detecting magnetic susceptibility changes [116]. SWI, for example, reveals calcifications as hypointense signals due to their paramagnetic or diamagnetic properties, offering superior sensitivity compared to conventional MRI [115]. Despite these advances, limitations persist. CT scans, with a spatial resolution of 0.5–1 mm, struggle to detect subcellular calcifications [102], while PET's lower

resolution (~4–6 mm) restricts its utility to more significant deposits. MRI, though non-invasive, faces challenges in distinguishing microcalcifications from background noise or adjacent tissues. Microscopy and histopathological methods remain indispensable in addressing these limitations. Techniques like Von Kossa staining and OsteoSense markers provide high-resolution visualisation of calcifications in post-mortem tissues, enabling detailed morphological and chemical analyses [119, 167]. These methods have revealed intracellular calcium dysregulation as a key driver of AD progression, linking mineral imbalances to tau hyperphosphorylation and neuronal death.

2.3.2 Therapeutic Interventions Targeting Calcification in AD

Current therapeutic strategies for AD focus on symptom management and slowing disease progression. Cholinesterase inhibitors, such as donepezil [168, 169], rivastigmine [170, 171], and galantamine [170, 172], enhance acetylcholine levels to improve cognitive function in early to moderate AD [173]. Memantine, an NMDA receptor antagonist, mitigates glutamate-induced excitotoxicity in moderate to severe cases [170]. While these therapies provide symptomatic relief, emerging approaches target the underlying pathology, including anti-amyloid, anti-tau [171], and anti-inflammatory agents [174]. Notably, interventions addressing brain calcification are gaining traction, focusing on preventing mineral deposition rather than reversing existing calcifications.

Chelation therapy, using agents like EDTA to bind excess minerals, has shown potential in reducing vascular calcification and is now being explored for brain mineralisation. Calcium channel blockers, such as verapamil and diltiazem, aim to stabilise intracellular calcium levels, thereby preventing pathological accumulation and indirectly modulating tau phosphorylation [80, 81, 84]. Bisphosphonates, traditionally used to treat bone disorders by inhibiting calcium phosphate crystal formation [175, 176], are being investigated for their ability to reduce brain calcification by lowering calcium phosphate saturation. Dietary and lifestyle modifications, including reduced phosphate intake and increased magnesium consumption, offer non-pharmacological strategies to regulate mineral homeostasis [177]. These approaches highlight the dual benefit of targeting calcification and tau pathology, addressing multiple facets of AD progression.

Despite these advances, significant challenges remain. Current therapies are unable to dissolve existing calcifications, and imaging limitations restrict real-time monitoring of microcalcifications in living patients. Future research must prioritise the development of targeted tracers for PET and MRI to improve in vivo detection alongside clinical trials to validate the efficacy of anti-calcification therapies. Integrating diagnostic insights with therapeutic innovation has the potential to transform AD management, offering hope for more effective, personalised treatment strategies.

2.4 Research Gap

Despite over a century of investigation into Alzheimer's disease (AD), therapeutic breakthroughs remain elusive, even with extensive focus on canonical hallmarks such as amyloid-beta (Aβ) plaques and neurofibrillary tau tangles. Emerging evidence suggests that calcium dysregulation is playing a crucial role in dementia. However, there are significant gaps in understanding the neuronal microcalcification formation during AD progression and the underlying mechanisms.

One of the significant uncertainties in AD-related calcification research is the mechanistic ambiguity in calcification pathways. While a positive correlation has been established between the co-occurrence of calcification and pTau in clinical AD patients (e.g., Tsolaki et al., 2022 [122]), the causal relationship between intracellular calcification and AD progression remains unresolved. Observing early-stage neuronal calcification in various brain regions of AD samples, with the quantification analysis of the regional calcification, will give researchers insights into the association between the AD clinical symptoms and pathological properties.

Microcalcifications are early diagnostic markers with distinctive characteristics that can be observed in soft tissue using imaging techniques. However, technological limitations (e.g., insufficient resolution of current imaging modalities) impede validation, especially for brain visualisation. Non-invasive tools to quantify brain calcification in vivo are urgently needed to correlate calcification burden with clinical stages of AD. The post-mortem neuronal calcification study at all stages of AD progression will shed new light on the role of calcification in AD progression and advance research on neuronal calcification diagnostic tools, promoting early diagnosis of AD and furthering treatment options.

To date, most published studies have focused primarily on the clinical aspects of calcification in AD, such as imaging findings or its potential as a biomarker, with limited exploration of the underlying pathological mechanisms. Furthermore, there is a notable lack of research providing quantitative analysis of brain calcifications specifically in the context of AD progression. No existing studies have systematically measured or compared the extent of calcification across brain regions or across Braak stages, highlighting a significant gap in the current understanding of the role of mineralisation in AD pathology.

My study gradually paved the way from exploring the correlation between neuronal calcification and AD progression (Braak Stages) to pTau aggregation association across brain regions. Five hypotheses are made to revealing the role of microcalcification in AD progression:

Hypothesis 1: I hypothesise that the extent of brain calcification increases with the progression of Alzheimer's disease. To test this, histological brain samples from AD patients at different Braak stages will be analysed using SEM. These samples, collected from four AD-associated brain regions, will be compared to control samples from healthy young individuals. By quantifying calcification levels and correlating them with disease progression, I aim to determine whether micro-calcification is a biomarker for AD severity and identify potential regional patterns of mineral deposition.

Hypothesis 2: I propose that AD-like mineralisation can form in neuronal tissues under conditions mimicking the body's internal fluid environment. To explore this, I will develop in-vitro simulation models replicating the biochemical and mineral composition of body fluids to different tissue types. These models will identify which tissues and cell types are most susceptible to calcification. By pinpointing the specific locations and conditions that promote mineral deposition, I aim to uncover the origins of microcalcification and its role in AD pathology.

Hypothesis 3: I hypothesise that the mineralisation environment selectively degrades phosphorylated proteins while leaving tau proteins intact. To investigate this, I will expose different tau protein isoforms—including full-length tau (tau 441), full-length phospho-tau, tau 383, and short phospho-tau (pTau 199)—to a simulated mineral-rich environment. This comparative study aims to reveal how mineralisation influences tau protein behaviour and whether it contributes to the hyperphosphorylation observed in AD.

Hypothesis 4: I hypothesise that the co-localisation of neuron cells, hyperphosphorylated tau proteins, and intracellular calcification increases with the advancement of Braak stages. To test this, I will perform immunostaining on carefully selected histological human brain samples based on Braak stages and brain regions. By quantifying the distribution and interaction of these elements, I aim to establish a

spatial and temporal relationship between mineralisation and tau pathology, providing insights into the mechanisms driving AD progression.

Hypothesis 5: I propose that intracellular calcification acts as a nucleation point for neurofibrillary tangle (NFT) formation, one of the hallmarks of AD. Building on findings from early-stage analyses and specific brain region studies, I will examine post-mortem AD brain tissues and in vitro simulation models to determine whether micro-calcification initiates or exacerbates NFT accumulation. By identifying the timing and locations of intracellular mineralisation, aiming to uncover its role in the early stages of AD and its potential as a causal reason for AD on-site.

Chapter 3: Experimental Methods

3.1 Electron microscopes

3.1.1 Scanning Electron Microscopy (SEM) and microcalcification

3.1.1.1 SEM overview

Scanning electron microscopy (SEM) was selected to detect cerebral calcification due to its unparalleled capacity for high-resolution surface characterisation [178]. This technique employs a focused electron beam to interrogate sample surfaces through controlled raster scanning, generating nanoscale morphological data while preserving sample integrity [179, 180].

The SEM achieves sub-micron resolution through its field-emission electron gun (FEG) and electromagnetic lens system, enabling the visualisation of microcalcifications as small as 50 nm [123, 181] - a critical capability for identifying early-stage calcium phosphate deposits (hydroxyapatite) in AD-affected tissues. This resolution surpasses optical microscopy by three orders of magnitude, allowing precise mapping of calcification patterns along neuronal pathways and blood vessels. At 5-20 kV accelerating voltages, the electron probe diameter can be reduced to ≤1 nm, revealing ultrastructural details of pathological mineralisation that correlate with clinical dementia scales [122].

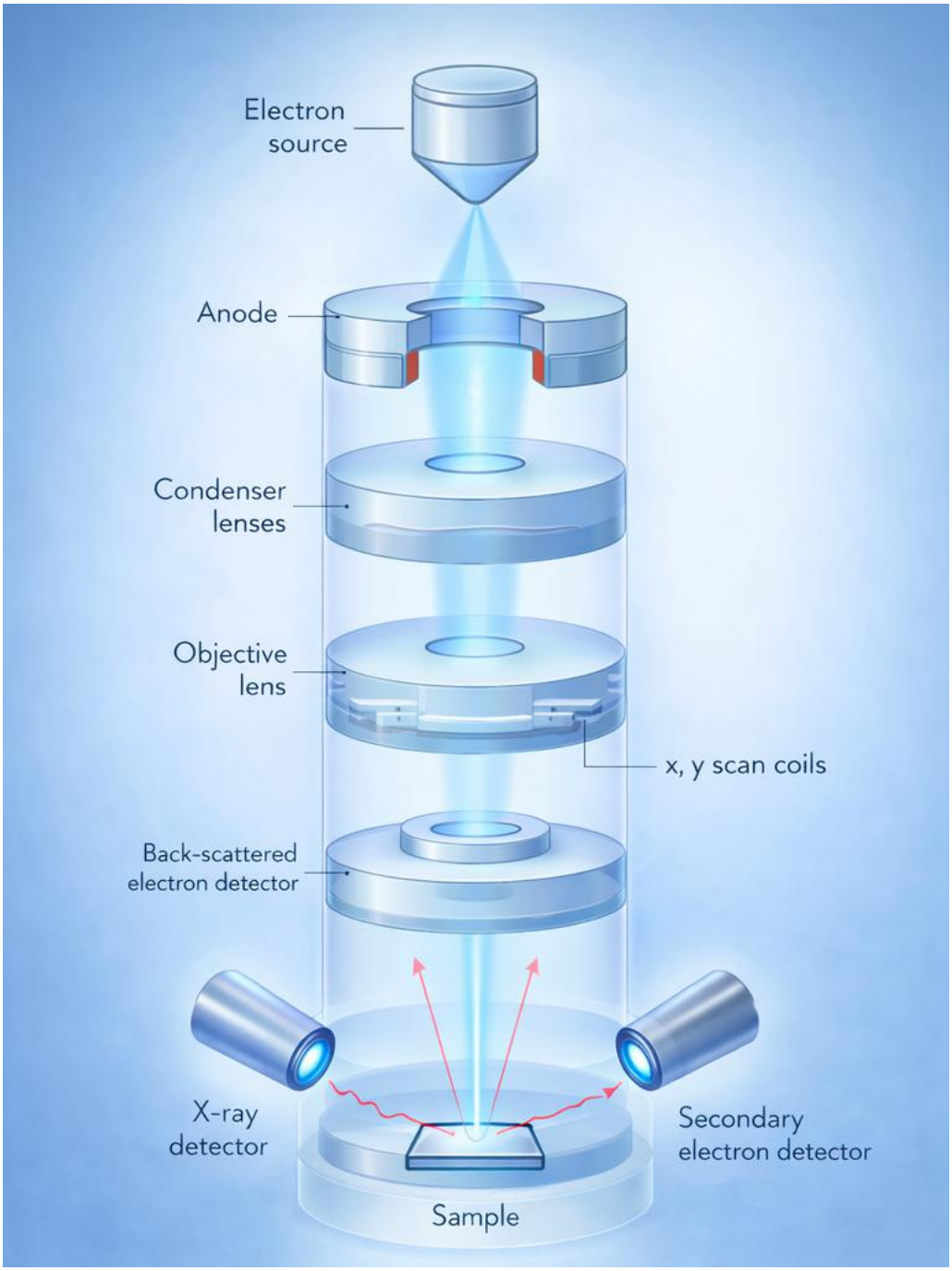

Figure 4. Conceptual diagram illustrating the SEM, including the main components and working principle based on previous literature [182].

Figure 4 illustrates the key internal structure of a Scanning Electron Microscope (SEM), comprising essential components necessary for generating high-resolution images [183]. The electron gun, the source of the electron beam, is located at the top of the SEM column. The two main types are thermionic and field emission guns (FEGS). Thermionic guns emit electrons in a heated filament (usually tungsten or lanthanum hexaboride). In contrast, FEGS apply an electric field to extract electrons

from a sharp tip, achieving better brightness and resolution. After emission, a high-voltage system accelerates the electrons to high energies [184].

Electromagnetic condenser lenses focus the accelerated electrons into a narrow beam at the sample. These electromagnetically controlled lenses are crucial for adjusting the beam's diameter and current density. Apertures between the lenses filter out scattered electrons to refine the beam. Lower in the column, scan coils direct the focused beam in a raster pattern across the sample surface. Electronic control of these coils ensures accurate scanning, which is vital for image formation [185].

The specimen chamber, which houses the sample stage, is located at the base of the SEM column. This stage allows the sample to be manipulated on multiple axes (x, y, z, tilt, and rotation) for precise positioning under the beam. The chamber is kept under a high vacuum to minimise electron scattering from air molecules[178].

3.1.1.2 Imaging

In scanning electron microscopy (SEM), multiple detectors are used to capture signals resulting from the interaction between the electron beam and the sample [186]. Among these, **secondary electron (SE) imaging** is the most used mode for visualising fine surface details at the nanoscale [187, 188].

The Everhart–Thornley detector is a widely used SE detector, collects low-energy secondary electrons—typically below 50 eV—emitted from the outermost layers of the sample (Figure 5(a)). Because these electrons originate from near the surface, the resulting images offer high spatial resolution and provide detailed information on surface topography with a characteristic three-dimensional appearance [189].

The in-lens detector is a high-resolution imaging component positioned inside the electron column, directly above the sample. Unlike conventional secondary electron detectors placed outside the column, the in-lens detector collects low-energy secondary electrons that are efficiently channelled through the objective lens system. This configuration significantly reduces noise and enhances image contrast, especially at low accelerating voltages. The in-lens imaging (Figure 5(b)) provides exceptional surface sensitivity and fine structural detail, making it ideal for analysing delicate nanostructures, thin films, and biological specimens. Its enhanced resolution and

reduced charging effects also make it particularly advantageous for imaging non-conductive or beam-sensitive samples without the need for heavy metal coating [190].

The **Backscattered Electron (BSE)** detector collects high-energy electrons elastically scattered from the sample's atomic nuclei. The signal intensity is proportional to the atomic number (Z) of the elements—higher-Z elements appear brighter—enabling strong compositional contrast [191]. This makes BSE imaging (Figure 5(c)) useful for distinguishing different materials or phases within a sample. In biomedical applications, such as Alzheimer's research, BSE is particularly effective for detecting calcification in soft tissues. Calcium-rich deposits, like microcalcifications, appear bright due to calcium's higher atomic number, allowing researchers to visualise and analyse mineralisation patterns that may be linked to disease progression [192].

(a)

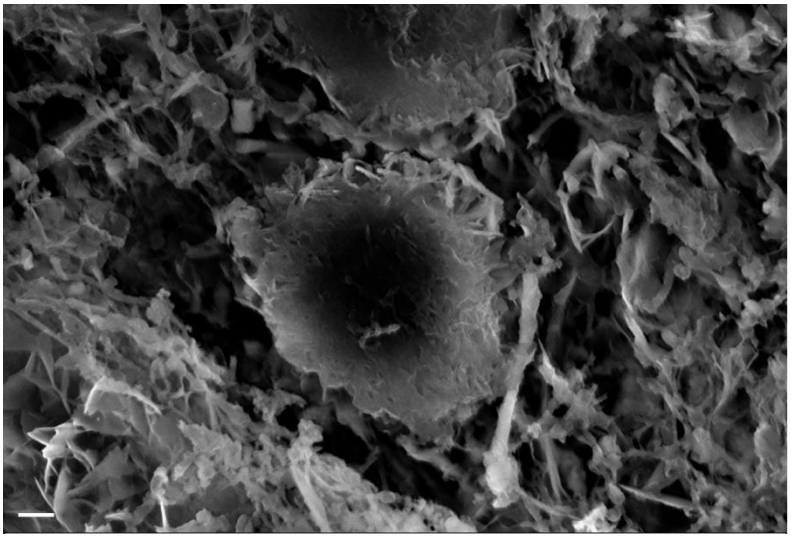

(b)

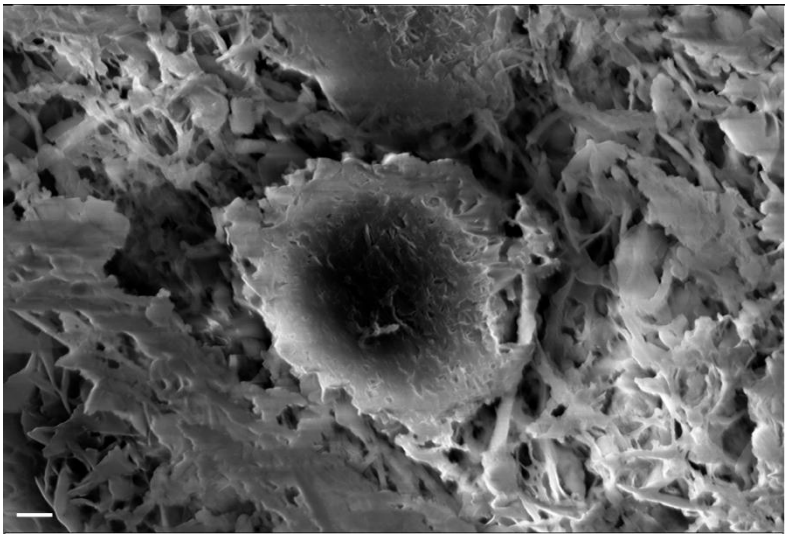

(c) 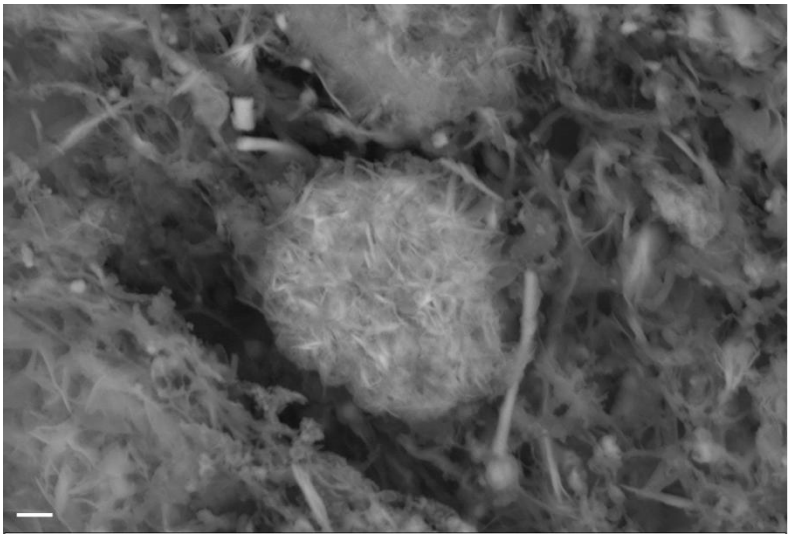

Figure 5. SEM images of inorganic particles in brain tissue (hippocampus sample P1-08), scale bars = 1μm. (a) SE micrograph. (b) In-lens micrograph. (c) BSE micrograph (organic = black, inorganic = white).

3.1.1.2 Density Dependent Colour – Scanning Electron Microscopy (DDC-SEM)

After acquiring both secondary electron (SE) and backscattered electron (BSE) images, a **Density-Dependent Colour (DDC) Map** (Figure 6) is generated by digitally merging the two imaging modes [193]. This composite image applies artificial colours to enhance contrast and improve visual interpretation. SE data—providing surface topography—is typically assigned one colour channel, while BSE data—reflecting compositional contrast—is assigned another. The resulting dual-colour image allows for simultaneous assessment of surface morphology and elemental composition. This technique is particularly effective for analysing soft tissues, as it clearly reveals the size, density, and precise location of calcifications, which would be less distinguishable using a single imaging mode.

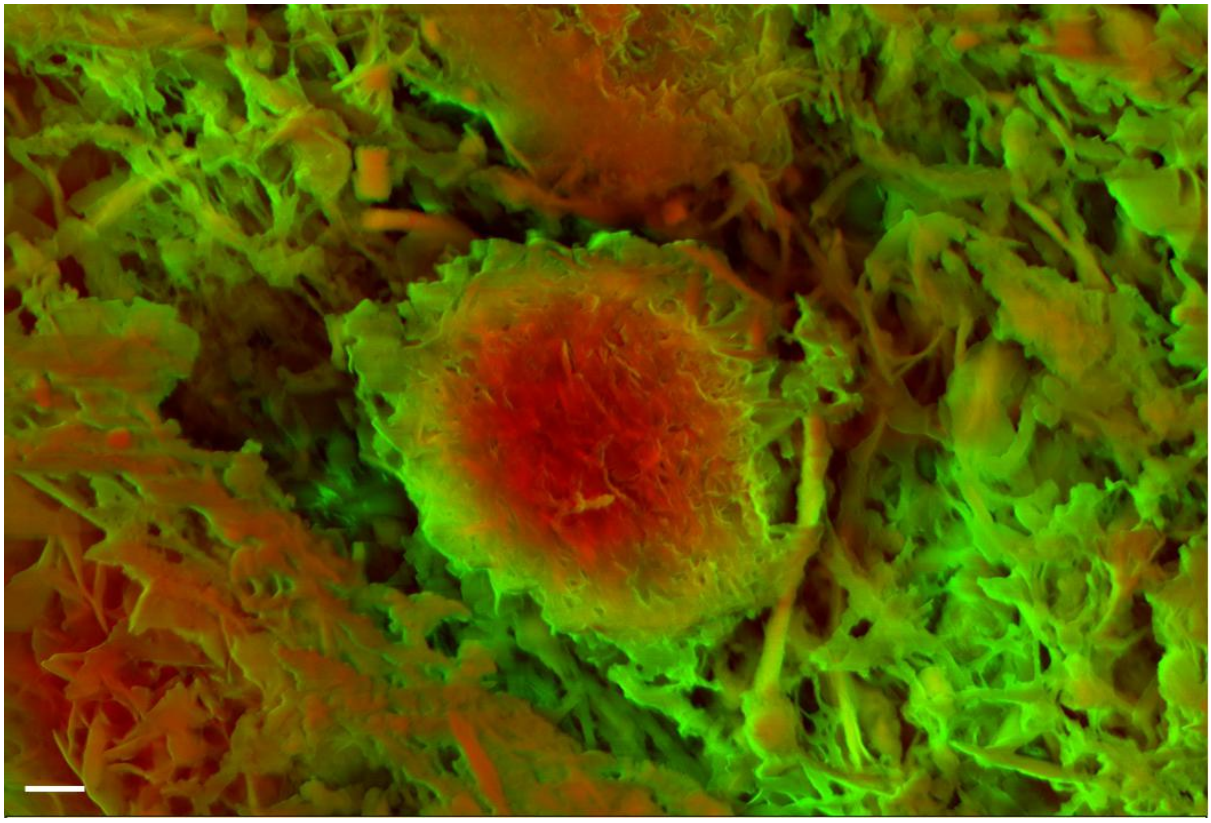

Figure 6. DDC-SEM images of inorganic particles in brain tissue (hippocampus sample P1/08), scale bars = 1μm. With the in-lens micrograph in green channel and BSE micrograph in red channel. (organic = green, inorganic = red/orange)

3.1.1.3 Composition analysis – Energy Dispersive X-ray Spectroscopy (EDS)

Energy-dispersive X-ray spectroscopy (EDS) is an analytical technique commonly integrated with electron microscopy to provide elemental composition data [194]. When the primary electron beam interacts with a sample, it can eject inner-shell electrons from atoms. As electrons from higher energy levels fill these vacancies, characteristic X-rays are emitted. These X-rays are specific to each element, allowing the EDS detector to identify and quantify the elements present in the sample.

EDS generates both elemental spectra and spatially resolved elemental maps, making it particularly useful for analysing mineralised structures in biological tissues [195]. In the context of Alzheimer's disease research, EDS can confirm the presence and distribution of calcium and phosphorus, the primary constituents of pathological calcification. By combining EDS with high-resolution electron microscopy, researchers can correlate morphological features with elemental composition, providing deeper

insights into the nature and progression of mineralisation in diseased brain tissue [196].

3.1.1.4 Biological tissue sample preparation for SEM

Imaging biological samples with electron microscopy presents inherent challenges due to the non-physiological operating conditions, particularly the high vacuum environment required for SEM operation [197]. Biological tissues are naturally rich in moisture, which is incompatible with vacuum conditions and can lead to sample degradation or imaging artefacts. Therefore, careful sample preparation is essential to ensure both sample stability and high-quality visualisation [198].

In this project, all tissue specimens were Formalin-Fixed, Paraffin-Embedded (FFPE) samples. Prior to SEM examination, the paraffin was removed through a series of xylene washes, with each immersion lasting 10 minutes and repeated three times. After the final wash, samples were air-dried at room temperature to remove residual solvent. It is essential to ensure that samples are completely dry before applying the conductive coating, as residual moisture can interfere with coating adhesion and compromise imaging quality. To enhance electron conductivity and image clarity, a 5-µm-thick carbon coating was applied to the tissue-facing side of each slide using a controlled coating machine. In addition, silver paint was applied to the non-tissue-covered areas to further improve electrical grounding. For added conductivity, a second 5 µm thick carbon layer was deposited on the sample surface. Copper tape was used to firmly secure the slides to the SEM sample stage, ensuring positional stability during imaging.

Electrical conductivity is critical in SEM, especially for biological samples. Non-conductive materials tend to accumulate charge under the electron beam, leading to beam distortion, image artefacts, and poor contrast. Adequate conductivity allows excess electrons to dissipate, minimising charging effects and enabling the detection of secondary and backscattered electrons with high efficiency. This ensures sharp, high-resolution images with minimal distortion. Poor conductivity not only reduces image quality but also increases the risk of sample damage, particularly in delicate biological tissues or nanostructures, due to localised heating or electron beam-induced displacement [199].

3.1.2 Transmission Electron Microscopy (TEM) and microcalcification

3.1.2.1 TEM overview

Transmission Electron Microscopy (TEM) was chosen as the primary technique for investigating protein-level calcification due to its unparalleled imaging resolution at the nanoscale [200]. TEM functions by transmitting a focused beam of electrons through an ultra-thin specimen, producing highly detailed two-dimensional images of internal structures [201]. This makes it particularly well-suited for examining protein complexes and nanostructured mineral deposits, enabling the visualisation of fine morphological details that are not accessible through other microscopy methods. Its atomic-scale resolution allows for the observation of protein conformational changes and interactions associated with the early stages of calcification [202]. Furthermore, TEM can be coupled with EDS to provide compositional analysis of the calcified regions, offering comprehensive insights into the structural organisation and elemental makeup of protein-associated mineralisation.

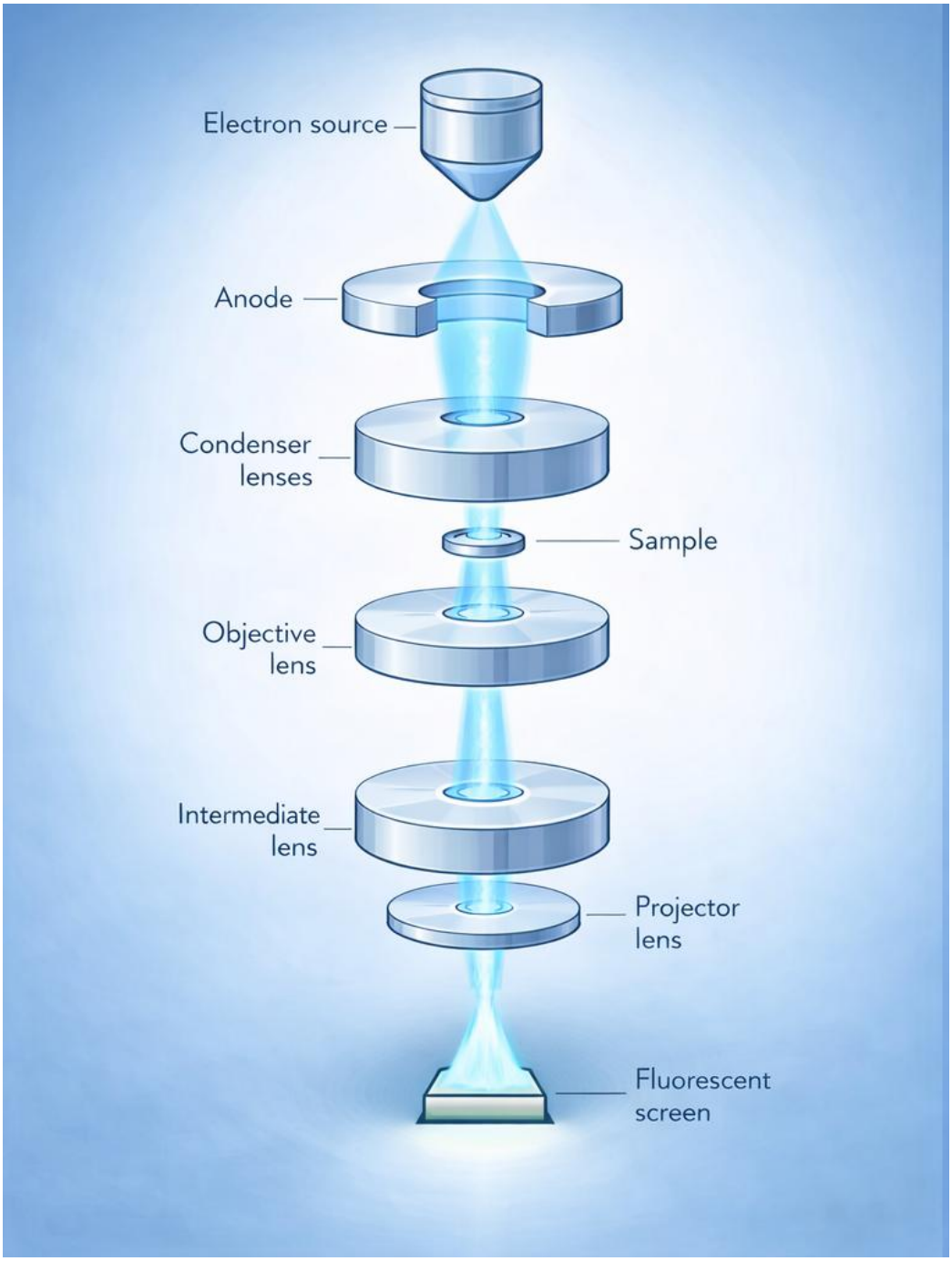

Figure 7. Conceptual diagram illustrating the TEM including the main components and working principle based on previous literature [182].

As illustrated in Figure 7, Transmission Electron Microscopy (TEM) operates by transmitting a beam of electrons through an ultra-thin specimen to produce high-resolution images that reveal the internal architecture of the sample. The process begins with an electron gun, typically equipped with a tungsten filament or a field emission source, which generates a highly focused electron beam. This beam is

accelerated to high energies—commonly between 60 and 300 keV—resulting in extremely short wavelengths that enable imaging at atomic resolution.

The beam is condensed into a coherent stream by a series of condenser lenses before interacting with the specimen, which is prepared to a thickness of less than 100 nanometres and mounted on an electron-transmissible grid. As the electron beam passes through the sample, it is scattered according to the material's density and atomic composition. The scattered electrons are then collected by objective lenses to form a primary image, which is further magnified by intermediate and projector lenses and displayed on a digital camera for image acquisition [201].

Contrast in TEM is primarily generated by variations in electron density and sample thickness—denser regions scatter more electrons and thus appear darker in the final image. To enhance analytical capability, TEM can be integrated with Energy-Dispersive X-ray Spectroscopy (EDS) for elemental analysis [196], and Selected Area Electron Diffraction (SAED) for structural characterisation of crystalline regions [203]. EDS identifies the chemical composition by detecting characteristic X-rays emitted from excited atoms, while SAED provides diffraction patterns that reveal the crystalline order of mineral phases.

These advanced features make TEM an indispensable tool for investigating protein-level mineralisation and calcification, offering unparalleled insight into nanoscale structure, composition, and molecular interactions. In this context, TEM significantly surpasses the spatial resolution limits of Scanning Electron Microscopy (SEM), making it particularly valuable for elucidating calcification processes at the atomic scale.

3.1.2.2 Imaging

TEM images provide detailed internal structural information, distinguishing them from surface imaging techniques. In the context of Alzheimer's disease (AD) calcification, the contrast in TEM images arises from variations in electron density, atomic number, and sample thickness. Denser or thicker regions, such as calcified deposits, scatter more electrons, appearing darker, while less dense areas show lighter contrasts [204]. This allows TEM to effectively visualise and characterise calcification in AD tissues, revealing fine details of mineralised regions and their interactions with surrounding structures. With their high resolution and contrast, TEM images offer invaluable insights

into microcalcifications and their role in disease progression, making TEM a powerful tool for studying pathological mineralisation in Alzheimer's research [205].

3.1.2.3 Composition analysis – Energy Dispersive X-ray Spectroscopy (EDS)

The integrated EDS in TEM operates on the same principle as the EDS in SEM, as described in section 3.1.1.4.

3.1.2.4 Diffraction analysis

TEM integrated Selected Area Electron Diffraction (SAED), which enhances its capabilities by providing detailed insights into the crystalline structures of materials. SAED works by analysing diffraction patterns produced when the electron beam interacts with the sample. This technique reveals critical information about lattice spacing, crystal orientation, and the degree of crystallinity, making it particularly valuable for studying mineralised deposits and calcification at the atomic scale [203, 206].

SAED allows for the precise identification of crystal structures within biological samples, enabling researchers to better understand the structural organisation of calcifications and their role in disease processes. By offering high-resolution analysis of nanoscale structures, SAED makes TEM an indispensable tool for investigating the detailed mechanisms of protein-level mineralisation and calcification, surpassing the resolution limitations of Scanning Electron Microscopy (SEM).

3.1.2.5 Biological protein sample preparation for TEM

Imaging protein solutions with Transmission Electron Microscopy (TEM) presents unique challenges due to the need for thin, dry samples in a vacuum environment, which can distort or damage biological materials if not properly prepared. Protein solutions are inherently liquid, and moisture can interfere with the electron beam and image clarity. Therefore, proper sample preparation is crucial to achieve stable, high-quality TEM images [207].

In this project, protein solutions were concentrated and applied to carbon-coated copper grids. The excess solution was blotted away with filter paper to achieve uniform protein distribution. Afterward, the grids were air-dried to ensure that the solvent was completely removed. This drying step is essential, as residual moisture can affect the stability of the protein layer and the adhesion of any coatings, compromising image quality. To improve electron conductivity and minimize charging

effects during imaging, a 5-μm-thick carbon coating was applied to the protein-facing side of the grid using a controlled coating machine to enhance conductivity. Proper conductivity is essential in TEM, as non-conductive samples tend to accumulate charge under the electron beam, causing image distortion and artefacts. Adequate conductivity allows for efficient electron dissipation, improving image contrast and resolution, and preventing sample damage from localised heating or displacement [208].

3.1.3 Confocal fluorescence microscopy

3.1.3.1 Confocal fluorescence microscopy overview

Confocal microscopy [209] is an optimal imaging modality for investigating the multiplex interrelationship among neurons [210, 211], microcalcifications, and phosphorylated tau (pTau) in Alzheimer's Disease (AD). Its superior resolution and capacity for optical sectioning within dense biological tissues enable precise visualisation of pathological markers at the cellular level. Given the complex three-dimensional structure of neurons, their interactions with microcalcifications and pTau often occur within specific focal regions of brain tissue [209]. Confocal microscopy facilitates the accurate imaging of these focal planes, allowing for a detailed examination of colocalisation patterns.

A key advantage of confocal microscopy is its ability to capture multiple fluorescent labels simultaneously. This capability is particularly beneficial for this study, as it enables the use of distinct fluorescent dyes to identify neurons, microcalcifications, and pTau within a single sample [212]. This technique can generate high-resolution, three-dimensional reconstructions of these pathological markers, providing crucial insights into their spatial relationships and roles in AD progression [213]. The enhanced visualisation offered by confocal microscopy ensures a comprehensive assessment of microcalcifications and tau aggregation in neuronal degeneration, furthering our understanding of AD pathology.

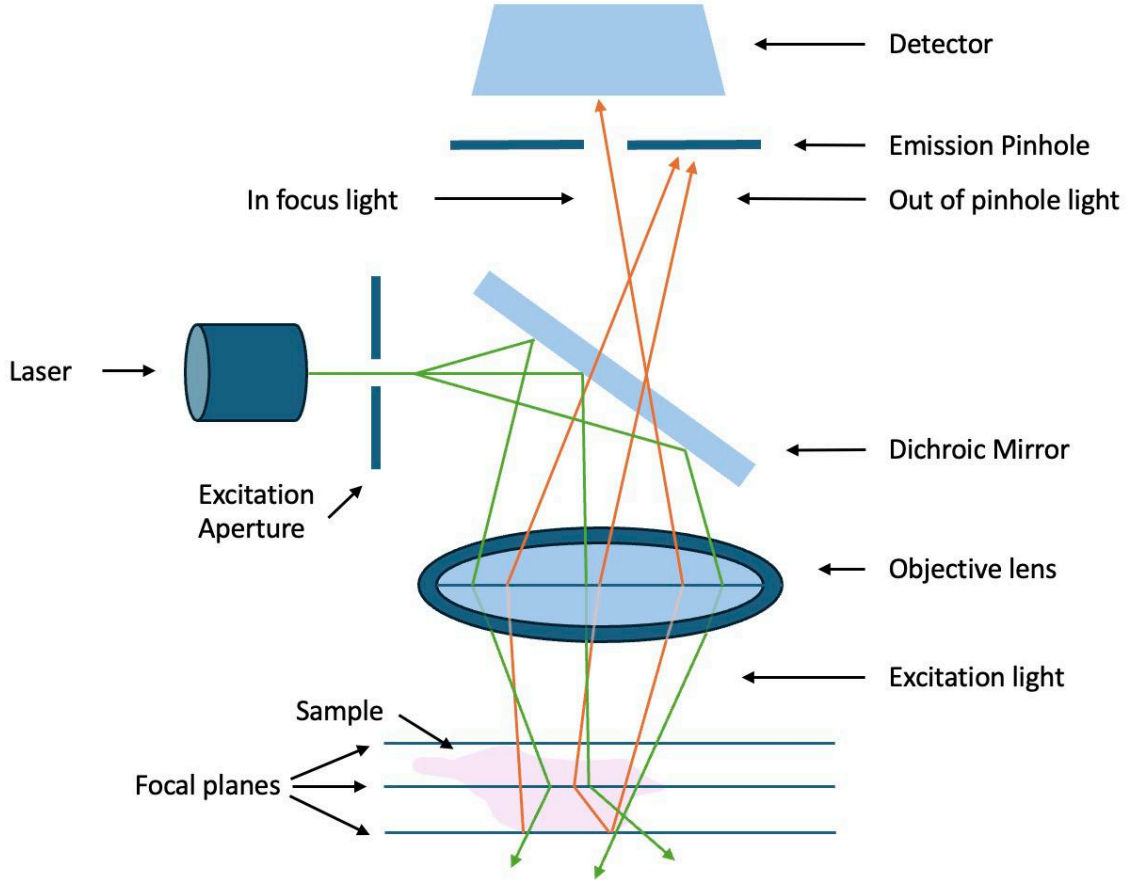

Figure 8. Conceptual diagram illustrating the confocal microscopy, including the main components and working principle based on previous literature [214].

Figure 8 outlines the operational principles of confocal microscopy [209]. In this technique, a laser source (illustrated on the left) emits a focused beam of coherent light at a designated wavelength directed toward the sample [215]. A dichroic mirror plays a crucial role in this process, selectively reflecting the excitation light (green) toward the objective lens while allowing the sample's emitted fluorescence light (red) to pass through. This separation of excitation and emission light pathways is essential for minimising background noise and ensuring high-resolution imaging.

Once the laser beam reaches the sample, it excites fluorophores within the labelled structures, causing them to emit fluorescence at a longer wavelength. The emitted fluorescence travels back through the optical pathway, passing through the objective lens and dichroic mirror before reaching the pinhole aperture. The pinhole is a defining feature of confocal microscopy, as it effectively blocks out-of-focus light, enhancing image clarity and contrast [216]. Only fluorescence originating from the

focal plane can pass through the pinhole, while light from other regions of the sample is excluded.

The filtered fluorescence signal is then captured by a photomultiplier tube (PMT) or a charge-coupled device (CCD), which converts the light into an electrical signal for digital image generation [217]. The laser systematically scans the sample in a raster pattern to construct a complete image, incrementally capturing fluorescence signals from different regions. Additionally, by adjusting the focal plane and acquiring multiple optical sections at varying depths, confocal microscopy enables the reconstruction of detailed three-dimensional images

3.1.3.2 Immunofluorescence staining

Immunofluorescence staining is a technique used to detect specific proteins, antigens, or other biomolecules within tissue or cell samples [218]. The method relies on the binding of a primary antibody to its specific antigen, enabling the visualization of target molecules at the cellular or subcellular level. The primary antibody is then detected using a secondary antibody, which is conjugated to a fluorescent marker, allowing the antibody-antigen complex to be visualized under a fluorescence microscope [219].

In the context of Alzheimer's disease (AD) calcification, immunostaining is employed to identify and visualize both calcification and associated protein markers in brain tissue. The OsteoSense fluorescent probe was chosen for this study because it binds with high affinity to hydroxyapatite (HA), a key component of calcifications found in both in vitro and in vivo environments. Hydroxyapatite is known to bind pyrophosphates, phosphonates, and synthetic bisphosphonates, which are involved in the formation of calcified deposits. The IVISense Osteo probes, designed as bisphosphonate imaging probes, enable the targeted visualization of these calcifications.

The antibody-antigen interaction allows precise identification of proteins within tissue samples, distinguishing them from surrounding structures [220]. In this study, immunostaining reveals the distribution of key proteins such as phosphorylated tau (pTau) and neurons. The antibodies used are specifically engineered to bind to these targets, enabling the visualization of how calcifications interact with pTau and neurons in the context of AD. This provides valuable insights into the role of calcification in AD progression.

By selectively binding to pTau, neurons, and calcification deposits, immunostaining enables detailed localization and quantification of these features in AD tissues. This technique is instrumental in uncovering the potential role of calcification and its correlation with pTau and neurons, offering a deeper understanding of its contribution to the progression of Alzheimer's disease.

3.1.3.3 Biological tissue sample preparation for confocal microscopy

In this project, SEM corresponded FFPE tissue specimens were analysed by confocal microscopy [221]. Prior to confocal examination, the paraffin was removed to expose the tissue to the antibody solutions. This is achieving through a series of xylene washes, with each immersion lasting 10 minutes and repeat three times.

After deparaffinisation, tissue sections were rehydrated through a graded ethanol series to restore water content and preserve tissue integrity for subsequent analysis. The slides were sequentially immersed in 100% ethanol (two changes, 5 minutes each), followed by 95%, 70%, and 50% ethanol (each for 5 minutes), and finally rinsed in distilled water for 5 minutes. This gradual rehydration process ensured a smooth transition from an organic to an aqueous environment, minimising osmotic stress and maintaining tissue morphology. Proper rehydration was critical for preparing the samples for downstream procedures, including immersion in simulated body fluid (SBF) for mineralisation studies or immunostaining for protein localisation.

Followed by the permeabilisation and blocking to allow antibody access to intracellular targets and minimise non-specific binding. Samples were incubated in PBS containing 0.1% Triton X-100 for 10 minutes at room temperature, followed by two 5-minute washes in PBS to remove excess detergent. This was achieved by incubating the slices for 6 hours in PBS containing 0.1% Triton X-100 and 2% normal donkey serum, which was prepared by adding 50 µl of Triton X-100 and 1 g of serum to 50 ml of PBS.

Following blocking, primary antibody incubation was carried out. The slices were incubated with primary antibodies diluted in the same blocking buffer for 8 hours at room temperature or overnight at 4°C. The primary antibodies used were anti-Phospho-Tau (Ser202, Thr205) [AT8] mouse monoclonal antibody at a 1:200 dilution, and anti-NeuN [EPR12763] rabbit recombinant antibody at a 1:100 dilution. The primary antibody mix was prepared by combining 1 µl of pTau and 2 µl of Neu in 200

µl of blocking buffer, with 20 µl applied to each slide. Following incubation, the slices were washed four times in blocking buffer, each lasting 30 minutes.

Secondary antibody incubation followed, using fluorophore-conjugated antibodies diluted in hybridisation buffer containing Triton X-100. Goat anti-mouse Alexa Fluor 555 (pTau) and sheep anti-rabbit Alexa Fluor 488 (Neu) were used at a 1:200 dilution. A typical secondary antibody mixes for 15 samples included 1.3 µl of pTau, 1.5 µl of Neu, and 0.3 µl Triton X-100 in 300 µl of buffer; an alternative formulation used 2 µl of each antibody and 0.4 µl Triton X-100 in 400 µl of buffer. The slices were incubated with the secondary antibody mixture for 8 hours in the dark, followed by four 30-minute washes in blocking buffer, also performed in the dark to protect fluorophores.

For nuclear staining, DAPI was applied at a 1:10,000 dilution for 10 minutes at room temperature, followed by another set of four 30-minute washes in blocking buffer. Finally, slices were incubated with OsteoSense dye at a 1:10 dilution for 20 minutes to visualise calcification. Excess dye was removed with four additional 30-minute washes in blocking buffer before imaging. A colour corresponding sum is shown in Table 1.

Primary Antibodies	Phospho-Tau (Ser202, Thr205) Monoclonal Antibody (AT8) - Mouse
	Recombinant Anti-NeuN antibody [EPR12763] - Neuronal Marker (MAP2-focused) (ab177487) - Rabbit
Secondary Antibodies	Goat anti-mouse - 555 1:200 concentration – 555 (pTau)
	Sheep anti-rabbit - 488 1:200 concentration – 488 (Neuron)
Non-Antibody stains	OsteoSense 680 (Calcification)
	DAPI (DNA/ Nuclei)

Table 1. A summary table displaying the selection of antibodies and stains used in this project, with the corresponding colours highlighted.

3.2 Statistical analysis

3.2.1 Correlation study

3.2.1.1 Pearson correlation

Pearson's correlation coefficient (r) measures the linear relationship between two continuous variables and assumes that the data is normally distributed, ranging from -1 (perfect negative correlation) to +1 (perfect positive correlation). A value of 0 indicates no correlation. It is widely used in fields such as economics and sciences when assessing the strength of linear relationships [222]. This measure is particularly valuable when researchers aim to quantify how changes in one variable relate to changes in another if the data follows a normal distribution [223]. In this case, Pearson's correlation can be used to investigate the relationship between the age and the amount/size of calcification, therefore, analysing whether amount/size of calcification increase linearly with the age.

3.2.1.2 Spearman correlation

Spearman's rank correlation coefficient (ρ) assesses the monotonic relationship between two variables, regardless of whether the relationship is linear [224]. It is suitable for ordinal data or when the assumptions of normality are not met, making it useful in biology or psychology for ranking preferences or assessing relationships in non-linear data [225]. In this research, it can be used to assess the relation between patient Braak stages and the amount of calcification.

3.2.2 Hypothesis test

To validate the Hypothesis 1 and Hypothesis 4, I applied a hypothesis test to the numerical data collected. Given the imbalanced group sizes in our research, the Mann-Whitney U Test was chosen as the primary non-parametric statistical approach.

The Mann-Whitney U Test, also known as the Wilcoxon rank-sum test, was used to compare two independent samples and determine whether there were differences in their population distributions [226]. One of its key advantages is that it does not require the data to follow a normal distribution. This makes it highly suitable for analysing skewed, ordinal, or non-continuously data, providing more flexibility than parametric tests relying on normality assumptions [227].

This test is robust against outliers. Ranking the data before analysis reduces the impact of extreme values on the results, unlike tests such as the t-test, which are based on the mean and variance [227]. This ranking mechanism enhances the test's reliability, especially for small sample sizes where data collection can be difficult or costly, as in our project.

Moreover, the Mann-Whitney U Test effectively analyses ordinal data since it preserves the ranked order without assuming linear relationships between scale points. It can also handle tied ranks well, adjusting calculations to ensure accuracy when non-distinct data points exist. These features ensure reliable results even in datasets with multiple identical values, making it a versatile and dependable choice for our analysis.

All group- and stage-based tests were conducted under the null hypothesis, which posits that there is no difference between the two groups. In addition to hypothesis testing, we performed correlation studies to evaluate the strength and direction of relationships among two or more variables. Our goal was to explore associations between variables and quantify their interrelation.

Chapter 4: Calcification identification and quantification

4.1 Introduction

Brain calcification has been observed in regions commonly associated with Alzheimer's disease (AD), including the basal ganglia, hippocampus, and temporal lobe [122]. A significant difference in calcification levels has also been reported between age-matched elderly individuals and those diagnosed with AD. Despite these findings, the role of micro-calcification in AD remains largely unexplored, hindering progress in understanding the pathological pathways involving inorganic compounds in the formation and progression of the disease. Identifying specific types of calcifications as potential biomarkers for AD or for early diagnosis remains a critical gap in research. This underscores the need for further investigation into the potential contribution of calcifications in AD progression. Therefore, leading to my **Hypothesis 1: the extent of brain calcification increases with the pathological progression of Alzheimer's disease**. This will be implied by quantifying the size and the amount of calcification of different AD related brain regions along with pathological progression by electron microscopy.

4.2 Materials and methods

4.2.1 Samples

Post-mortem brain specimens were obtained from two established neuropathological repositories: the Queen's Square Brain Bank (London) and the Edinburgh Brain Bank. Ethical approval for tissue procurement was granted under reference REC 21/LO/0123. Tissue sections of 4µm thickness from the basal ganglia at the level of the anterior commissure, hippocampal area at the level of the lateral geniculate body, temporal neocortex (Brodmann areas 21 and 22) and Broca Area (BA44/45) were obtained. These regions were selected based on their association with common AD symptoms, as outlined in Chapter 2.1.1.

Broca's area was included as a control region, as it is primarily associated with language production that is typically impaired in the later stages of Alzheimer's disease. Since the present study focuses on early pathological changes, Broca's area samples were examined only in cases classified as Braak stages I–IV, during which speech-related symptoms are generally not yet clinically apparent and this region is not expected to be significantly affected.

Due to limitations in tissue availability and anatomical sampling, Broca's area sections were only obtainable in a subset of ten additional subjects. These samples were therefore analysed as a supplementary control dataset rather than as part of the main quantitative analysis. At least two consecutive sections were obtained per case where possible, to ensure internal consistency. The purpose of including this region was to assess whether the observed pathological features were region-specific rather than reflecting a global cortical phenomenon.

The study cohort included two distinct groups. The Alzheimer's disease (AD)-associated group consisted of 54 cases, with an age range of 56–95 years (mean age 77.19 ± 6.3). This group was further subdivided into 29 age-matched controls (with Braak staging but not diagnosed with AD) and 25 symptomatic AD cases (diagnosed AD), as outlined in Table 2. The control group comprised 15 neurologically healthy subjects, aged 16–40 years (mean age 26.47 ± 4.1 years), as shown in Table 3. This will be implied by quantifying the size and the amount of calcification of different AD related brain regions along with pathological progression by electron microscopy.

	Patient code	Sex	Age	Braak Stages	Clinical information
1	P18/03	F	56	1	mild small vessel disease
2	P31/11	M	88	1	N/A
3	P32/09	F	86	1	Small vessel disease
4	P41/09	M	95	1	lacunar infarct due to small vessel disease, pathological aging (Braak 1) Argyrophilic grain disease
5	P47/11	F	79	1	Pathological aging Braak 1, mild hyaline arteriosclerosis
6	P58/10	F	87	1	mild age-related changes (Braak I), mild CVD
7	P66/06	M	57	1	N/A
8	P69/06	M	75	1	moderate CAA, LB pathology
9	P72/07	M	85	1	N/A
10	P75/08	M	87	1	moderate small vessel disease, tau pathology (Braak I)
11	P78/06	F	68	1	metastasis
12	P21/15	F	76	2	N/A
13	P48/06	F	89	2	Vascular dementia, old cerebral infarct, AD path low
14	P51/08	F	82	2	Pathological aging (Braak II), mild small vessel disease, moderate CAA
15	P62/05	M	62	2	severe CAA
16	P64/04	F	80	2	Argyrophilic brain disease, pathological ageing Braak II, small vessel disease
17	P64/11	F	80	2	argyrophilic brain disease, pathological ageing Braak II, small vessel disease
18	P66/10	M	87	2	Pathological ageing (Braak II)
19	P76/06	F	87	2	path aging Braak II, mild CVD
20	P77/06	F	82	2	Pathological aging Braak II, mild CAA
21	P1/11	F	93	3	pathological ageing (Braak III)
22	P13/03	M	77	3	severe CAA, transitional LBD
23	P45/04	F	78	3	mild small vessel disease, mild age-related changes
24	P64/03	F	88	3	Normal, multiple cortical infarcts, small vessel disease and pathological aging
25	P67/10	F	92	3	cerebral infarct, CVD, pathological ageing (Braak III)
26	P75/10	M	83	3	Pathological ageing (Braak III)
27	P44/02	F	78	4	Pathological ageing (Braak IV)
28	P13/08	F	88	5	Braak V, severe CAA, CVD of small vessel type
29	P69/07	M	76	5	Braak V, severe CAA
30	P86/10	M	80	5	Braak V, transitional LB pathology, mild CAA, mild small vessel disease, watershed infarction in frontal lobe

31	P01/08	F	76	6	Braak VI, severe CAA, TDP-43 proteinopathies
32	P06/05	M	64	6	Braak V1, CERAD definite, moderate CAA
33	P07/11	F	79	6	Braak VI, moderate CAA, mild hyaline arteriosclerosis, mild atherosclerosis
34	P12/10	F	56	6	Braak VI
35	P20/09	F	79	6	Braak VI, moderate small vessel disease
36	P25/16	M	88	6	Braak VI, moderate small vessel disease
37	P30/07	M	68	6	Braak VI
38	P36/10	M	72	6	Braak VI, TDP-43 proteinopathies
39	P40/10	F	62	6	Braak VI, severe CAA, limbic TDP-43 pathology, amygdala predominant LB pathology
40	P61/06	F	67	6	Braak VI, severe CAA
41	P73/08	F	61	6	Braak VI, Moderate CAA, lacunar infarct
42	P88/10	F	66	6	Braak VI, hippocampal sclerosis
43	P41/04	F	71	/	Moderate CAA
44	P44/12	M	69	/	severe CAA, diffuse white matter injury associated with severe CAA
45	SD035/21	F	63	1	NA
46	SD026/21	M	81	1	NA
47	SD042/21	M	79	2	NA
48	SD038/21	M	78	2	NA
49	SD023/21	M	85	2	NA
50	SD018/21	M	75	3	NA
51	SD050/16	F	74	3	NA
52	SD046/19	F	83	4	NA
53	SD029/18	M	82	4	NA
54	SD008/18	F	69	4	NA

Table 2. Clinical information of the elderly samples analysed in this study. Diagnosed AD samples are highlighted in yellow, while un-highlighted samples are Braak-staged but not diagnosed as AD. Hippocampus, basal ganglia and temporal lobe regions were studied for sample 1 to sample 44, only Broca's area was studies for sample 45 to sample 54.

	Patient code	Sex	Age	Cause of death	Clinical information
1	SD028/06	M	17	Severe head and neck trauma, 1b - Road traffic collision (motorcycle rider)	Brain Diffuse vascular trauma
2	SD008/09	M	25	Extensive Internal Haemorrhage,1b - Multiple Injuries,1c - Road traffic collision (driver)	No significant abnormality.
3	SD036/08	F	20	Suspension by a ligature	No significant abnormality.
4	SD031/15	F	40	N/A	N/A
5	SD029/17	M	40	N/A	N/A
6	SD004/12	M	39	Suspension by a ligature	No significant abnormality.
7	SD038/17	M	34	N/A	N/A
8	NA90/0024	M	26	Multiple injuries owing to road traffic accident	No significant abnormality.
9	SD047/15	M	19	N/A	N/A
10	SD006/09	M	25	Multiple Injuries,1b - Road traffic collision (passenger)	No significant abnormality.
11	SD016/06	M	25	Internal bleeding, Rupture of the thoracic aorta, Road traffic collision (driver)	Possible grade 3 diffuse axonal injury (DAI).
12	NA90/0270	M	21	Stab wound to chest	No significant abnormality.
13	NA93/0090	M	22	PM toxicology - hypoglycaemia.	No significant abnormality.
14	SD001/06	M	16	Suspension by a ligature	No significant abnormality.
15	SD025/05	M	28	Suspension by a ligature	No significant abnormality.

Table 3. Clinical information of the young healthy controls analysed in this work.

4.2.2 Calcification density quantification by SEM

4.2.2.1 Scanning electron microscopy

For SEM analysis, two scanning electron microscopes were utilized: the Hitachi S-3499N at the Wolfson Lab in the Archaeology Department of University College London (UCL) and the Zeiss Leo 1525 Gemini at the Electron Microscope Suite of the Materials Science Department at Imperial College London. Both microscopes operated at an accelerating voltage of 10 kV and a working distance of 10 mm to minimize uncertainty in the measurements. The Hitachi S-3499N was primarily used for quantitative imaging. The Zeiss Leo 1525 Gemini was selected for its additional in-lens detector, with the in-lens images being used for the formation of the Density-Dependent Colour (DDC) map. Oxford Instruments energy-dispersive X-ray (EDS) detectors, integrated into both machines, were employed for elemental analysis. The sample preparation methods and protocols are described in Chapter 3.1.1.5.

4.2.2.2 Data acquisition

All 69 donor samples from 4 brain regions were studied by BSE-SEM. The calcification quantification methodology employed SEM backscattered electron (BSE) imaging combined with systematic digital analysis through three critical operational parameters. First, an optimal balance of resolution and contrast was established to preserve microstructural details while maintaining adequate field coverage. Second, standardised image processing parameters were implemented across all samples to ensure measurement consistency. Third, an adjusted thresholding protocol with artefact removal mechanisms was used to enhance analytical accuracy.

SEM-BSE imaging provided atomic number-dependent contrast differentiation between mineralised (bright) and non-calcified (dark) regions. All images were acquired at 1000× magnification, achieving a 0.25 mm² field coverage while maintaining submicron resolution (>500 nm discernible). Consistent acquisition parameters included a 10 kV accelerating voltage, a 10 mm working distance, and a 60s frame integration to minimise signal noise. This configuration balanced microstructural detail capture with representative sampling requirements. The image processing workflow is shown in the visual protocol Figure 9.

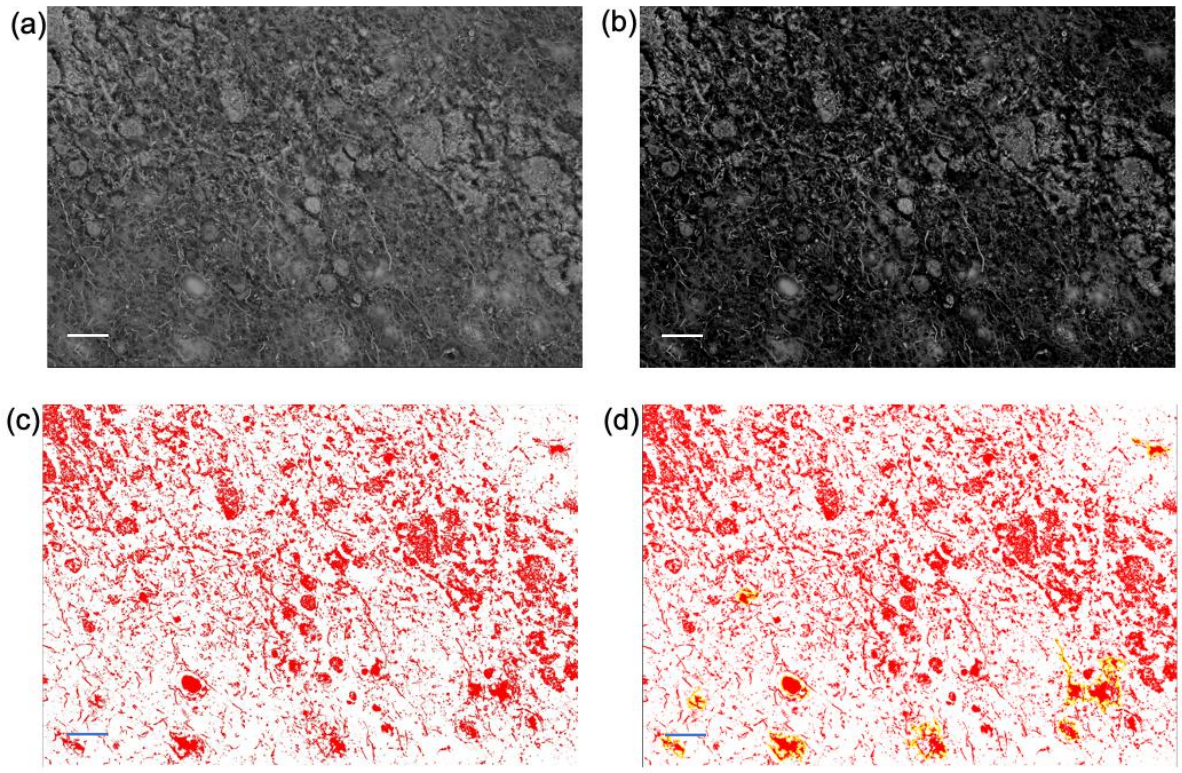

Figure 9. ImageJ threshold setting for calcification calculation. Scale bar = 100μm. (a) Original image. (b) Image after brightness and contrast adjustments. (c) Image after threshold application. (d) Manually deselect the glass region within the threshold interval, highlighted in yellow.

The pre-processing phase started with an 8-bit grayscale conversion of the original image shown in Figure 9(a), standardizing intensity values and eliminating chromatic artefacts caused by detector variations. Following this, global histogram equalisation was applied to enhance contrast uniformity without localised adjustments, as shown in Figure 9(b). This method preserved the quantitative integrity of the data while improving the visibility of calcification, particularly in samples with subtle mineralisation gradients. As a result, the bright calcification became more prominent, and background noise and imaging artefacts were effectively removed during this step.

Thresholding operations utilized an adaptive dual-layer strategy. The primary thresholding step isolated mineralised areas by applying a grayscale range of 190-255 (Figure 9(c)), which corresponds to the calcium phosphate density thresholds observed in phantoms. Manual verification was employed to identify artefacts through consensus review sessions, as the slide glass exhibited a similar colour to calcification in SEM images. To enhance the accuracy of data acquisition, the glass region was manually deselected from the thresholder image, as shown in Figure 9(d).

The high-density glass regions exhibited a similar contrast to calcifications but differed in both structure and composition. These high-density regions were analysed using energy-dispersive X-ray spectroscopy (EDS) during imaging. All excluded regions were identified and deselected based on the EDS results in combination with prior experimental experience. Some degree of uncertainty is inherently associated with this exclusion process.

ImageJ analyser will generate the area fraction statistics based on the formula:

$$\%\ Calcified\ Area = \left({Thresholder\ Pixels}/{ROI\ Pixels}\right) * 100\%$$

For each sample in which calcification was present, five measurement points were initially selected from non-band regions of calcification. These regions were chosen because the calcifications outside the band typically exhibited a more uniform and circular morphology, thereby reducing the risk of misidentifying non-cellular or irregular calcified material that may be present within the band regions shown in Fig12(a). To minimise the influence of measurement variability and potential outliers, the largest and smallest values were excluded, leaving three representative data points per sample. The mean of these three measurements was then calculated and used for subsequent analysis. This approach was adopted to improve measurement robustness while limiting variance arising from local heterogeneity in calcification morphology.

4.2.3 Statistical Analysis

All statistical analyses were conducted using OriginLab 2020 and GraphPad Prism 10 software. I employed two types of correlation analyses: Pearson's Correlation Coefficient (r) and Spearman's Rank Correlation Coefficient (ρ). Each method highlights different aspects of the data, and due to the unique nature of our dataset, relying on a single correlation approach was insufficient to draw definitive conclusions. Additionally, a Mann-Whitney two-tailed unpaired U test ($p<0.05$) was used to assess calcification size and density differences between groups. Further details are provided in Chapter 3.2.

Two distinct box plot formats were employed to best suit the nature of the datasets being analysed. For calcification size, the use of whiskers extending to mean ± 1.5 SD provided a more informative view of variability around the mean, which is important for capturing subtle morphological differences in particle dimensions across disease stages. This approach allows better visualisation of the distribution when the data are relatively symmetric and continuous. In contrast, for calcification density, whiskers representing the minimum and maximum values were used to account for the broader spread and potential skewness of the data. Since density measurements can vary widely and may include extreme values, this method ensures that full data ranges are represented, making it more appropriate for assessing regional or stage-specific variation in calcification load. Using these tailored visual strategies enabled a more accurate and meaningful interpretation of the underlying patterns in each dataset.

4.3 Results and Discussion

4.3.1 Calcification identification

The progression of Alzheimer's disease (AD) leads to significant deterioration in brain function, resulting in characteristic cognitive and neurological deficits. In this study, brain tissue samples from the basal ganglia, hippocampus, temporal lobe, and Broca's area of the elderly group were initially examined using scanning electron microscopy (SEM), an effective technique for identifying mineralisation. Micro-calcification was detected in varying degrees across approximately 80% of the cases, with regional differences in distribution and density. As illustrated in Figures 10(a) and 11(b), distinct calcified structures were commonly observed in elderly brain specimens. The elderly group included both individuals clinically diagnosed with AD and those who had not received a diagnosis but were found to be within defined Braak stages, indicating underlying AD-associated pathology.

Figure 11(c) presents a large-scale view of the mineralisation at 1000x magnification. Spherical and fibrillar structures at different stages of mineralisation are visible, indicating that mineral deposition occurs gradually over time. The variation in mineralisation levels within a single sample highlights the progressive nature of the deposition process. Figure 11(d) illustrates that the findings are consistent with previous studies on AD-related calcification. The EDS analysis focused on the orange-marked regions in DDC - SEM or bright regions in SEM images. The results confirmed that the calcifications were primarily composed of calcium phosphate, a common association with pathological deposits. The spectral data from the dense spherical formations showed distinct peaks for calcium (Ca) and phosphorus (P). Along with oxygen (O), these elements were the primary components of the calcified structures, suggesting the presence of calcium phosphate.

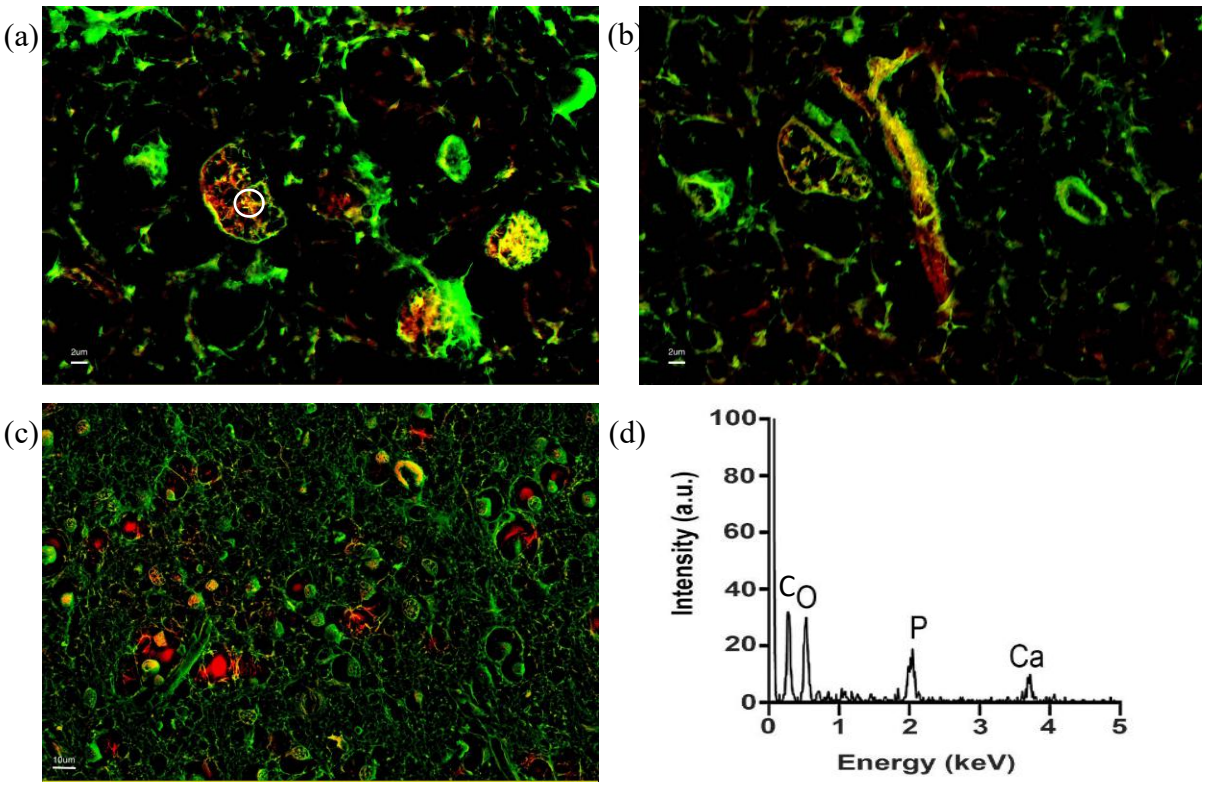

Figure 10. Density-dependent colour - scanning electron microscopy (DDC-SEM) of typical mineralisation observed in the histological section of AD brains - hippocampus area (Patient P1/08) (High-density calcification is presented in orange and organic materials in green.) (a). Spherical calcifications at 5000 magnifications with a 2 μm scale bar. (b). Fibril calcifications at 5000 magnifications with a 2 μm scale bar. (c). Large-scale view of brain tissue calcification at 1000 magnification with a 10 μm scale bar. (d). Specific EDX point spectrum of the discovered mineralisation of the highlighted area shown in Figure (a), the carbon peak shown is picked up from the carbon coating.

To confirm the presence of calcium phosphate, spectral data were interpolated across adjacent scan points to generate continuous elemental distribution maps (Figure 11(a)). The BSE-SEM image in Figure 11(a) illustrates the overall calcification pattern, delineated by a dotted line. A pronounced contrast in density is observed, with bright regions in the lower-left indicating areas of high mineral concentration, while the darker upper-right reflects less calcified tissue. The bright signals on the right side of the dotted line—highlighted by blue arrows—correspond to the glass slide, which shares similar electron density with calcified structures. This density gradient suggests a pattern of spatially confined mineral

accumulation, supporting the hypothesis of region-specific calcification (**Hypothesis 4).**

Figure 11(b)(c)(d) presents the corresponding EDS elemental maps, with calcium (Ca) in yellow, phosphorus (P) in blue, and magnesium (Mg) in green. The substantial spatial overlap between Ca and P in the lower-left region is particularly notable and consistent with the formation of calcium phosphate compounds. The sharp boundary observed in both the Ca and P channels aligns with the high-density region in Figure 11(a) image, reinforcing the interpretation that this area corresponds to a calcified deposit. In contrast, the Mg channel appears uniformly distributed across the entire field, with no concentration in the calcified region. This uniformity suggests that magnesium is a background element in the tissue matrix, not directly associated with the localised mineralisation. The combined visualisation of backscattered imaging and co-localised EDS mapping strongly supports the conclusion that the high-density spherical structures predominantly comprise calcium phosphate and exhibit a regional preference in their distribution.

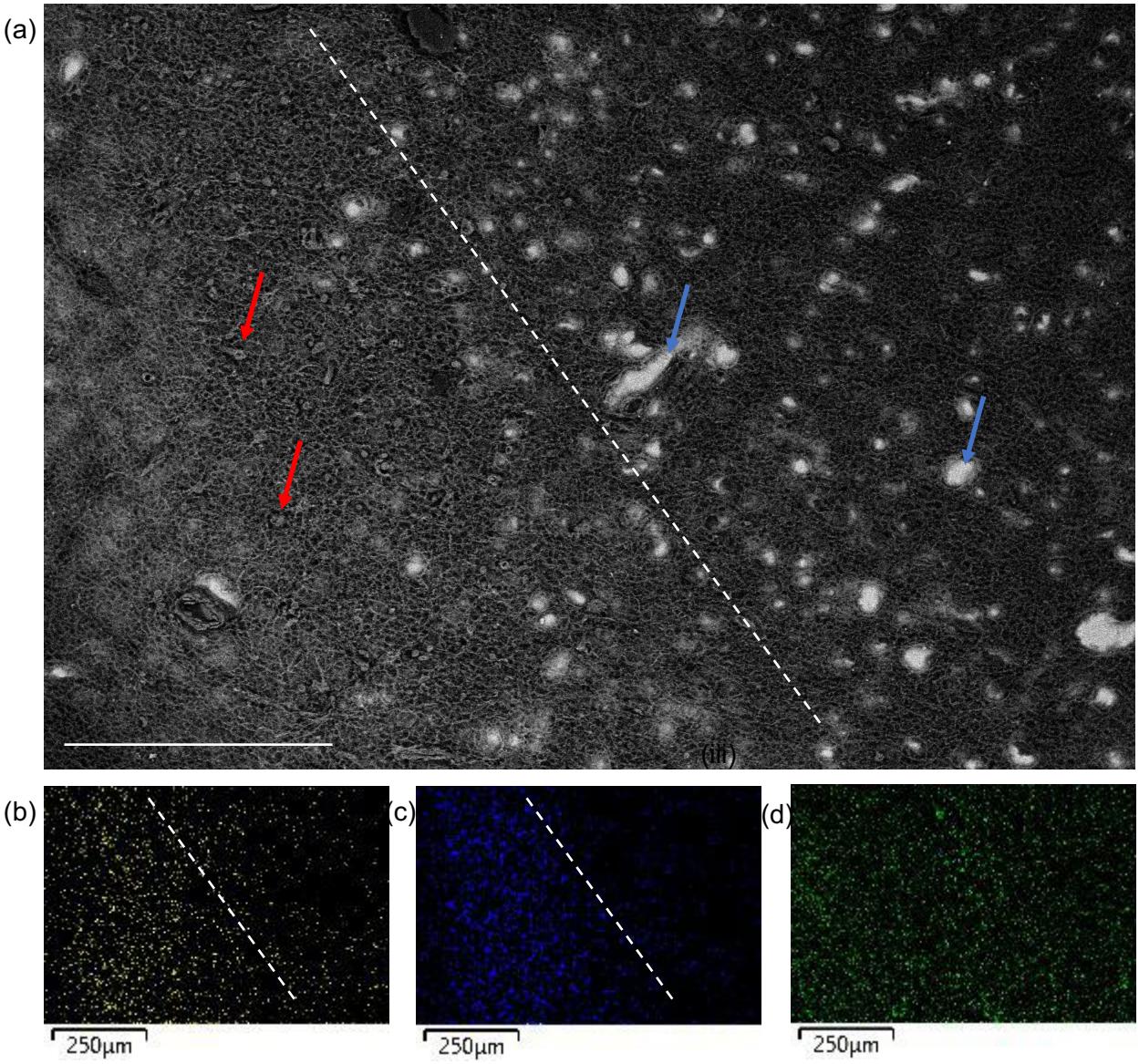

Figure 11. Composition analysis of mineralisation observed in the histological section of AD brains - hippocampus area (Patient P6/05) (a). The calcified band is close to the tissue edge, scale bar =250 µm. Red arrow high density structure = calcification, blue arrow high density structure = background glass slide. (b). Calcium channel (Ca) EDS map of Figure(a), scale bar = 250 µm. (c) Phosphorus channel (P) EDS map of Figure(a), scale bar = 250 µm. (d). Magnesium channel (Mg) EDS map of Figure(a), scale bar = 250 µm.

A clearly defined band of calcification observed at the tissue periphery, along with scattered deposits throughout the section, indicates a spatially organised rather than random pattern of mineralisation (Figure 12a). Notably, this calcification is predominantly aligned along the grey matter, densely populated with neuronal cell bodies. This localisation suggests a preferential vulnerability of neurons to pathological mineral deposition, potentially reflecting region-specific susceptibility due to metabolic activity, ion channel expression, or microenvironmental factors such as local calcium homeostasis. The presence of both peripheral bands and intra-tissue mineralisation further implies that calcification may follow structured pathways— possibly along vasculature, axonal tracts, or regions of early neurodegenerative change. Importantly, no comparable calcifications were detected in young control samples (Figure 12b), underscoring that these mineral deposits are not standard features of healthy brain tissue but emerge with pathological progression. This supports **hypothesis 1** that neuronal calcification is closely associated with Alzheimer's disease (AD) pathology, it may increase with disease progression. The absence of such features in controls also reinforces their potential utility as disease-specific markers. These findings are consistent with previous literature describing age-related brain calcifications and provide further evidence that the spatial distribution of mineralisation may reflect underlying neurodegenerative processes.

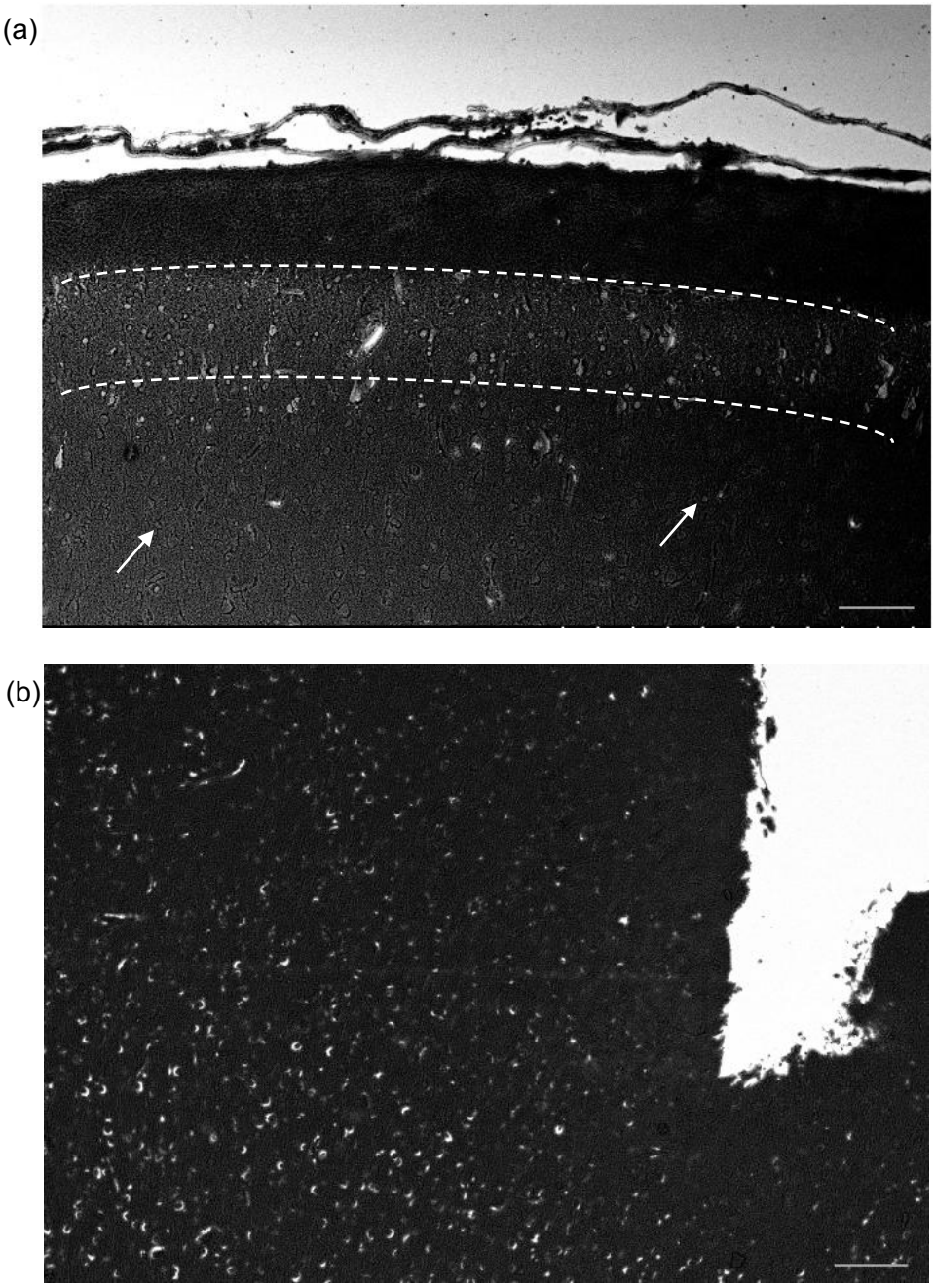

Figure 12. Backscattered - scanning electron microscopy (BSC-SEM) of the mineralisation band observed in the hippocampus histological section. (a) AD brains (P25/16), scale bar = 100 μm; calcification band highlighted with dotted line, inter-tissue calcifications are pointed by white arrows. (b) young control brain (SD004/12), scale bar = 100 μm.

The detection of calcium phosphate in both spherical and fibrillar forms, along with the observation of calcification bands across multiple samples and brain regions, suggests a consistent mineral composition among calcified deposits in Alzheimer's disease (AD)-affected brain tissue, as illustrated in Figure 12(a), Figure 13(a), and Figure 13(b). The two morphologies—spherical structures resembling neuronal somas and fibrillar formations resembling axons or dendrites—indicate that mineralisation likely occurs within or along neuronal compartments, which may disrupt neuronal connectivity and contribute to functional deterioration.

A particularly notable feature is the presence of calcification bands with neuron-like morphology in the hippocampus, basal ganglia, and temporal lobe, with a high-magnification view of the basal ganglia region shown in Figure 13(c). These bands are not randomly distributed; rather, they exhibit alignment with cytoarchitectonic layers, suggesting a layer-specific vulnerability to mineral accumulation. In both cortical and subcortical structures, these laminar patterns correspond to functionally distinct zones and synaptic networks. The localisation of calcified structures along these layers implies that calcium phosphate deposition may preferentially affect certain neuronal populations or microcircuits, potentially due to differences in regional metabolism, cell type composition, or extracellular matrix characteristics.

The consistent shape, density, and localisation of these deposits—especially their concentration in regions rich in neuronal cell bodies—further supports the hypothesis that mineralisation is not merely a passive by-product of degeneration but may be an active pathological process in AD. The morphological and compositional uniformity observed across different brain regions suggests a shared pathological mechanism underlying calcium phosphate accumulation, regardless of local anatomical variation.

These findings reinforce **hypothesis 2** that microcalcifications are forming in neuronal tissue, and it is a structural hallmark of Alzheimer's pathology and may represent a final common endpoint of regionally distributed but mechanistically convergent neurodegenerative processes. Furthermore, the spatial association between calcification bands and cytoarchitectonic boundaries highlights the importance of investigating how mineralisation may interfere with region-specific neural functions, potentially offering new insight into disease staging, symptom progression, and the identification of regionally vulnerable networks in AD.

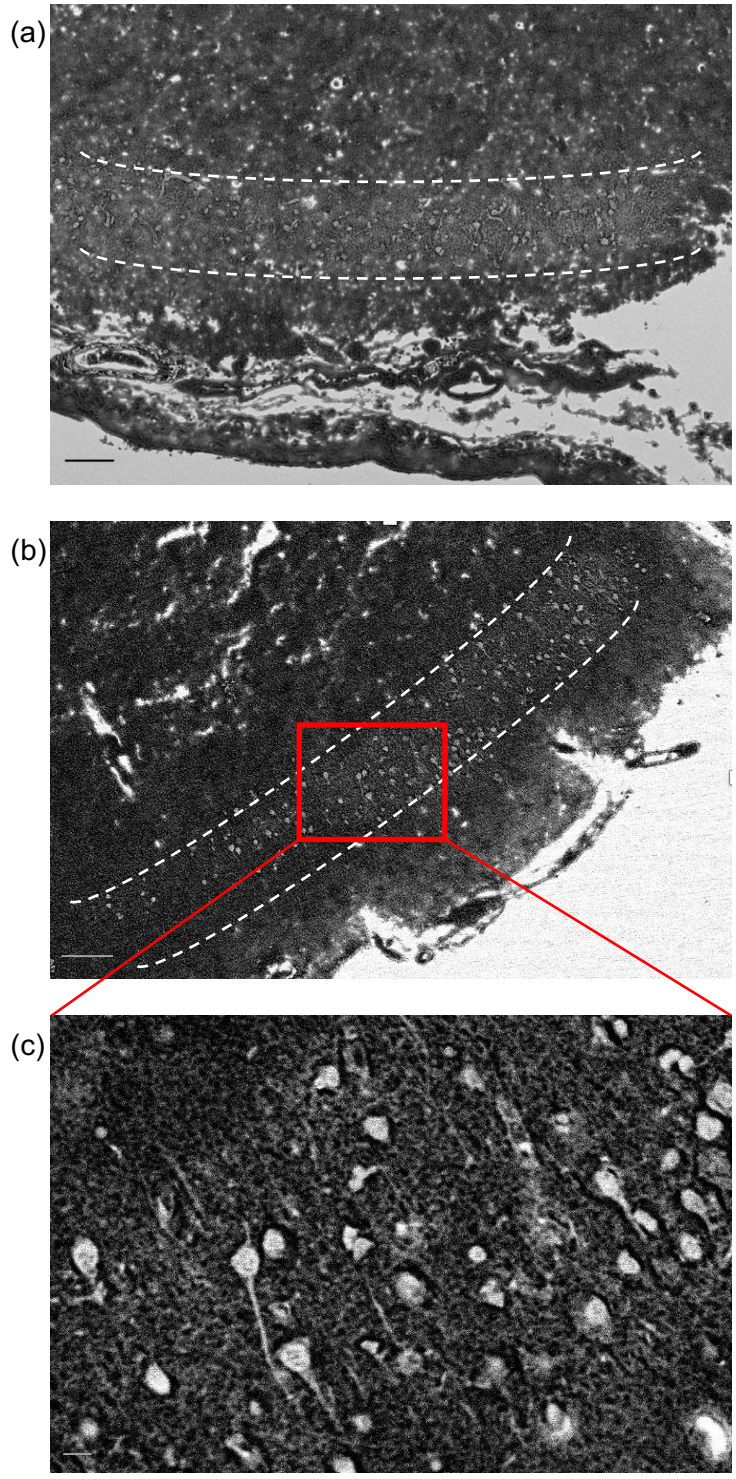

Figure 13. Backscattered - scanning electron microscopy (BSC-SEM) of the mineralisation band observed in the histological section of sample P25/16 at different brain regions. (a) Temporal lobe region, calcification band highlighted with dotted lines, scale bar = 100 μm; (b) Basal ganglia region, calcification band highlighted with dotted lines, scale bar = 100 μm; (c) high magnification of basal ganglia region, scale bar = 10 μm.

4.3.2 Calcification analysis across Braak Stages

4.3.2.1 Age, disease progression, and calcification dynamics

While age is the most significant risk factor for the onset of Alzheimer's disease (AD), its role in disease progression appears to be independent of Braak staging, which reflects the distribution of neurofibrillary pathology. For this study, the first batch of samples was obtained from the Queen's Square Brain Bank, comprising 42 samples with defined Braak stages. Notably, Braak stage IV included only one sample, while all young healthy controls (15 samples) were classified as Braak stage 0. Each Braak stage group included at least one clinically diagnosed AD case, except for Braak stage I and IV, which contained only non-diagnosed cases.

The violin plot analysis (Fig. 14) demonstrates a paradoxical stabilisation of patient ages across Braak stages I-V (mean 80 ± 3 years), contradicting expectations of accelerated pathology in older cohorts. This plateau suggests a critical threshold mechanism – once amyloid-tau cascades reach stage I, progression through intermediate stages (II-V) becomes age-insensitive, operating through self-sustaining pathological feedback loops rather than chronological ageing. Younger patients reaching terminal Braak VI (mean 69.8 years) exhibited 14.6% faster stage transitions than the I-V average, implying aggressive subtype dynamics possibly mediated by gene-driven calcium dysregulation or early-onset AD mutations. Notably, the absence of AD- related calcifications in young controls (26.5 ± 4.1 years) confirms the age-dependent initiation but not progression—a dichotomy that requires mechanistic models to separate nucleation events from pathological amplification.

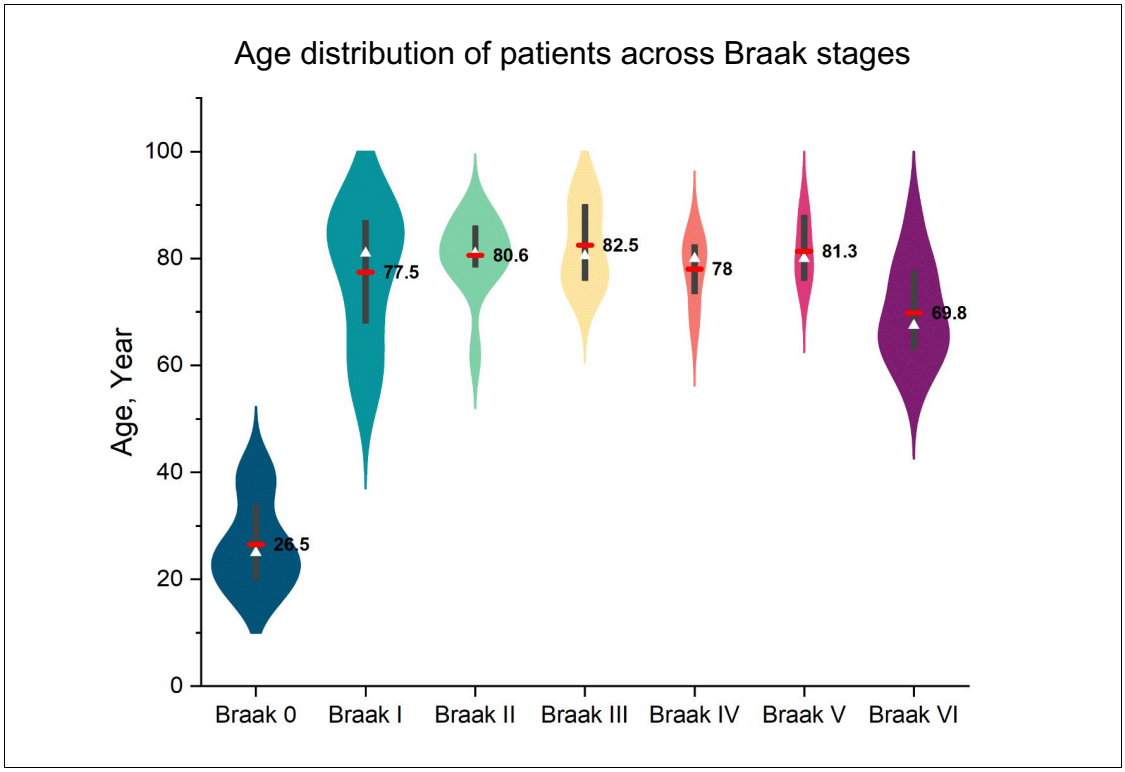

Figure 14. Violin plot of patient age distribution in each Braak group and young controls. The average age is marked as a red line with the values, and the white triangle is the median of each group.

Figure 15 presents a systematic evaluation of calcification diameters in the hippocampus and temporal lobe using stratified box plot analyses, offering insights into variations related to age and disease stage. The analysis is based on the same 42 samples used in Figure 14, as each hippocampal sample is matched with a corresponding temporal lobe sample, ensuring regional alignment and consistency across the dataset. Spherical calcifications were observed in 25 temporal lobe samples and 23 hippocampus samples. For each case, three data points were collected to calculate the average calcification size per sample.

In Figure 15(a), age-stratified groups show minimal variation in calcification size (ranging from 3–8 μm), with substantial overlap in interquartile ranges. Mann-Whitney tests were conducted both within and between groups, and no statistically significant differences were found ($p > 0.05$) in any of the comparisons. The young control group (Braak 0) exhibited no detectable calcifications, supporting their role as a pathology-free baseline. These findings suggest that while age may influence the presence of calcification, its progression appears to be primarily disease driven.

Figure 15(b) illustrates Braak stage-dependent trends, highlighting a gradual increase in calcification size within the temporal lobe, and a relative constant size at hippocampus as disease severity progresses. Although the median diameters of calcifications remained within a relatively narrow range (4–7 μm), a clear upward trend was observed, with mean size increasing from 4.2 ± 0.5 μm in Braak I to 7.8 ± 1.1 μm in Braak VI. This suggests that as AD pathology advances, not only does calcification become more prevalent, but the deposits themselves also grow in size, possibly reflecting prolonged or intensified mineral accumulation.

Statistical analysis revealed a significant difference between Braak I and Braak V in the temporal lobe ($p < 0.05$*), indicating a measurable shift in calcification characteristics at mid-to-late stages of the disease. Additionally, a significant difference in calcification size was detected between the hippocampus and temporal lobe within Braak V ($p < 0.05$*), suggesting region-specific mineralisation dynamics at this disease stage. However, no statistically significant differences were identified within or across other Braak stages, possibly due to inter-individual variability and the limited sample size, particularly in Braak IV, which weakened statistical power and limited correlation analysis.

These findings support the notion that calcification size may serve as an additional morphological marker of AD progression. The data imply that microcalcifications, beyond their presence, undergo structural changes as pathology intensifies, which may reflect evolving tissue microenvironments or shifting interactions with degenerating neurons and proteins such as pTau.

However, a decrease in calcification size was observed in the temporal lobe from Braak V to Braak VI, deviating from the otherwise progressive enlargement trend and suggesting an unconventional pattern. This unexpected reduction may not reflect a true biological reversal but is more likely attributable to the limited sample size within the Braak VI group, which may reduce statistical reliability and amplify variability.

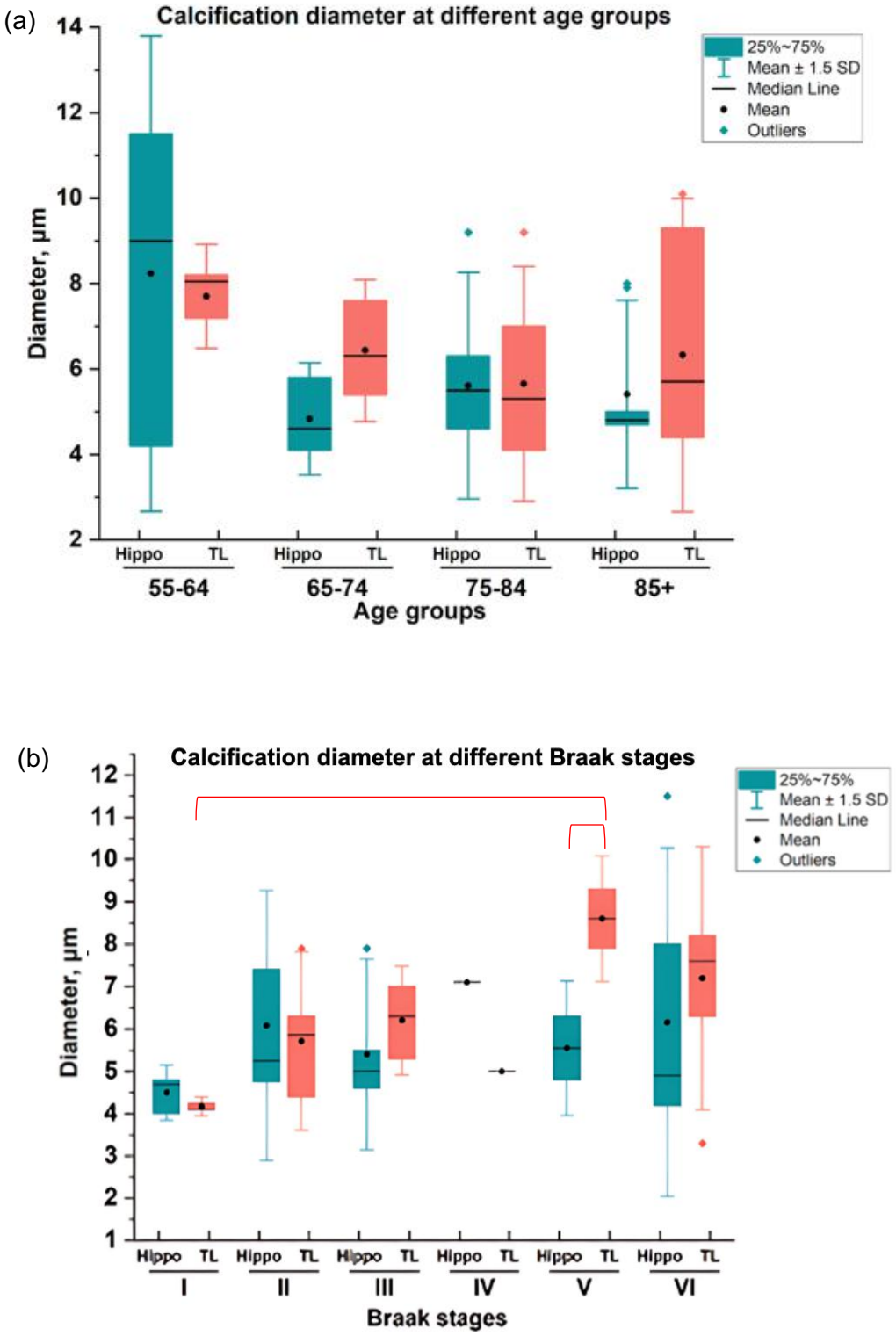

Figure 15. Box charts analyse the calcification diameter observed in the hippocampus and temporal lobe areas based on different factors. The red connection lines indicate a significant difference $p<0.05$. (a) Patients are grouped based on age. (b) Patients are grouped on the Braak stages.

4.3.3 Calcification Density at Progressive Disease Stages in Different Brain Areas

Based on the calcification size analysis, no clear or consistent relationship was found between calcification diameter and AD pathophysiology, particularly across the different Braak stages. Consequently, the focus of the investigation shifted toward evaluating calcification density in relation to disease progression across multiple brain regions. To support this analysis, 10 age-matched Broca's area samples from Braak stages I–IV were added to the study, as this region is less directly associated with early-stage AD pathology. Given that the Broca area, responsible for language processing, is typically affected in later stages of the disease, it serves as a meaningful comparative region for assessing regional vulnerability. However, due to sample availability constraints and quality control considerations, only samples from four Braak stages were ultimately included in the analysis.

A general increasing trend in calcification density was observed across all four brain regions examined (Figure 16), based on a total of 24 cases distributed across Braak Stages I–VI (n = 5, 5, 5, 1, 3, 5, respectively). For each case, the data point represents the average of three independent measurements, ensuring consistency and reducing sampling variability.

Pearson correlation analyses were conducted to assess the linear relationship between Braak stages and calcification density across different brain regions. The resulting Pearson correlation coefficients (r) were as follows: Basal ganglia: $r = 0.4080$; Temporal lobe: $r = 0.2078$; Hippocampus: $r = 0.2608$; Broca's area: $r = 0.1474$. These values indicate a positive linear correlation in all four regions, meaning that calcification density tends to increase with disease progression. However, the strength of the correlation varies, with the basal ganglia showing the strongest association, followed by the hippocampus and temporal lobe, while the Broca's area exhibits only a weak correlation. The relatively higher correlation in the basal ganglia suggesting that it is more susceptible to pathological mineral accumulation in advanced AD stages.

Moreover, the positive correlations are further supported by the results of statistical tests comparing each region's calcification density to baseline levels. Significant differences were observed in all four regions, with p-values of <0.0001 for the basal ganglia and temporal lobe, $p < 0.05$ for the hippocampus, and $p < 0.01$ for the Broca's area. These findings reinforce the conclusion that calcification density

increases with disease progression, and that this trend is statistically robust across anatomically and functionally distinct brain regions.

However, all the Pearson correlation coefficients (r) obtained across the studied brain regions were less than 0.5, indicating weak linear relationships between calcification density and Braak stage progression. While the correlations were positive, suggesting that calcification generally increases with disease severity. The low r-values imply that the linear association is not strong and may not fully capture the nature of the relationship.

To account for potential non-linear but consistent trends, a monotonic relationship analysis was subsequently performed using non-parametric Spearman's rank correlation (ρ). These approaches assess whether calcification density tends to increase consistently with Braak stages, regardless of whether the change occurs at a constant rate. This allowed for a more comprehensive evaluation of how mineralisation correlates with AD progression, particularly in datasets that may not meet the assumptions of normality or linearity.

The Spearman correlation coefficients (ρ) were calculated to evaluate the monotonic relationships between Braak stage progression and calcification density across four brain regions. The results revealed strong positive correlations in the basal ganglia ($\rho = 0.8396$), temporal lobe ($\rho = 0.7459$), and Broca's area ($\rho = 0.8335$), while a moderate correlation was observed in the hippocampus ($\rho = 0.5361$). These values suggest that, as Braak stage increases, calcification density tends to increase consistently across all regions—regardless of whether the rate of increase is linear.

The statistical significance of these correlations was confirmed with p-values of <0.0001 for the basal ganglia and temporal lobe, $p < 0.01$ for the hippocampus, and $p < 0.05$ for the Broca's area. These results indicate that the observed associations are unlikely to be due to chance and reinforce the **hypothesis 1 that calcification density increases progressively with Alzheimer's disease severity**, and they highlight region-specific trends in vulnerability to pathological mineralisation. The presence of statistically significant correlations across all regions, despite differences in anatomical function and calcification patterns, suggests that microcalcification may serve as a generalisable marker of neurodegenerative progression. Moreover, the

strength of statistical significance supports the reliability of the findings and provides confidence in the consistency of the underlying biological phenomenon.

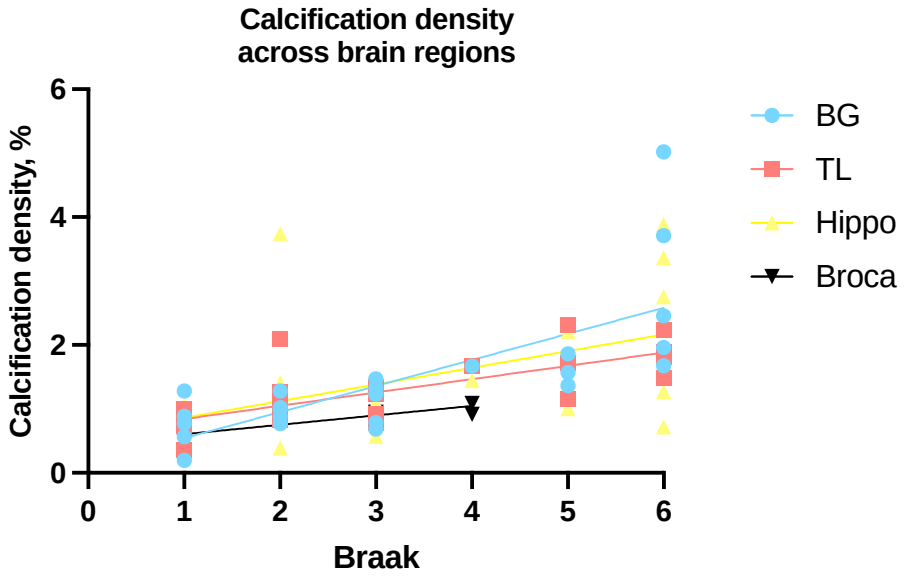

Figure 16: scatter plot of calcification density across brain regions with Braak stage progression.

The same set of data was then utilised to conduct Braak stage–specific investigations, this stratified analysis reveals distinct regional patterns of mineralisation that correlate with Alzheimer's disease (AD) pathology, supporting **Hypothesis 1**. Moreover, the presence of measurable calcification in samples from early Braak stages (I–III) suggests that mineral accumulation may begin during the initial phases of disease development. This early-stage mineralisation could reflect subtle pathological changes preceding overt clinical symptoms, indicating that brain calcification has potential as a sensitive early biomarker for neurodegenerative processes in AD.

The basal ganglia (Figure 17a) exhibit a stage-dependent increase in mineralisation, with below 1% median calcification at Braak Stage I, progressively rising to approximately 2.5% by Stage VI. A gradual accumulation (1.5% at Stage IV) precedes a marked surge between Stages V (1.5%) and VI (2.5%), indicating heightened vulnerability to pathological mineralisation in late-stage AD. This trend correlates with progressive motor and executive dysfunction, aligning with the basal ganglia's role in movement coordination and procedural memory. Notably, a wide range of calcification values was observed among Braak VI samples, indicating

significant heterogeneity in mineralisation at this stage of the disease. This variation may reflect individual differences in disease severity that influence the propensity for calcification. Several cases displayed values substantially higher than the median, suggesting that certain individuals or subregions of the basal ganglia may be particularly susceptible to intense mineral accumulation. While calcification is generally more pronounced in late-stage Alzheimer's disease, these findings highlight that its distribution and severity are not uniform across all patients or brain areas, underscoring the complexity and variability of AD pathology. Statistical analysis revealed a significant difference in calcification levels between Braak Stage I and Braak Stage VI ($p < 0.01$), Braak II and Braak VI ($p<0.01$), and Braak III and Braak VI ($p<0.01$) indicating that the extent of macrocalcification increases markedly with advancing stages of Alzheimer's disease.

The temporal lobe (Figure 17(b)) exhibits a relatively lower calcification density compared to the basal ganglia. However, a gradual increase is observed, with the median calcification density rising from 0.8% at Braak I to 1.8% at Braak VI. Despite the overall modest range, a statistically significant difference is detected between Braak I and Braak IV ($p < 0.01$), indicating that mineralisation in the temporal lobe may still reflect disease progression, albeit to a lesser extent than in more heavily affected regions, such as basal ganglia.

Calcification in the hippocampus (Figure 17(c)) shows no clear stage-dependent trend, with median values ranging from 1.0% to 2.5% across Braak Stages I–VI (excluding Braak IV due to the inclusion of only one case). Notably, Braak Stage II exhibits a wide variability in calcification levels, suggesting considerable inter-individual differences at this early stage. No statistically significant differences were observed between any of the Braak stages. This indicates that, within the non-dentate gyrus regions of the hippocampus analysed, calcification may not follow a consistent progression pattern throughout Alzheimer's disease. Alternatively, the limited sample size, especially in the middle to late Braak stages, may reduce the statistical power to detect subtle or non-linear changes.

Compared to other regions, Broca's area (Figure 17(d)) demonstrates strong resistance to calcification, with a stable median (between 0.5%~1.0%) from Braak Stages I to IV. This pattern aligns with clinical observations that syntactic processing remains relatively preserved until the terminal stages of AD. The underlying protective

mechanisms may involve a unique vascular architecture or the differential expression of calcium-binding proteins within the microenvironment of the inferior frontal gyrus.

The observed regional disparities in calcification highlight its uneven contribution to AD pathology. Broca's area remains largely unaffected while the basal ganglia, and temporal lobe exhibit significant increases, particularly in later Braak stages. These findings suggest that calcification may play a role in AD-related neurodegeneration, particularly in areas involved in memory, sensory processing, and motor functions. The temporal progression of mineralisation also underscores the potential of the calcification burden as a biomarker for disease staging and therapeutic targeting.

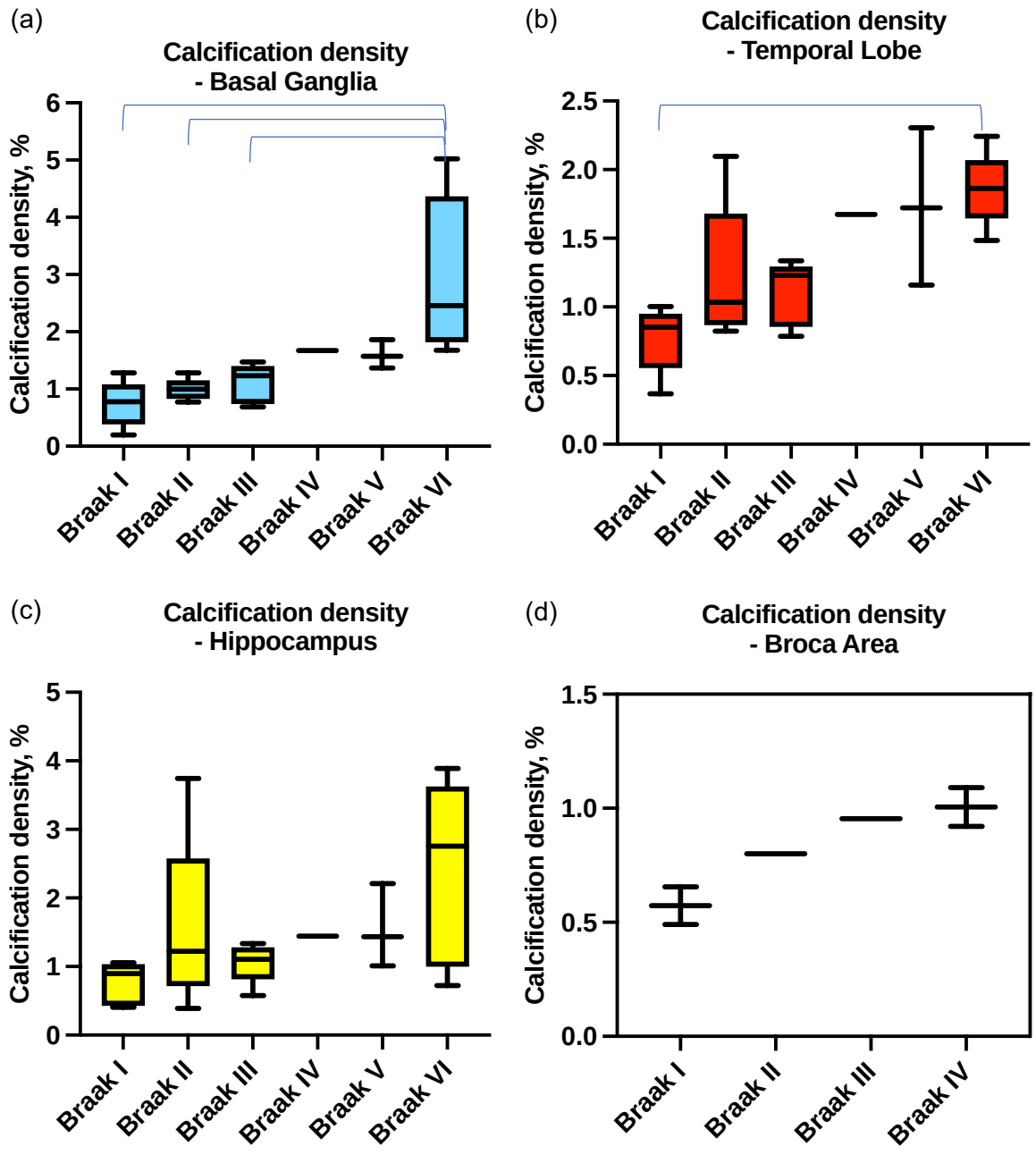

Figure 17: Box chart analysis of calcification density across brain regions with Braak stage progression, blue connection line indicating $p<0.01$.(a) Basal Ganglia region; (b) Temporal lobe region; (c) Hippocampus region; and (d) Broca's Area.

The two-step Braak stage grouping method is widely used in Alzheimer's disease (AD) research as an effective framework for hypothesis testing. It links the progression of neurofibrillary tangles to clinical symptoms, allowing researchers to distinguish between early (Braak I–II), intermediate (III–IV), and late (V–VI) stages of AD. Figure 18 illustrates the distribution of calcification levels across three brain regions—basal ganglia, hippocampus, and temporal lobe—and their association with these grouped Braak stages. The Broca's area was excluded from this analysis due to the limited number of samples and the low levels of calcification observed in that region.

Significant differences in calcification density within the basal ganglia were observed between both the middle (Braak III–IV) and late (Braak V–VI) stages ($p < 0.01$), as well as between the early (Braak I–II) and late stages ($p < 0.001$). These findings indicate a notable increase in mineralisation as Alzheimer's disease progresses into its advanced phases, reinforcing the association between calcification accumulation and disease severity. However, no statistically significant difference was identified between the early and middle stages. This lack of distinction suggests that mineralisation in the basal ganglia may remain relatively stable or gradual during the initial to mid-phases of disease development, with a more pronounced escalation occurring only during the late stages. This pattern implies that pathological calcification in the basal ganglia is likely a late-stage phenomenon, potentially linked to advanced neurodegenerative processes, such as widespread neuronal loss, glial activation, or changes in the local ionic environment. These results support the hypothesis that calcification may serve as a progressive marker of disease burden, particularly in subcortical regions.

The temporal lobe displays a trend comparable to that of the basal ganglia, with calcification levels remaining relatively stable during the early (Braak I–II) and middle (Braak III–IV) stages, followed by a notable increase in the late stages (Braak V–VI). This progression is reflected in the statistical analysis, which shows significant differences between the middle and late stages ($p < 0.05$) and between the early and late stages ($p < 0.01$). The magnitude of change and statistical significance in the temporal lobe is less pronounced compared to the basal ganglia. While both regions demonstrate late-stage calcification as a marker of advancing pathology, the basal ganglia exhibit a steeper and more statistically robust increase, suggesting it may be more susceptible to or indicative of pathological mineralisation in

Alzheimer's disease. This comparison reinforces the region-specific nature of calcification dynamics and highlights the basal ganglia as a potentially more sensitive region for detecting mineral-related progression in AD.

Hippocampus shows no significant differences in calcification across the different Braak stages, as the box plot reflects relatively stable calcification across early, middle, and late stages. This finding is consistent with the results from the Mann-Whitney test ($p>0.05$). This suggests that calcification may not be a primary factor in hippocampal degeneration during AD progression. It implies that other pathological processes, such as tau and amyloid accumulation, may have a more dominant role in the Hippocampus, despite its crucial involvement in memory processing and cognitive decline.

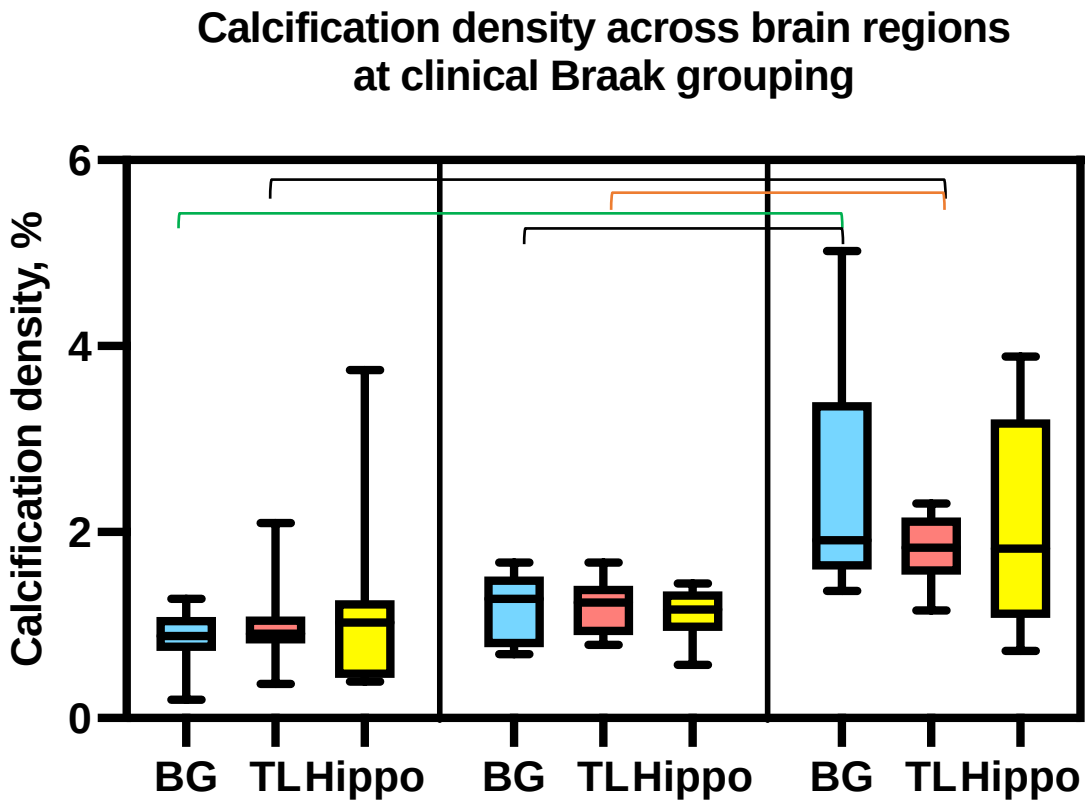

Figure 18. Box plot analysis of calcification density across brain regions in relation to clinical Braak stage progression. Orange connection lines indicate statistically significant differences at $p < 0.05$, black lines indicate $p < 0.01$, and green lines indicate $p < 0.001$. The basal ganglia region is shown in blue, the temporal lobe region in red, and the hippocampus region in yellow.

4.4 Conclusion and Future work

The results of this study confirmed the presence of micro-level calcium phosphate minerals in the brains of both pre-clinical and clinically diagnosed Alzheimer's disease (AD) patients, while no mineral deposits were detected in young control samples, revealing that calcification is associated with AD pathology rather than normal ageing. Neuron-like calcifications were consistently observed across all four studied regions—basal ganglia, hippocampus, temporal lobe, and Broca's area—indicating a widespread yet regionally distinct mineralisation pattern.

Importantly, the findings suggest that age alone does not drive disease progression but may instead influence the timing of onset. Analysis of calcification morphology showed that calcification size remains relatively constant across Braak stages, whereas **calcification density demonstrates a progressive increase with advancing pathology, following a monatomic relationship (Hypothesis 1).** This trend highlights density, rather than size, as a more reliable indicator of disease severity. Notably, this study is the first to quantify calcification density across Braak stages, providing novel insights into the relationship between mineralisation and disease progression.

Statistical analyses revealed significant increases in calcification density in the basal ganglia and temporal lobe between the late stages of AD (Braak V–VI) and early stages (Braak I-II and Braak III-IV), suggesting that these regions may be particularly vulnerable to late-stage pathological mineral accumulation. Collectively, these results support the role of brain calcification as a progressive and region-specific feature of AD, with potential implications for early detection and disease monitoring.

This study successfully achieved its primary objective of investigating the correlation between brain calcification and pathological progression of Alzheimer's disease, as defined by Braak staging. However, more work must be done to improve the robustness and interpretability of future research. Firstly, using a larger and more evenly distributed cohort would help strengthen statistical reliability and validate the observed trends. The imbalanced sample distribution across Braak stages—particularly the presence of only one sample at Braak stage IV—limited the statistical power of the analyses. Several observed differences in calcification density approached, but did not reach, conventional significance thresholds ($p \approx 0.05$), suggesting that some findings may be sensitive to sample variability. Secondly,

including additional areas—particularly those implicated in other neurodegenerative disorders—could provide a more comprehensive understanding of whether microcalcifications are specific to AD or reflect broader pathological processes. This would also help clarify whether calcification patterns are region-specific, disease-specific, or shared among multiple forms of neurodegeneration.

In conclusion, this work represents the first quantitative assessment of brain calcification in relation to pathological AD progression, specifically across Braak stages. The detection of microcalcifications in early-stage AD and their positive correlation with disease severity lays a strong foundation for exploring the pathological role of mineralisation in AD progression. Quantitative analysis demonstrated a stage-dependent accumulation of calcification, most notably in the basal ganglia, where a marked increase was observed in advanced Braak stages. Interestingly, even regions with relatively low calcification levels, such as Broca's area, showed a measurable correlation with disease progression, suggesting that micro-mineralisation may serve as a sensitive marker of underlying neurodegenerative changes. Across all examined brain regions, the consistent rise in calcification with AD severity supports the hypothesis that brain mineralisation is not merely a by-product but may represent a contributing factor to the disease pathology.

Chapter 5: Calcification simulation in Simulated Body Fluid (SBF)

5.1 Introduction

Calcifications have been consistently observed in AD-associated brain regions, including the basal ganglia, hippocampus, and temporal lobe, where many of the deposits exhibit neuron-like morphologies, particularly in cortical areas, as detailed in Chapter 4. These high-density, shape-specific mineralisation suggest a potential preference for certain cell types or protein environments, implicating them in the progression of Alzheimer's disease. The regional and morphological consistency raises the possibility that calcification formation is not random but may be influenced by the biochemical composition or cellular architecture of specific brain areas.

To further explore the mechanisms underlying calcification formation, a simulation model was developed to investigate mineral deposition at both the tissue and protein levels.

Simulated body fluid (SBF) has been widely used for the in vitro evaluation of the bioactivity of *implantable materials, as it mimics the ionic composition of human blood plasma. In this context, the formation of a bone-like apatite layer on material surfaces following immersion in SBF is considered predictive of bone-bonding ability in vivo. Conventional SBF (c-SBF) and its revised formulations, including revised SBF (r-SBF), were originally developed to match the total or dissociated ion concentrations of healthy human plasma more closely and to improve the reliability of in vitro bioactivity testing.*

In my study, r-SBF was not employed for the assessment of material bioactivity, but instead as a disease-relevant simulation environment to investigate mechanisms of mineral deposition associated with Alzheimer's disease. Unlike conventional SBF, which represents healthy physiological conditions, the use of r-SBF was intended to approximate altered ionic and physicochemical conditions that may be present in pathological states. This approach allowed the investigation of mineral deposition at both tissue and protein levels under conditions more relevant to AD pathology, rather than to normal bone–material interactions.

The ion concentration is listed in Table 4 [228]. Understanding these preferences is crucial for clarifying how microcalcifications form and spread in the AD brain and may provide insight into the factors that drive their selective

accumulation. Then, leading to **Hypothesis 2 (AD-like mineralisation can form in neuronal tissues under conditions mimicking the body's internal fluid environment)** and **Hypothesis 3 (The mineralisation environment selectively degrades phosphorylated proteins while leaving tau proteins intact).**

Ions	Amount in r-SBF/mM
Na^{+}	142.0
K^{+}	5.0
Mg^{2+}	1.5
Ca^{2+}	2.5
Cl^{-}	103.0
HCO_3^{-}	27.0
HPO_4^{2-}	1.0
SO_4^{2-}	0.5

Table 4. Ion concentration of the revised SBF (r-SBF) used for simulation.

5.2 Materials and methods

5.2.1 Samples

5.2.1.1 Animal samples

Three six-month-old mice were euthanised in accordance with institutional ethical standards using an approved protocol, specifically carbon dioxide (CO_2) inhalation followed by cervical dislocation to ensure rapid and humane death. Immediately after euthanasia, the skull was carefully opened using fine microscissors and forceps, and the brain was gently extracted to avoid mechanical disruption. Mice were selected for this experiment because they provide a genetically controllable, biologically relevant, and ethically feasible in vivo model.

The freshly harvested tissues were then immersed in 4% paraformaldehyde (PFA) in phosphate-buffered saline (PBS) at 4 °C for 24 to 48 hours to ensure complete fixation. This fixation step is critical for maintaining tissue architecture and preventing post-mortem degradation.

For paraffin embedding, the fixed brains were dehydrated through a graded ethanol series (70%, 80%, 95%, and 100%), then cleared in xylene, and subsequently embedded in molten paraffin wax. Tissue blocks were sectioned using a rotary microtome to a thickness of 4 μm, the same as all the tissue samples used in this thesis.

The resulting sections were mounted on positively charged glass slides to promote strong tissue adhesion and then dried overnight at 37 °C. Prepared slides were stored at room temperature until they were ready for downstream use.

5.2.1.2 Protein samples

This research employed commercially available tau proteins to model calcification at the protein level and investigate the underlying mechanisms. The selected commercial proteins included phosphorylated recombinant human tau-441 (ab269026), tau-383, and phosphorylated tau (pTau) 199 from Abcam. These proteins were chosen for their relevance to Alzheimer's Disease (AD) research, where tau modifications play a crucial role in disease pathology. Table 5 provides details for each selected protein.

Protein	Details
Phosphorylated variant, tau-441	It contains phosphate groups at specific residues, mimicking the hyperphosphorylation observed in AD. Hyperphosphorylation contributes to tau aggregation and neuronal dysfunction, making this variant essential for studying phosphorylation's role in calcification.
Tau-383	A shorter isoform consisting of 383 amino acids, results from alternative splicing and is also implicated in AD,
Phosphorylated tau (pTau) 199	A featuring phosphorylation at threonine 199, was examined due to its association with tau pathogenesis. Investigating this specific phosphorylation site provided insights into its potential role in neuronal mineral deposition.

Table 5. Details of each protein selected.

5.2.2 Simulation models

5.2.2.1 Tissue-level simulation model setting

To investigate the underlying mechanisms of brain calcification and identify the conditions that facilitate calcium phosphate deposition, a simulation model was developed to replicate the physiological environment in which mineralisation may occur. The setup for the tissue-level simulation model is illustrated in Figure 19. The revised simulated body fluid (r-SBF) solution was freshly prepared on the day of the experiment to ensure optimal ion stability and mimic in vivo conditions as closely as possible. The reagents and the corresponded amount are listed in Table 6.

To prepare the revised simulated body fluid (r-SBF), all glassware and tools are first cleaned with 1.0 M HCl, neutral detergent, and thoroughly rinsed with distilled water to remove any contaminants. About 350 mL of distilled water is added to a 500 mL beaker, stirred continuously at 36.5°C using a magnetic stir bar. HEPES buffer is dissolved separately in 50 mL of distilled water and added to the main solution. The remaining reagents are added one at a time, ensuring each is fully dissolved before the next is introduced. Once all reagents are incorporated, the pH is adjusted to 7.40 at 36.5°C using 1.0 M NaOH. The solution is then transferred to a 500 mL volumetric flask, topped up to volume with distilled water, and allowed to cool to room temperature. The prepared r-SBF can be stored at 5°C for up to 4 weeks. It is important to check and adjust the pH before every use.

Prior to immersion in the prepared r-SBF solution, all tissue samples were deparaffinised and rehydrated to restore their aqueous permeability and ensure effective interaction with the simulated fluid. The detailed procedure for this process is outlined in Chapter 3.1.3.3. To maintain physiological relevance, the samples were then incubated in the r-SBF within a temperature-controlled shaking chamber set at 37°C, closely mimicking human body temperature. Continuous agitation (once/day) during incubation enhanced ion exchange and diffusion across the tissue surface, promoting uniform exposure and supporting efficient mineral deposition. For the mineralisation study, samples were incubated in r-SBF for two different time periods—2 days and 4 days—to assess the progression and extent of calcium phosphate deposition over time.

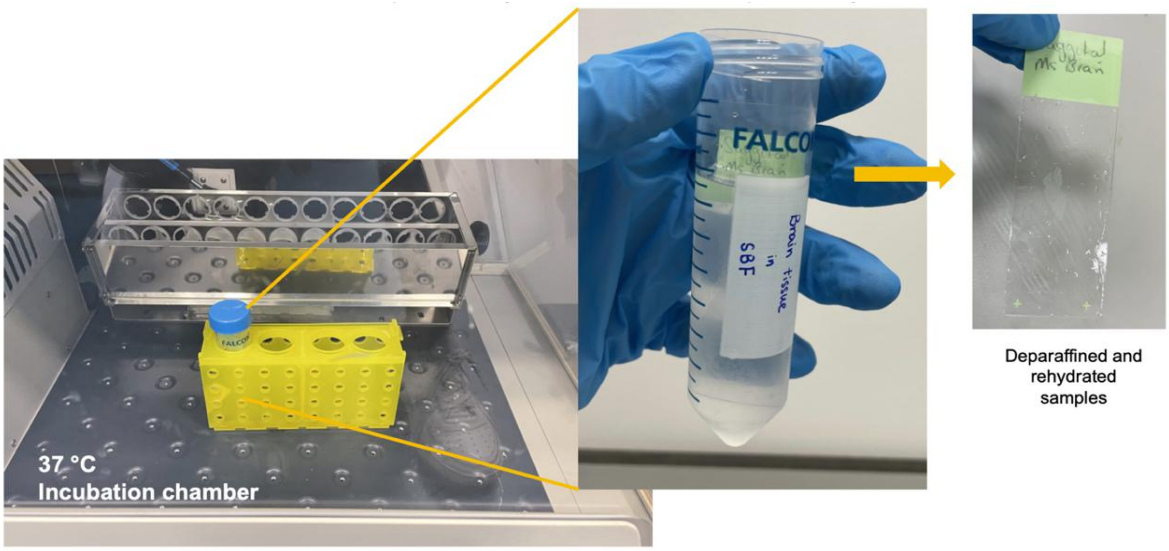

Figure 19. Experimental Setup for Calcification Simulation. The image depicts incubating deparaffinised and rehydrated brain tissue samples in r-SBF. The samples are placed in a 37°C incubation chamber to mimic physiological conditions, promoting the formation of calcifications in brain tissues.

Reagents	Amount
NaCl	5.403g
$NaHCO_3$	0.740g
Na_2CO_3	2.046g
KCl	0.225g
K_2HPO_4	0.176g
$MgCl_2 \cdot 6H_2O$	0.311g
$CaCl_2$	0.293g
Na_2SO_4	0.072g
HEPES	11.928g

Table 6. SBF reagents list and corresponded amount for a 500ml solution preparation.

5.3.2.2 Protein-level simulation model setting

Protein mineralisation was investigated in parallel with tissue-level simulations, using the same r-SBF solution to ensure consistency in experimental conditions. Two approaches were employed to simulate protein-based calcification. In the first method, 5μl protein was directly applied to TEM grids before immersion in r-SBF (Figure 20). This approach ensured that the protein remained fixed on the grid throughout the simulation, thereby minimising sample loss and improving imaging reliability during transmission electron microscopy (TEM) analysis.

In the second method, protein was first incubated freely in r-SBF to allow for mineral deposition in solution, after which the 5μl concentrated protein-mineral complex was applied to the TEM grid. This approach aimed to maximise the extent of mineralisation, as the protein was fully exposed to the mineralising environment.

To assess the temporal progression of calcium phosphate deposition, samples from both methods were incubated for two time points—24 hours and 48 hours—allowing comparison of mineral formation at different stages.

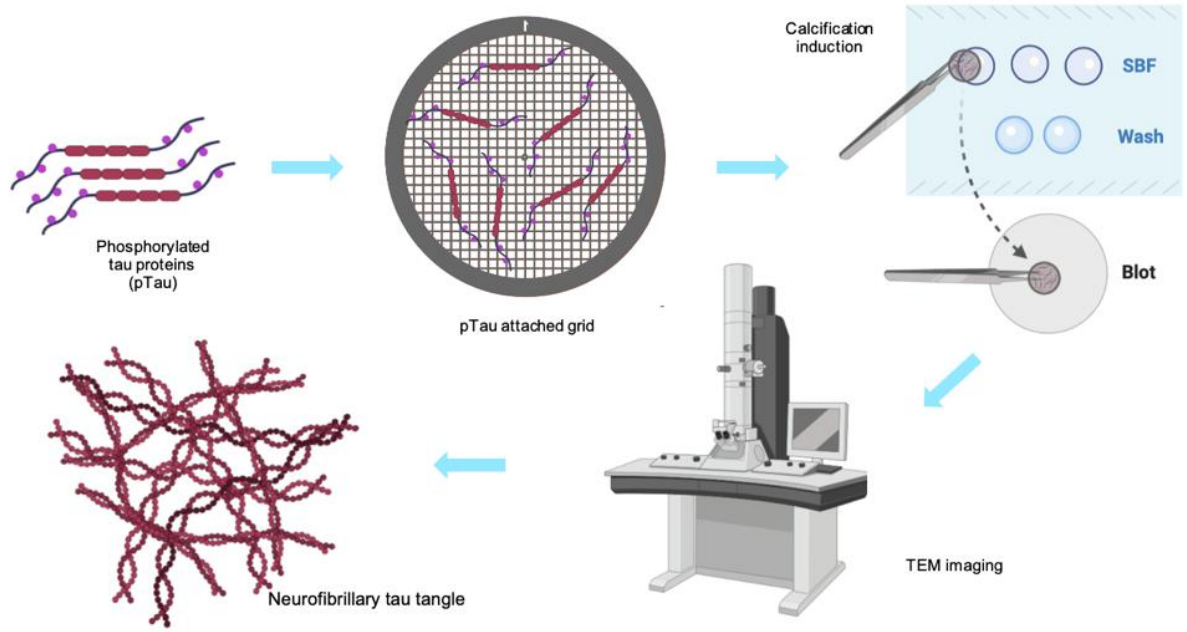

Figure 20. Schematic Representation of Phosphorylated Tau (pTau) and Tau Proteins Calcification and Imaging Process. This figure illustrates the experimental workflow for studying the calcification of phosphorylated tau (pTau) protein.

5.2.3 SEM sample preparation

After removal from the r-SBF solution, the slides were thoroughly washed to eliminate any superficial, non-specifically bound mineral residues. Each sample underwent six consecutive 5-minute washes in distilled water, followed by a final 30-second rinse under running distilled water to ensure complete removal of loosely attached deposits. Proper washing is critical to avoid interference from surface residues, which could compromise the accuracy of downstream analysis focused on targeted mineralisation.

Following the wash, slides were processed according to the SEM sample preparation protocol described in Chapter 3.1.1.5.

5.2.4 TEM sample preparation

The copper grids were placed on droplets of protein solutions, with the dark side facing down, for five minutes to facilitate protein adherence. After incubation, the grids underwent three consecutive five-minute washes with distilled water to remove excess protein, ensuring accurate imaging. Since calcifications were naturally visible under electron microscopy, additional staining was unnecessary. Following air-drying at room temperature to preserve mineral deposits, the grids were examined using TEM, enabling high-resolution visualisation of calcified and non-calcified tau structures. Samples were stored in a dedicated container to prevent contamination before imaging.

Transmission Electron Microscopy (TEM) samples were prepared on copper grids with carbon film, providing a stable substrate for analysis. The protocol involved preparing protein solutions (20 µL total volume) with r-SBF, a solution that closely replicates human extracellular fluid, creating a physiologically relevant environment for mineralisation studies.

5.2.5 Sodium Dodecyl Sulfate–Polyacrylamide Gel Electrophoresis (SDS-PAGE)

5.2.5.1 Sample preparation

Phosphorylated tau441 (p-Tau) proteins were prepared in both mineralised and non-mineralised forms to evaluate potential structural and molecular alterations induced by calcium phosphate deposition. Mineralisation was achieved by incubating pure tau solutions in simulated body fluid (r-SBF) for 1 day at 37 °C under static conditions, allowing controlled precipitation of phosphate minerals onto the protein surface. After incubation, samples were centrifuged at 12,000 × g for 10 min, and the supernatant and the final protein pellets were collected for analysis. To ensure comparability, equal volume (10μL per lane) of phosphorylated tau and their mineralised counterparts were loaded for analysis.

5.2.5.2 Gel Electrophoresis

Sodium dodecyl sulfate–polyacrylamide gel electrophoresis (SDS-PAGE) was performed at room temperature on a precast 4-20% gradient gel. Samples were denatured by mixing with 10μL 2× Laemmli sample buffer (containing 10% β-mercaptoethanol, 2% SDS, 10% glycerol, and 0.002% bromophenol blue) and heating at 95 °C for 5 min. Electrophoresis was carried out in 1× Tris-glycine running buffer (25 mM Tris, 192 mM glycine, 0.1% SDS) at 120 V constant voltage for approximately 60 minutes using a Mini-PROTEAN system (Bio-Rad, USA).

5.2.5.3 Staining and Visualisation

Following electrophoresis, gels were stained with Coomassie Brilliant Blue R-250 for 1 hour and subsequently destained with destaining solution (Bio-Rad) until the background was clear. Protein migration patterns were compared across lanes containing non-mineralised p-tau and mineralised p-tau. A pre-stained molecular weight marker (CHAMELEON® Duo Ladder) was used to confirm protein size and assess potential shifts in apparent molecular mass resulting from mineral deposition.

5.2.5.4 Data Interpretation

Band intensity and migration shifts were analysed by visualisation to quantify any alterations in electrophoretic mobility. Differences in apparent molecular weight between mineralised and control samples were interpreted as evidence of conformational change.

5.3 Results and Discussion

5.3.1 Tissue-level Analysis

A 4-day and a 2-day simulation was studied with a control mouse brain sample. The incubation time was selected according to the results of an optimisation study previously carried by my undergraduate student. Figure 21 presents the BSC-SEM results of the sample changes along with the 4-day simulation experiment. These images illustrate the distribution, morphology, and density of induced mineral deposits, offering valuable insights into the region-specific nature of calcifications in the brain and their potential implications for neurodegeneration.

A wide-angle backscatter SEM image in Figure 21(a) provides an overview of the entire mouse brain, where high-density mineralisation appears as bright regions. Notably, a substantial concentration of calcifications is observed in the dentate gyrus (Figure 21(b)), a hippocampal subregion critical for memory formation and emotional regulation. This localisation is particularly significant as the dentate gyrus is among the earliest areas affected in AD. The accumulation of calcifications in this region suggests increased susceptibility of neuronal populations to mineral deposition, potentially contributing to cognitive impairment. A higher-magnification SEM image shown in Figure 21(b) focuses on calcifications within the dentate gyrus, revealing dense clusters of spherical deposits. This morphology closely resembles mineral formations reported in human AD brain samples, reinforcing the translational relevance of the mouse model. The preference for mineral deposition in neuron-rich areas suggests that metabolic activity and calcium homeostasis disturbances may be key drivers of calcification. Given that calcium dysregulation is a well-documented hallmark of AD, these findings support **hypotheses 2 and 3**.

Figure 21(c) highlights a distinct pattern of calcification in a hippocampal region adjacent to the dentate gyrus. This region exhibits a more diffuse and randomly distributed calcification pattern than the concentrated mineralisation observed in Figure 21(b). Such variability suggests that different hippocampal subregions may exhibit varying susceptibilities to mineral deposition, potentially influenced by differences in neuronal density, metabolic demand, or structural properties. This observation raises intriguing questions regarding the selective vulnerability of neuronal populations in AD and whether specific cell types or microenvironments promote calcification.

A detailed CDD-SEM image captures the microstructure of individual calcifications (Figure 21(d)), revealing well-defined spherical deposits at the cellular level. The structural resemblance between these formations and those found in human AD brains further validates the experimental model. These deposits' clear boundaries and dense composition suggest they could act as physical barriers within neuronal cells, disrupting intracellular processes and impairing normal function. As these calcifications grow, they may exacerbate neurodegeneration by interfering with synaptic signalling, neuronal viability, and overall hippocampal function.

Figure 21(e) is the EDS analysis that provides compositional insights into the calcifications, revealing characteristic peaks for calcium (Ca) and phosphorus (P), and occurrence of oxygen (O). This confirms that the deposits primarily comprise calcium phosphate, a pathological feature frequently associated with neurodegenerative diseases. Calcium phosphate suggests a direct link between neuronal calcium dysregulation and mineral formation. In AD, disruptions in calcium signalling can lead to intracellular calcium overload, which may precipitate as mineral deposits. Over time, these calcifications may perpetuate a detrimental cycle, further impairing neuronal function and accelerating disease progression.

The findings from this r-SBF simulation underscore the strong correlation between neuronal degeneration and mineral deposition in AD pathology. Highly metabolically active Neurons rely heavily on calcium signalling for various intracellular functions. In AD, disruptions in calcium homeostasis may trigger a cascade of pathological events, leading to cellular stress, dysfunction, and ultimately neuronal death. Calcium phosphate micro-calcifications within neurons suggest that these deposits may not merely be by-products of degeneration but active contributors to the disease process.

The spherical shape and dense clustering of these calcifications indicate that neuronal cells may serve as preferential sites for mineral nucleation. Over time, the progressive accumulation of these deposits could interfere with typical neuronal architecture, potentially leading to structural disintegration and cognitive decline. Additionally, the regional variability in calcification patterns, as observed in Figures 21(b) and (c), suggests that specific neuronal populations may be inherently more prone to calcification due to differences in metabolic activity or specific intracellular structure.

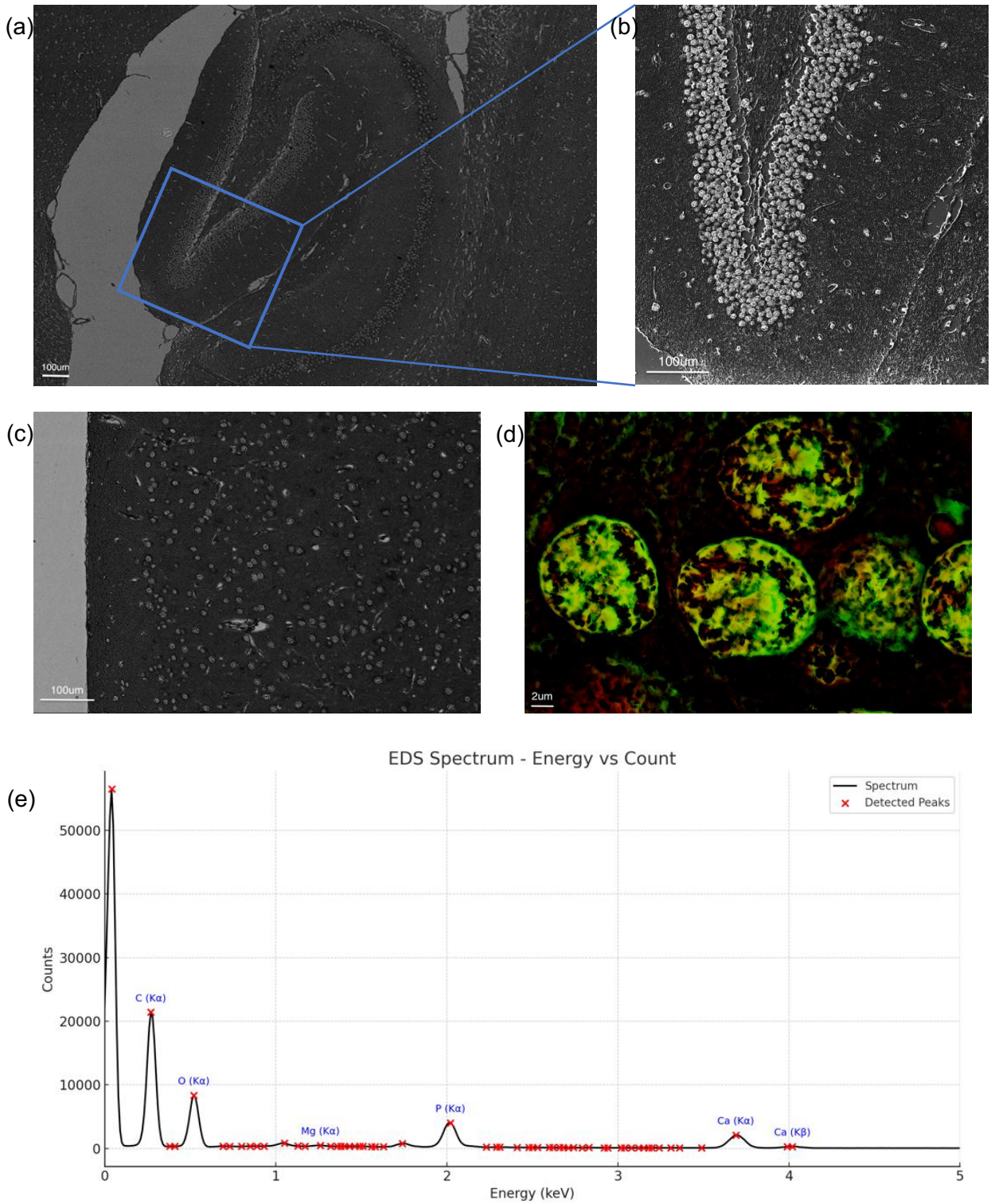

Figure 21. BSE-SEM images of mouse brain samples under a 4-day calcification induction. (a). Large-scale backscatter views clusters of calcifications throughout the entire mouse brain, scale bar = 100 μm; (b). A zoom-in on the dentate gyrus area, scale bar = 100 μm; (c). Large-scale views of the calcification of the other part of the hippocampus tissue, scale bar = 100 μm; (d). A DDC-SEM of spherical calcification, scale bar = 2 μm; (e) EDS of the mineralisation observed.

Figure 22 presents backscattered electron scanning electron microscopy (BSE-SEM) images of mouse brain tissues subjected to simulated body fluid (r-SBF) incubation, illustrating time-dependent mineralisation compared to an untreated control sample. In panel (a), the sample incubated in r-SBF for 4 days displays dense and widespread high-intensity regions, which are characteristic of calcium phosphate mineral deposition (as shown in Figure 21) The bright regions correspond to areas of high atomic number, as revealed by backscattered electron contrast, and their spherical and clustered morphology aligns with previously reported microcalcifications observed in both simulated and pathological brain tissues.

Panel (b) shows a sample subjected to 2 days of r-SBF immersion, displaying fewer and smaller mineral aggregates in comparison to the 4-day sample. These calcified areas are still visible as distinct bright spots, but their lower density and more limited distribution suggest that mineralisation is progressive, with extent and intensity increasing with incubation time. This indicate that longer exposure to mineralising conditions enhances calcium phosphate accumulation in the tissue matrix.

In contrast, panel (c) depicts the untreated control sample, which was not exposed to r-SBF. The image shows a uniform surface with no detectable high-density structures or surface irregularities. The absence of mineral features in this sample confirms that the calcifications observed in panels (a) and (b) are not artifacts of fixation, dehydration, or imaging, but are directly attributable to the simulation model.

These images demonstrate the efficacy of the r-SBF protocol in inducing controlled mineralisation in brain tissue and highlight the potential of this model to mimic early-stage pathological calcification. The observed progression between 2-day and 4-day incubations provides visual and structural evidence of time-dependent mineral growth, allowing for a better understanding of how microcalcifications might form and evolve in vivo, particularly in the context of neurodegenerative diseases such as Alzheimer's disease. This approach lays the groundwork for further investigation into the molecular triggers and cellular environments that promote mineral deposition in the brain and may help to identify early-stage biomarkers or therapeutic targets related to pathological mineralisation. The presence of mineral deposits within neuronal compartments suggested a potential interaction between tau protein aggregates—particularly in their phosphorylated forms—and the calcification process.

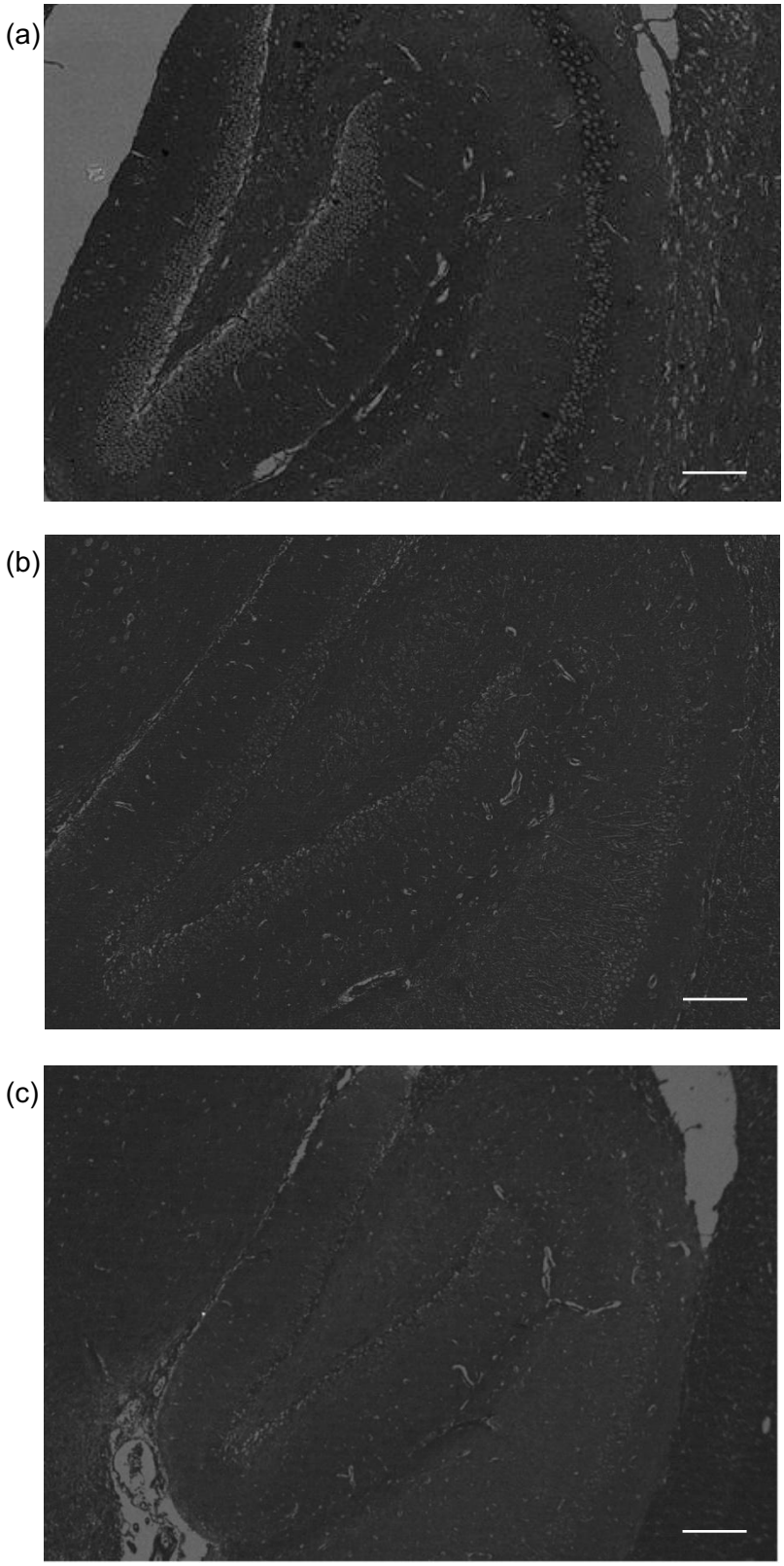

Figure 22. BSE-SEM images of mouse brain samples following simulated mineralisation, with all three mouse samples showing a similar mineralisation trend under different time simulations. (a) Sample after 4-day r-SBF incubation; scale bar =

200 µm. (b) Sample after 2-day r-SBF incubation; scale bar = 200 µm. (c) Control mouse brain sample without simulation; scale bar = 200 µm.

5.3.2 Protein-level Analysis

Simulation of variant tau proteins was conducted following the tissue-level mineralisation experiments, prompted by the observation of intracellular calcification described in Chapter 5.3.1.

Tau proteins exhibited structural variability following incubation in simulated body fluid (r-SBF). Figure 23 displays TEM images captured after 24 hours of simulation, highlighting a range of morphological characteristics across different tau variants. In all samples, small, high-density particles were consistently detected, indicating the potential for early-stage protein-associated mineralisation or crystallisation.

In the Tau383 sample (Figure 23(a)), scattered, square-shaped, low-contrast particles are observed across multiple regions of the grid, highlighted by the red boxes. These features appear faint and are frequently isolated, lacking close association with surrounding proteinaceous structures. The apparent spatial separation between these particles and adjacent protein deposits suggests a lack of consistent co-localisation. Additionally, the overall field appears relatively sparse, with a low density of aggregated protein material, indicating limited interaction or mineral accumulation within this specific tau variant under the given simulation conditions.

In the pTau441 sample (Figure 23(b)), a dense, dark region is present near the centre of the image, displaying an irregular shape and sharply defined edges. The particle occupies a relatively large area and shows higher electron density than its surroundings. The area around this central structure immediately contains a more finely textured, granular matrix. Toward the periphery, elongated, thread-like structures are faintly visible. These vary in length and contrast, appearing as loosely aligned or partially extended filaments. The differences in morphology within this image suggest the presence of compact and less structured material across the field.

The r-SBF mineral deposition process is particularly relevant in neurodegeneration, where abnormal protein deposits have been associated with neuronal calcification. In the TEM image, specific dark, well-defined regions may indicate mineralised pTau aggregates, suggesting that the protein has undergone structural reorganisation due to its interaction with r-SBF components. This raises the

possibility that pTau aggregation may be a biochemical process that involves physicochemical alterations influenced by its surrounding environment.

In the pTau199 sample (Figure 23(c)), a dark, dense structure with a diameter of approximately 0.5 μm was observed. This structure appears bulkier and more crystalline than those found in theTau383 and pTau441after24 hours of r-SBF simulation. The relatively straightforward, large, and well-defined morphology suggests a higher degree of structural organisation or aggregation, potentially indicating protein crystallisation or mineral deposition.

Given the r-SBF incubation environment, which supplies calcium (Ca^{2+}) and phosphate (PO_4^{3-}) ions, the presence of a high-density, crystallised structure in the pTau199 sample suggests a stronger interaction with these ionic components compared to other proteins. This observation may indicate that specific phosphorylation sites on pTau199 increase its affinity for ion-induced aggregation or mineralisation, potentially contributing to a unique structural outcome. However, no diffraction patterns characteristic of crystalline structures was detected, likely due to the limited quantity of deposited mineral or the absence of fully developed crystalline phases under the experimental conditions.

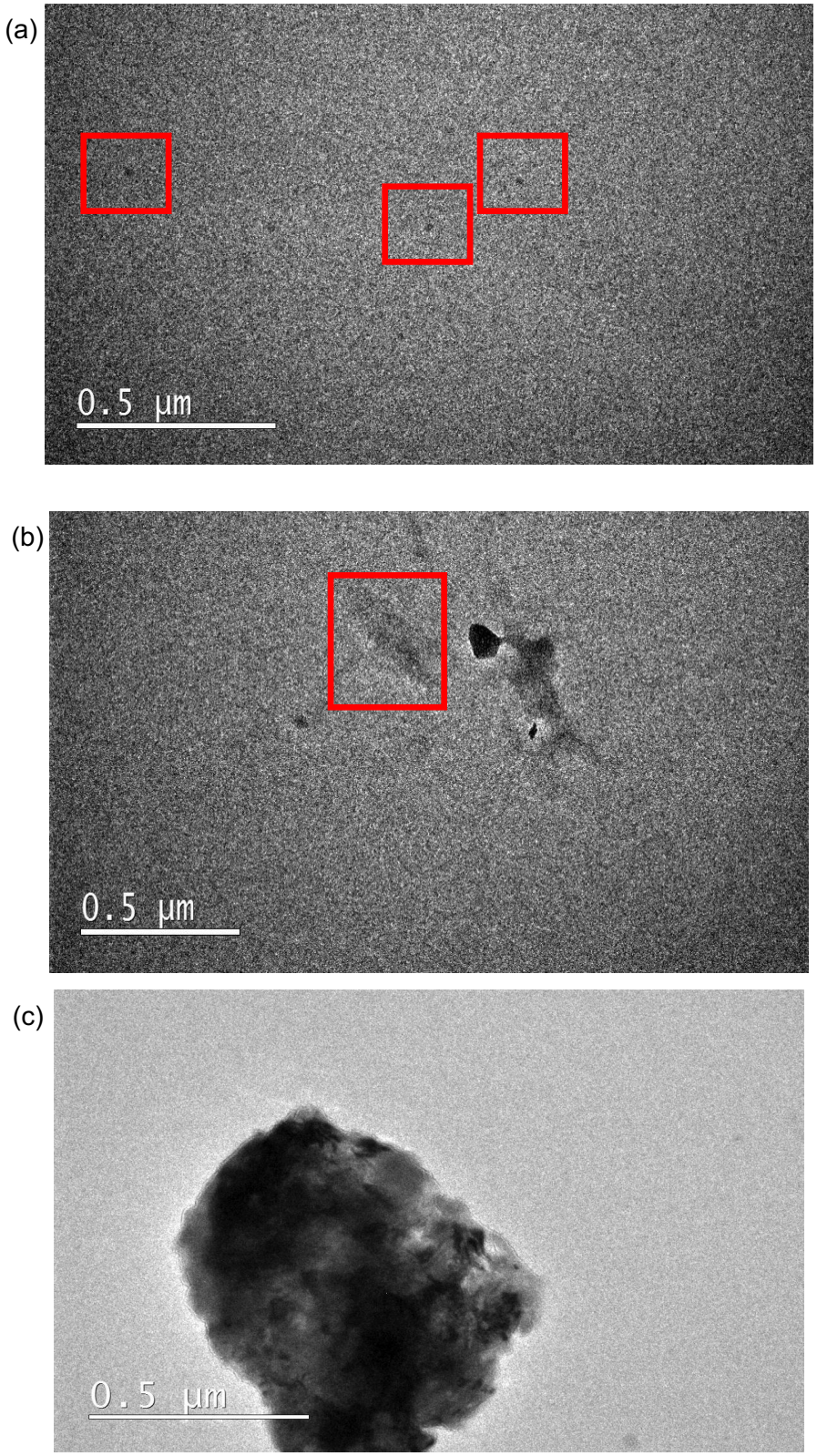

Figure 23. r-SBF simulation on different proteins under 24 hours simulations at 37 degrees Celsius, scale bar = 0.5 µm. (a) Tau383 under a 24-hour simulation, red boxes highlighted the high-density particles. (b) pTau441 under a 24-hour simulation, elongated structure highlighted in red box. (c) pTau199 under a 24-hour simulation.

Figure 24 presents the structures formed after a 48-hour r-SBF simulation to investigate the protein crystallisation process further. Compared to the 24-hour incubation, all three proteins exhibited an overall increase in high-contrast particles, suggesting a progression in aggregation or mineral deposition over time.

In the Tau383 sample (Figure 24(a)), the square-like crystalline formations previously observed after the 24-hour simulation evolved into more elongated, rectangular structures with extended incubation time. This morphological shift suggests a progressive ordering or growth of the mineralised material, potentially driven by continued interaction between the protein and the ionic components of the r-SBF solution. These rectangular features bear a strong resemblance to those seen in Figure 23(a), indicating that they may share a common nucleation mechanism or crystallisation pathway. The consistency in shape and appearance across different time points further supports the notion that Tau383 may promote a specific type of mineral organisation, possibly influenced by its structural conformation or phosphorylation state under simulation conditions.

In the pTau441 sample (Figure 24(b)), a markedly higher density of dark, high-contrast structures was observed, exhibiting greater variability in both location and size. This represents a substantial progression in crystallisation or aggregation compared to the 24-hour simulation. In contrast to the smaller and more dispersed particles seen at the earlier time point, the presence of larger and more densely packed structures suggests that prolonged incubation promotes continued mineral growth and organisation. This trend implies that extended exposure to the simulated body fluid enhances the potential for protein aggregation and/or calcium phosphate deposition, highlighting the time-dependent nature of tau-associated mineralisation processes.

The pTau199 sample (Figure 24c) displayed a distinct pattern compared to the other protein variants. In contrast to the relatively well-defined and uniform structures observed in pTau441, the mineral formations in pTau199 appeared significantly more irregular and heterogeneous, with marked variations in density and distribution across the sample block (highlighted in the large red box). This spatial and morphological inconsistency suggests that pTau199 may interact differently with the simulated body fluid (r-SBF) environment, likely influenced by its unique structural conformation or phosphorylation-dependent aggregation behaviour. Notably, small square-like crystalline features, similar to those previously identified in the Tau383

samples, were also present in pTau199 (highlighted in the small red box). The recurrence of these crystallisation patterns across different tau isoforms points to a potentially shared mineralisation pathway, although the morphology, extent, and organisation of these structures differ depending on the specific tau variant. These observations underscore the importance of isoform-specific properties in directing the nature and progression of mineral formation, suggesting that even subtle differences in tau structure or phosphorylation state can significantly affect calcium phosphate nucleation and growth under physiologically simulated conditions.

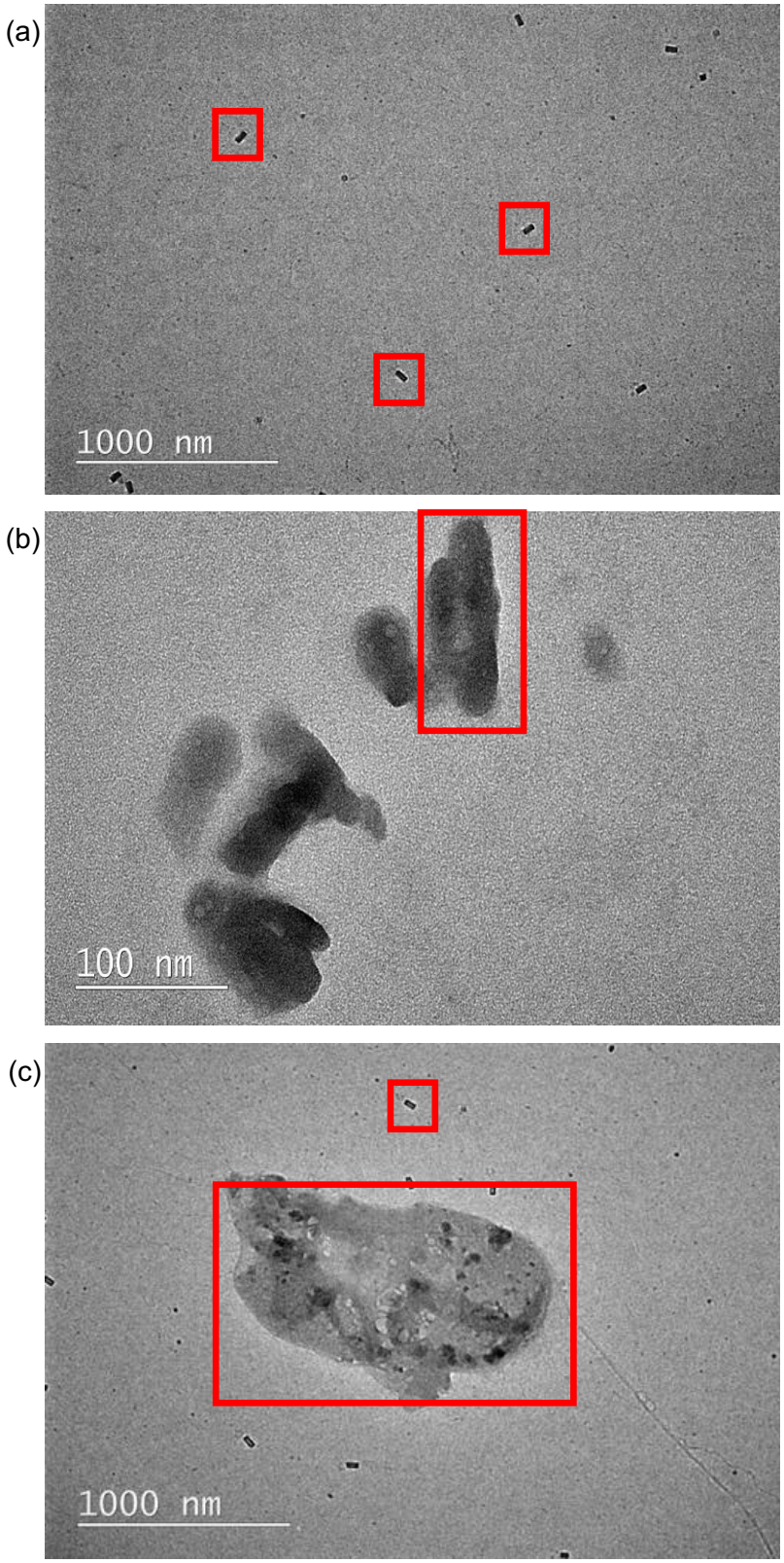

Figure 24. r-SBF simulation on different proteins under 48 hours simulations at 37 degrees Celsius, red boxes highlighted the high-density particles (a) Tau383 under a 48-hour simulation, scale bar = 1000nm. (b) pTau441 under a 48-hour simulation, scale bar = 1 μm. (c) pTau199 under a 48-hour simulation, scale bar = 1000nm.

The differences between the 24-hour (Figure 23) and 48-hour (Figure 24) simulations highlight the time-dependent nature of protein crystallisation and aggregation under r-SBF conditions. The distinct structural characteristics observed in each protein variant imply differential interactions with the surrounding ions, potentially influenced by their phosphorylation state and structural properties. These findings emphasise the importance of time and protein composition in determining the extent and morphology measuring formations surrounding of crystallisation or mineral deposition, which could have implications for understanding protein aggregation mechanisms in pathological conditions such as AD.

The microstructural analysis of the 48-hour mineralised phosphorylated tau (pTau) sample was conducted using high-resolution transmission electron microscopy (HRTEM), selected-area electron diffraction (SAED) and Fast Fourier Transform (FFT) processing, as shown in Figure 25.

Figure 25a shows a lattice resolved HRTEM image revealing nanoscale crystalline regions within the tau matrix. Lattice fringes with periodic spacing between 0.25 nm and 0.30 nm are visible, suggesting the presence of calcium phosphate nanocrystals. These crystalline domains appear embedded in a partially amorphous background, consistent with a heterogeneous mineralisation process where the tau protein network provides nucleation sites for inorganic crystal growth. The observed lattice periodicity corresponds well to typical interplanar spacings of hydroxyapatite (HAp), supporting the presence of a HAp-like mineral phase.

Figure 25b presents the SAED pattern collected from the same specimen area. The pattern displays distinct, symmetrically distributed diffraction spots, confirming the crystalline nature of the mineral phase. The calculated d-spacings (≈ 0.26 nm, 0.13 nm, 0.09 nm) correspond to the (211)/(112)/(300) and higher-order planes of hexagonal hydroxyapatite. The sharpness and regularity of these reflections indicate a degree of crystallographic order within the nanocrystalline calcium phosphate regions. Together with the HRTEM observations, this demonstrates that tau/pTau complexes can support oriented mineral nucleation and growth.

Figure 25c shows the FFT pattern extracted from a high-resolution area of the same crystal. The cross-shaped arrangement of bright frequency spots corresponds to periodic lattice order along two orthogonal axes, confirming the presence of a well-ordered crystalline substructure. The reciprocal-space spacing yields an estimated real-space d-spacing near 0.30 nm, consistent with the (211)/(300) reflections

identified in the SAED pattern. The congruence between the FFT and SAED results validates the presence of hydroxyapatite-like calcium phosphate nanocrystals embedded within the tau and phosphorylated tau assemblies.

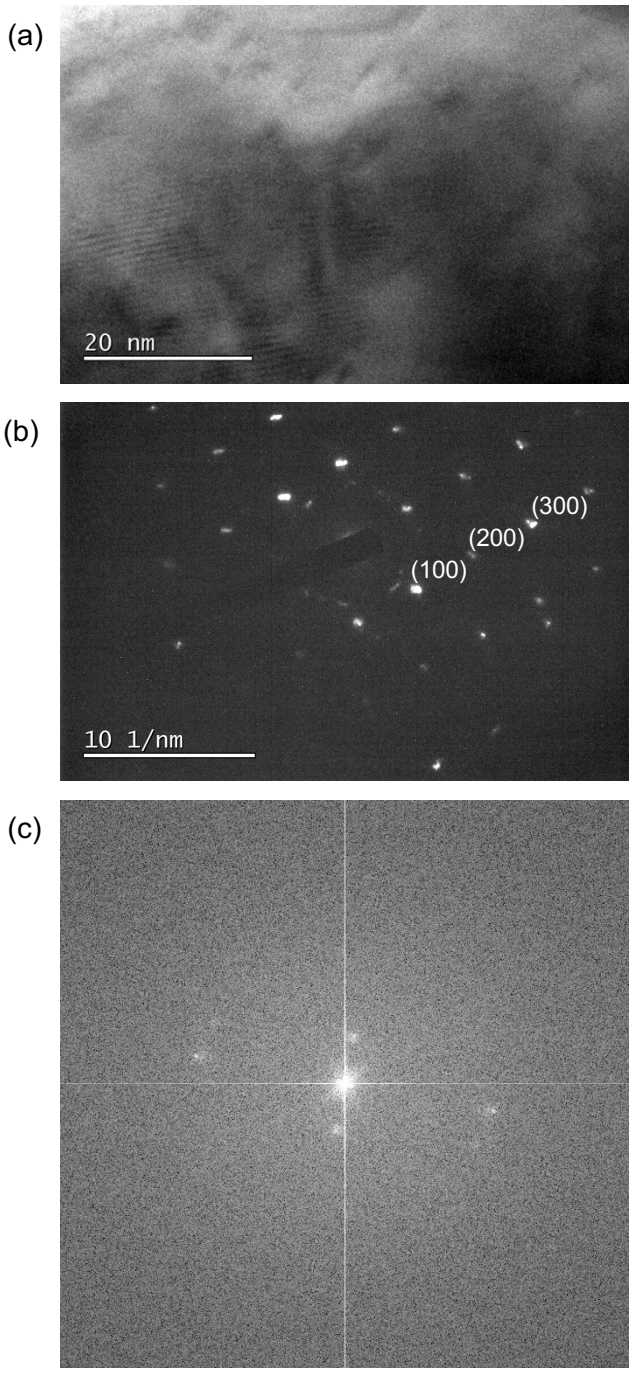

Figure 25. Microstructural characterisation of mineralised proteins using TEM, SAED and FFT analysis. (a) High-resolution TEM (HRTEM) image showing nanoscale lattice fringes within the mineralised tau matrix, indicating crystalline domains embedded in an amorphous background. (b) Selected Area Electron Diffraction (SAED) pattern acquired from the same region, displaying discrete diffraction spots consistent with hexagonal hydroxyapatite (HAp) reflections. (c) Fast Fourier

Transform (FFT) of a lattice-resolved area confirming periodic order and lattice symmetry corresponding to HAp (211)/(300) planes.

Figure 26 presents the SDS-PAGE analysis of phosphorylated tau (pTau441) and mineralised pTau441 samples. Commercial pTau441 was selected as the control due to its high purity, with only minor faint bands indicating trace fragments. Lane 1 shows a predominant monomeric band with an apparent molecular weight of approximately 64 kDa, consistent with monomeric pTau441. Lanes 2 and 3 correspond to the pellet and supernatant fractions, respectively, obtained after 48 hours of mineralisation in simulated body fluid (r-SBF). Both lanes display a similar pattern, featuring pronounced high-molecular-weight (HMW) smears extending from 70 kDa to 160 kDa with reduced intensity at the monomer position. This pattern suggests the formation of aggregated protein species or protein–mineral complexes exhibiting poor electrophoretic mobility. In addition, the presence of low-molecular-weight fragments (approximately 12–25 kDa) indicates proteolytic truncation of tau, likely representing N-terminal fragments (15–25 kDa) and C-terminal fragments (12-18 kDa) generated during or after the mineralisation process.

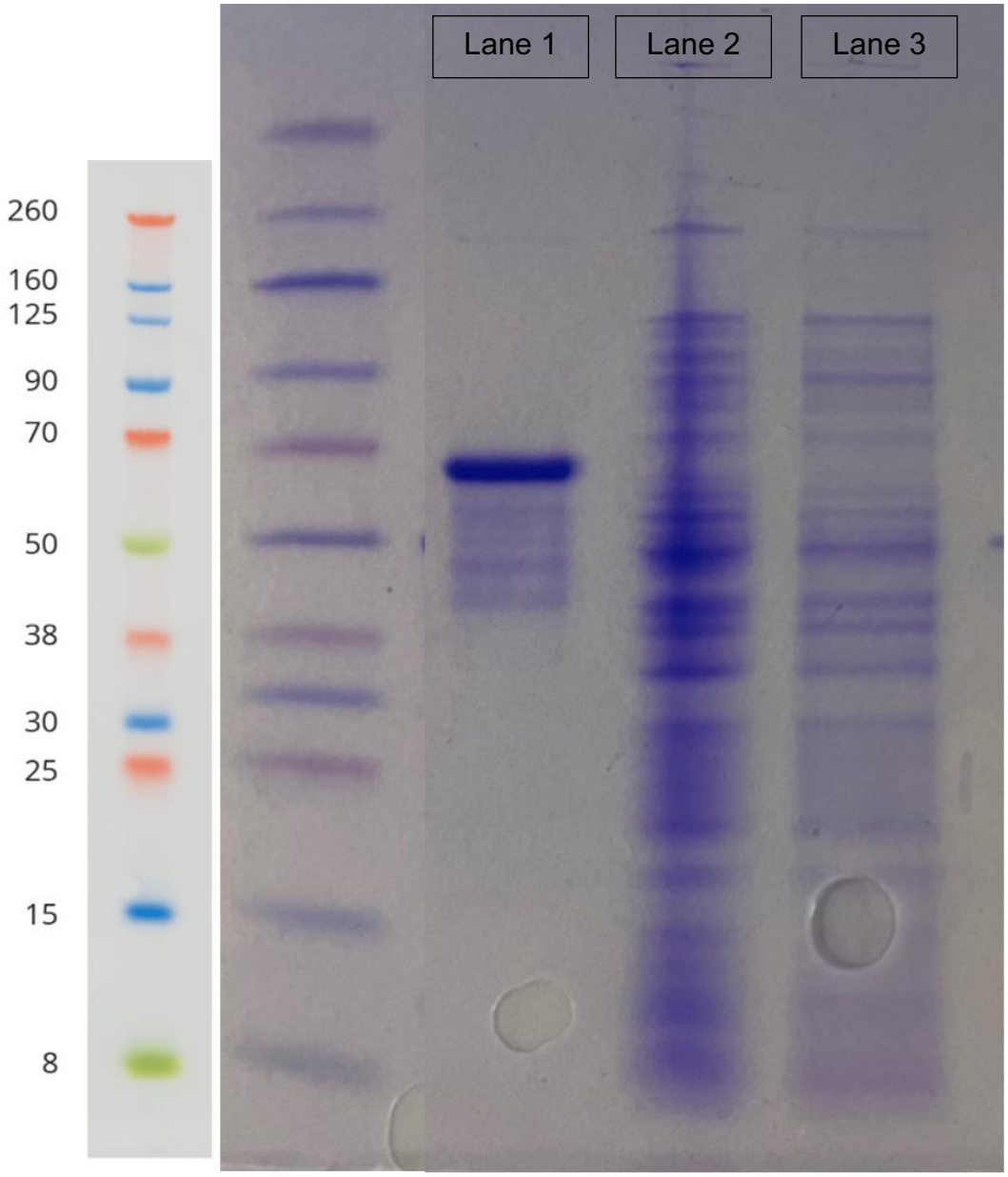

Figure 26. SDS-PAGE gel showing protein separation under mineralisation using the Mini-PROTEAN system (Bio-Rad, USA). The molecular weight marker (left lane) indicates reference bands ranging from 8 to 260 kDa. Lane 1 shows a distinct band at approximately 64 kDa, corresponding to the purified recombinant ptau441 protein. Lanes 2 and 3 show the mineralised ptau441 samples, which exhibit multiple bands of varying molecular weight.

Figure 27 presents the structural outcomes observed across all 48-hour r-SBF simulation models, revealing a diverse array of high-density accumulations and fibril-like formations. The considerable morphological heterogeneity among these structures' points to two primary interpretations. First, the observed features may

represent progressive aggregation of variant tau proteins under simulated physiological conditions, where prolonged exposure to calcium and phosphate ions promotes protein-mineral interactions and mineralisation along protein scaffolds.

Second, the appearance of some filamentous or clustered high-density regions raises the possibility of bacterial contamination or the presence of biomimetic crystallisation phenomena that mimic microbial morphology. Certain crystallised salt or mineral aggregates, particularly under high ionic strength conditions and extended incubation, can form structures resembling microbial colonies or biofilms. Additionally, unintentional microbial growth introduced during sample handling or incubation could produce dense, irregular deposits that differ from pure protein-mineral complexes.

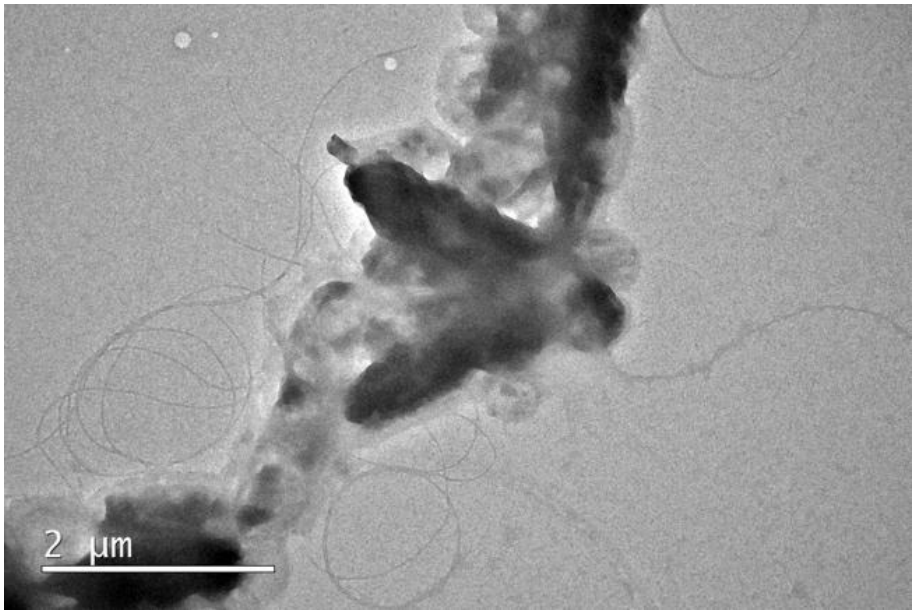

Figure 27. r-SBF simulation on different proteins under 48 hours simulations at 37 degrees Celsius. Bacterial-like structures observed in all protein samples after the 48-hour simulation, scale bar = 2 µm.

5.4 Conclusion and Future Work

The results from the simulation model support **Hypothesis 2: AD-like mineralisation can form in neuronal tissues under conditions that mimic the body's internal fluid environment.** A revised simulated body fluid (r-SBF) tissue-level simulation results demonstrated that prolonged exposure promotes the formation of calcium phosphate deposits. After 4 days simulation, mouse brain tissue sections exhibited dense, neuron-associated calcifications, including spherical and fibrillar structures consistent with those identified in AD-affected regions such as the basal ganglia and hippocampus. These mineralised features were preferentially localised to dentate gyrus areas, and appeared to be intracellular, suggesting that neuronal components may serve as nucleation sites for calcification. This finding aligns with the histological observations in post-mortem AD tissue and supports the notion that neurons may play an active role in pathological mineral deposition.

Moreover, time-course experiments using 2-day and 4-day incubations revealed a clear temporal pattern in mineral accumulation, highlighting the time-dependent nature of calcium phosphate mineralisation. This progression suggests that chronic ionic imbalance or prolonged physiological stress in the brain could contribute to ongoing calcification processes, potentially exacerbating neurodegeneration over time.

However, efforts to test whether the mineralisation environment selectively degrades phosphorylated proteins while preserving tau proteins—as proposed in **Hypothesis 3**—yielded partial conclusive results. High-density mineral deposits were observed across all protein variants examined (Tau383, pTau199, and pTau441). However, based on the current structural and compositional analyses at the 100 nm scale, no definitive protein-specific calcification could be confidently attributed to direct interactions between tau or phosphorylated tau (pTau) and the mineral phase. The absence of characteristic mineral–protein binding signatures indicates that further molecular-level evidence will be required to validate the proposed mechanism of tau-mediated nucleation.

At higher resolution (20 nm scale), diffraction and FFT analyses consistently revealed crystalline features corresponding to hydroxyapatite (HAp) across all tau variants, with no distinguishable differences between isoforms. These findings suggest that HAp formation is possible under r-SBF simulation conditions; however,

extended mineralisation experiments were discontinued due to the emergence of bacterial-like structures, which compromised sample integrity.

Subsequent SDS-PAGE analysis of pTau441 and mineralised pTau441 demonstrated the presence of high-molecular-weight species and multiple low-molecular-weight fragments, indicative of aggregation, potential protein–mineral complex formation, and proteolytic truncation during the mineralisation process. Collectively, these results provide preliminary evidence for mineral association with tau proteins but highlight the need for additional, higher-resolution biochemical and biophysical analyses to establish definitive mechanistic insight.

Future work should focus on enhancing the resolution and specificity of protein-level mineralisation analysis, including the application of cryo-electron microscopy, immunogold labelling, or correlative imaging techniques to better localise mineral-protein interactions. Additionally, protein integrity and phosphorylation status should be confirmed post-incubation using Western blotting or mass spectrometry, to assess whether selective degradation or preservation occurs under mineralising conditions. Improving sample purity, refining incubation protocols, and applying real-time mineralisation tracking may further clarify the relationship between tau proteins and pathological calcification in Alzheimer's disease.

Chapter 6: Colocalisation study of neuron, pTau and calcification

6.1 Introduction

Intracellular calcifications were first identified in Chapter 4 and further replicated under physiologically relevant conditions using the revised simulated body fluid (r-SBF) model in Chapter 5. Building on our previous findings [122] and incorporating evidence from both post-mortem Alzheimer's disease (AD) brain tissue and tissue-level simulation models, a clear positive correlation has emerged between calcification extent and pathological disease progression, particularly in the basal ganglia, hippocampus, and temporal lobe. These regions are known to be densely populated with neurons and heavily implicated in AD-related cognitive decline.

Importantly, microcalcifications appear to accumulate preferentially within neuron-rich substructures, such as the dentate gyrus of the hippocampus, suggesting that the neuronal microenvironment may play a critical role in facilitating or attracting mineral deposition. This spatial patterning raises the possibility that calcifications are not merely by-products of degeneration but may actively contribute to neuronal dysfunction. Based on these observations, this chapter focuses on investigating the colocalisation of microcalcifications with neuronal cells and key disease-associated markers, particularly phosphorylated tau (pTau). I hypothesise (**Hypothesis 4**) that microcalcifications in AD brains are spatially associated with neurons, and that this colocalisation reflects underlying pathological mechanisms contributing to Alzheimer's disease progression. To test this hypothesis, immunofluorescence staining and spatial colocalisation analysis were performed to identify whether calcified deposits consistently overlap with neuronal and pTau markers. Particular attention was given to the timing and distribution of characteristic features, aiming to determine the onset point of such colocalisation during different stages of the disease (**Hypothesis 5: intracellular calcification promotes pTau aggregation**).

6.2 Materials and methods

6.2.1 Samples

For this study, a total of 15 post-mortem human brain tissue samples from the basal ganglia, hippocampus and temporal lobe were selected based on prior observations of intracellular calcification. To ensure a representative distribution across disease progression, five samples were randomly selected from each of the three clinical Braak stage groups: early stage (Braak I–II), intermediate stage (Braak III–IV), and late stage (Braak V–VI). This stratified sampling approach enabled a comparative analysis of calcification-related colocalization patterns across the continuum of Alzheimer's disease pathology.

From each of the 15 samples of each region, five independent regions of interest were analysed, resulting in a total of 75 data points of each brain region (n=25 for each clinical Braak stage group). These data point regions were selected to maintain consistency in anatomical location and imaging quality, thereby enhancing the reliability of statistical comparisons. This sample size and structure were designed to balance sufficient statistical power with practical constraints such as tissue availability and staining throughput, while also capturing stage-dependent trends in mineralisation and marker colocalisation.

6.2.2 Confocal microscopy

For the immunohistochemical analysis, two high-resolution confocal scanning laser microscopes were employed: the Zeiss LSM 980 with Airyscan detector and the Zeiss LSM 800, both located in the Biosciences Department at University College London (UCL). These instruments were selected for their high sensitivity, spectral flexibility, and superior resolution, enabling accurate visualisation of multiple fluorescent markers within complex brain tissue sections.

Four fluorescent detection channels were configured to visualise specific targets based on the antibody staining panel. DAPI was used for nuclear and DNA staining, serving as a general counterstain to delineate cellular architecture. Alexa Fluor 488 was used to label neuronal cells, providing information on the spatial distribution of neurons. Alexa Fluor 555was employed to detect phosphorylated tau (pTau), a hallmark of Alzheimer's disease pathology. Finally, Alexa Fluor 680 was used in conjunction with the OsteoSense dye to visualise calcium-rich mineral deposits, allowing for the identification of microcalcifications within the tissue.

These fluorescent channels were selected to minimise spectral overlap and ensure reliable colocalisation analysis. The choice of fluorophores and corresponding antibodies is detailed in Chapter 3.1.3, where the full immunostaining protocol and antibody specifications are outlined.

6.2.3 Statistical analysis

The overlap rates between calcification and pTau (CaP), and between calcification and neuronal cells (CaNeu), were calculated using the following formulas:

$$CaP\ Overlap\ rate = (Ca\ channel\ AND\ pTau\ channel / Ca\ channel) * 100\%$$

$$CaNeu\ Overlap\ rate = (Ca\ channel\ AND\ Neu\ channel / Ca\ channel) * 100\%$$

These formulas quantify the percentage of calcification signals that spatially coincide with either pTau or NeuN signals, thereby providing a measure of colocalisation between mineralisation and disease-relevant cellular markers.

All statistical analyses were conducted using GraphPad Prism 10 software. For the assessment of co-occurrence between calcification and cellular markers, a Mann–Whitney U test (two-tailed, unpaired) was employed with a significance threshold of $p < 0.05$. This non-parametric test was chosen because the dataset did not meet the assumptions of normality, as verified through distribution checks. Unlike parametric tests, the Mann–Whitney U test does not require normally distributed data and is thus appropriate for small sample sizes or skewed distributions, such as those obtained in this study. Further information regarding the statistical procedures, including normality testing and software settings, is provided in Chapter 3.2.

Data visualisation was carried out using box plots, where the box represents the interquartile range (IQR)—spanning from the first quartile (Q1) to the third quartile (Q3)—with a line indicating the median. Whiskers represent the minimum and maximum values, excluding outliers unless otherwise stated. This method enables clear comparison of group distributions and highlights differences in central tendency and data spread.

6.3 Results and discussion

6.3.1 Immunochemistry histology analysis of neuronal calcification

Immunofluorescence staining was employed to verify that the calcified, neuron-like structures observed in tissue sections (as described in Chapter 4.3.1) were indeed neuronal cells. Figure 28 demonstrates the spatial colocalisation between calcification and neuronal markers, indicating that the mineral deposits in Alzheimer's disease (AD) samples exhibit a consistent pattern of accumulation within or closely associated with neurons. This finding provides a foundational basis for **Hypothesis 4**, **which proposes that the colocalisation of microcalcification with neuronal cells increases progressively with advancing Braak stages**.

The three-channel overlapped immunofluorescence image reveals a distinct cell band in the same anatomical region where a calcification band was previously identified in Chapter 4.3.1. To further clarify the spatial relationships among the stained targets, split-channel images are presented in Figures 28(b), (c), and (d). DAPI staining, shown in Figure 28(b), serves as a nuclear counterstain, highlighting the overall cellular architecture and positioning. The neurons (Figure 28(c)) and calcification (Figure 28(d)) channels demonstrate a strong degree of spatial overlap. This colocalisation indicates a close spatial relationship between neuronal populations and mineral deposits, reinforcing the observation that calcification occurs preferentially in neuron-rich zones, as mentioned in Chapter 4.3.1 and Chapter 5.3.1. The observed fluorescence signal overlap implies that neurons may play a significant role in the mineralisation process. On one hand, it is possible that neuronal cells actively participate in the formation of calcifications, potentially triggered by specific intracellular structures or proteins inside the neurons. On the other hand, these neurons, especially those rendered vulnerable by the disease, may instead serve as passive recipients of calcium phosphate accumulation. In this scenario, impaired calcium regulation and progressive cellular degeneration could create a permissive environment for mineral deposition within or around neuronal structures.

Overall, this co-distribution further supports that microcalcification in Alzheimer's disease is not random but is instead intimately linked to neuronal structure and pathology, possibly serving as an early or progressive marker of disease-related neuronal dysfunction.

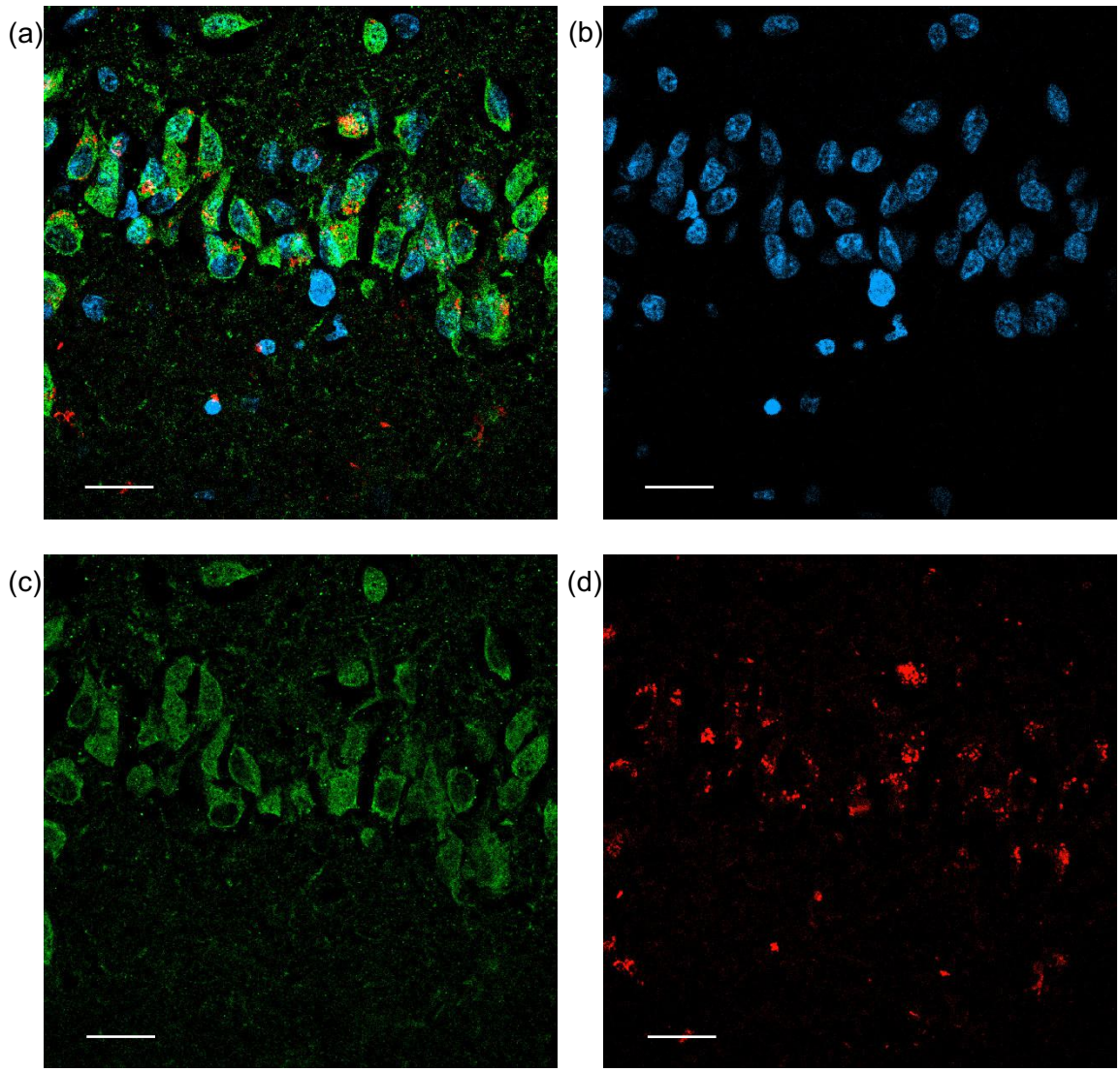

Figure 28. Multiplexing basal ganglia confocal image of a BRAAK VI patient (P07/11) at the calcification band region, indicating nuclei, neurons and microcalcification. At 20x magnification, with the scale bar = 50 μm. (a) An overall view of the 3-channel image. (b) The DAPI channel represents the appearance of the nucleus (blue channel). (c)The neu channel represents the appearance of Neurons (green channel). (d) Calcification channel represents the appearance of calcium deposition (red channel).

A high-resolution immunofluorescence image, presented in Figure 27, provides detailed visualisation of calcification within a single neuron, highlighted with a white box. The DAPI stain, shown in Figure 29(b), was used to localise the nuclei and confirm cellular identity. The neuronal marker NeuN (Figure 29(c)) and the calcification probe signal (Figure 29(d)) exhibit a high degree of spatial overlap, suggesting a close association between neuronal structures and calcified deposits.

The merged three-channel image in Figure 29(a) clearly illustrates this colocalisation, with a prominent calcification signal aligned along the axon-like projection of the neuron. Notably, the neuronal cell body demonstrates only limited calcification, primarily localised within the cytoplasmic region, with no significant accumulation observed in the nuclear area.

This observation suggests a more refined pattern of intracellular calcification, potentially involving early axonal pathology or region-specific vulnerability within neuronal compartments. The calcification along axons may reflect disrupted calcium trafficking or degeneration of cytoskeletal structures, both of which are hallmarks of neuronal damage in AD. This specific localisation prompted a shift in focus—from the general association of calcification with neuronal cells to a more targeted investigation of its relationship with intracellular phosphorylated tau (pTau), a key pathological hallmark of Alzheimer's disease.

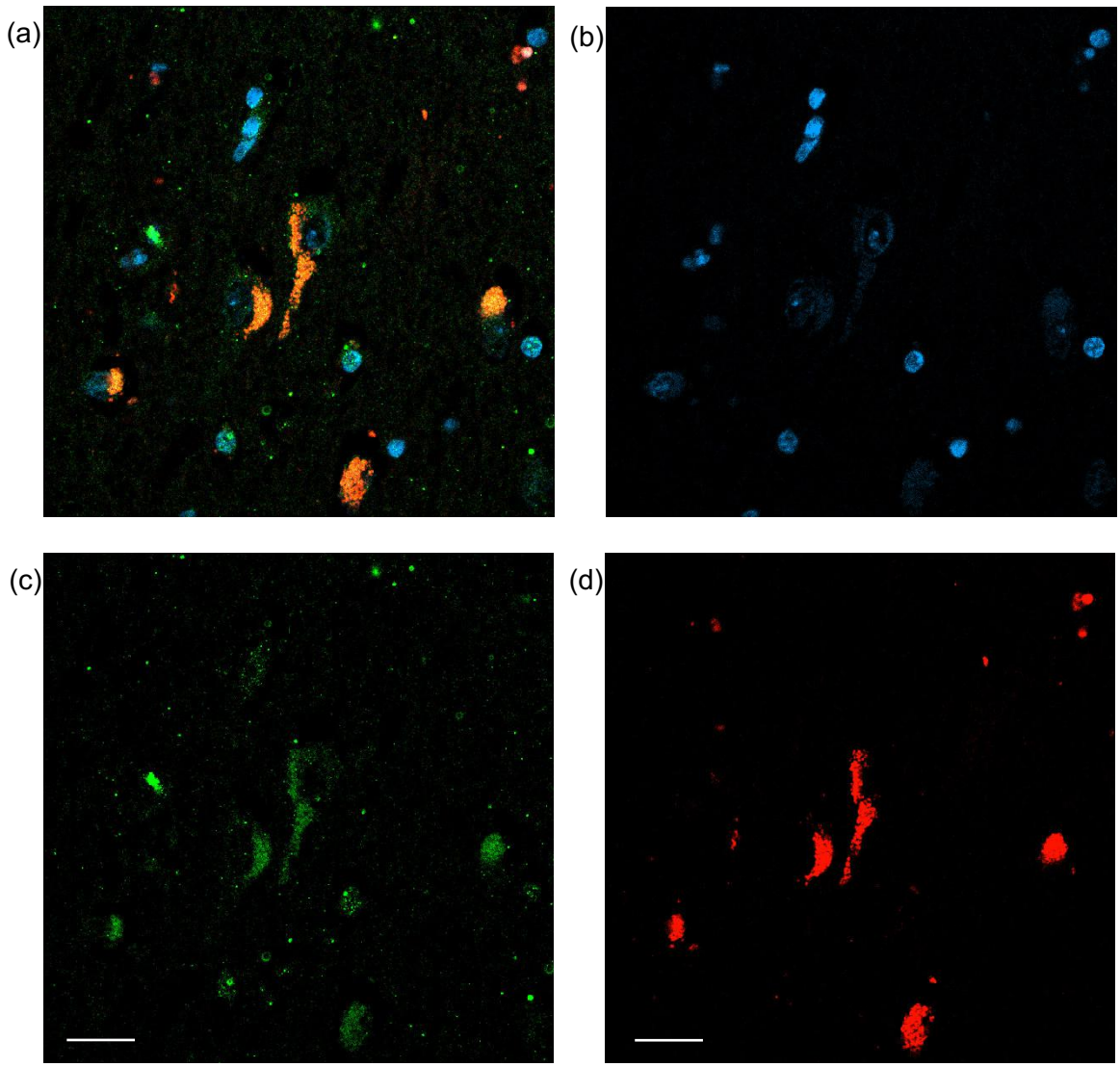

Figure 29. Multiplexing basal ganglia confocal image of a BRAAK VI patient (P07/11) at the calcification band region, indicating nuclei, neurons and microcalcification. At 40x magnification, with the scale bar = 10 µm. (a) An overall view of the 3-channel image. (b) The DAPI channel represents the appearance of the nucleus (blue channel). (c)The neu channel represents the appearance of Neurons (green channel). (d) Calcification channel represents the appearance of calcium deposition (red channel).

A four-channel immunofluorescence analysis was performed on temporal lobe samples representing early, intermediate, and late stages of Alzheimer's disease, as illustrated in Figure 30 (early stage), Figure 31 (intermediate stage), and Figure 32 (late stage). DAPI staining, shown in Figures 30(a), 31(a), and 32(a), outlines the nuclei of cells, providing critical structural reference points for assessing the spatial localisation of neuronal markers and calcification.

Figures (c) through (e) in each case display the individual fluorescence channels: phosphorylated tau (pTau) is shown in orange, NeuN (neuronal marker) in green, and calcifications in red. This colour-coded representation allows for precise visualisation of colocalisation patterns across different disease stages, supporting the analysis of spatial relationships between pathological markers and mineral deposits.

In the early-stage sample, which had not yet been clinically diagnosed as AD and exhibited minimal or no symptoms, calcifications were already detectable, albeit at relatively low levels. Notably, these mineral deposits showed complete spatial colocalisation with both neuronal markers and phosphorylated tau (pTau), as highlighted by the white boxes in Figure 30. This observation stated a strong correlation between pTau and intracellular calcification, and it is consistent with the scanning electron microscopy (SEM) findings presented in Chapter 4.3.1, which demonstrated that brain calcification can occur at the early Braak stages, before the onset of noticeable symptoms or formal diagnosis. The early presence and specific localisation of calcification suggest that microcalcification may represent one of the earliest detectable pathological changes in Alzheimer's disease, with potential value as an early-stage biomarker.

The yellow boxes in Figure 30 highlight a potential early event in axonal calcification. In this region, no calcification is observed within the neuronal cell body; however, a distinct calcified deposit is detected adjacent to the nucleus. This deposit colocalises with both the pTau and neuronal markers, suggesting that mineralisation may begin in axonal or perinuclear regions before extending to the cell body. This pattern implies that axonal segments, particularly those under early tau-related stress may serve as initial sites of pathological calcification, offering further evidence of the spatially specific and progressive nature of mineral deposition in Alzheimer's disease.

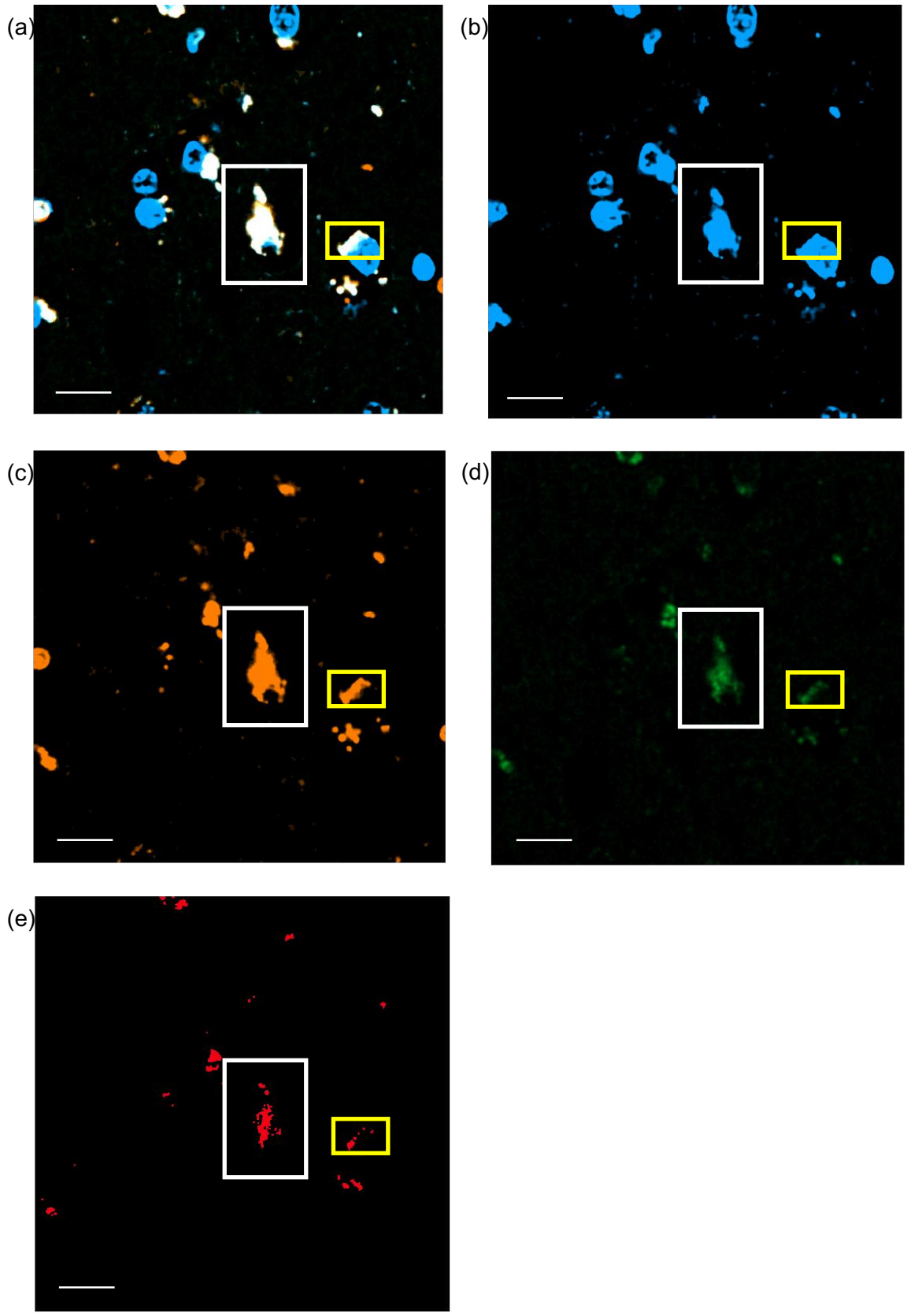

Figure 30. Multiplexing temporal lobe confocal images of DAPI, calcification, pTau, and neurons at early Braak stages (P75/08) at 40x magnification, with the scale bar = 20um. (a) Overlapped image. (b) Blue-DAPI. (c) Orange-pTau. (d) Green-Neu. (e) Red-Calcification.

In the intermediate-stage sample, shown in Figure 31, the patient had not yet received a clinical diagnosis of Alzheimer's disease but exhibited mild cognitive symptoms indicative of early pathological changes. The staining pattern closely resembles that of the early-stage sample described in Figure 30, with calcifications continuing to show a high degree of colocalisation with both phosphorylated tau (pTau) and neuronal (NeuN) markers.

Notably, calcified deposits were frequently observed around the nuclear periphery, rather than within the nucleus itself. These peripheral calcifications, one of which is highlighted in the white boxes, suggest a continued pattern of early-stage mineralisation in areas vulnerable to neurodegeneration. The consistent presence of pTau and neuronal colocalisation across stages reinforces **hypothesis 4** that tau pathology and neuronal integrity are tightly linked to the spatial development of microcalcification.

This persistence of nuclear-adjacent calcification, even in the absence of formal AD diagnosis, may indicate a pathological transition zone where early neurodegenerative mechanisms, such as tau aggregation and ionic imbalance, begin to promote localised mineral deposition. As such, these findings support the view that calcification is not merely a consequence of advanced degeneration but may participate in the evolving pathology of Alzheimer's disease from an early Braak stage.

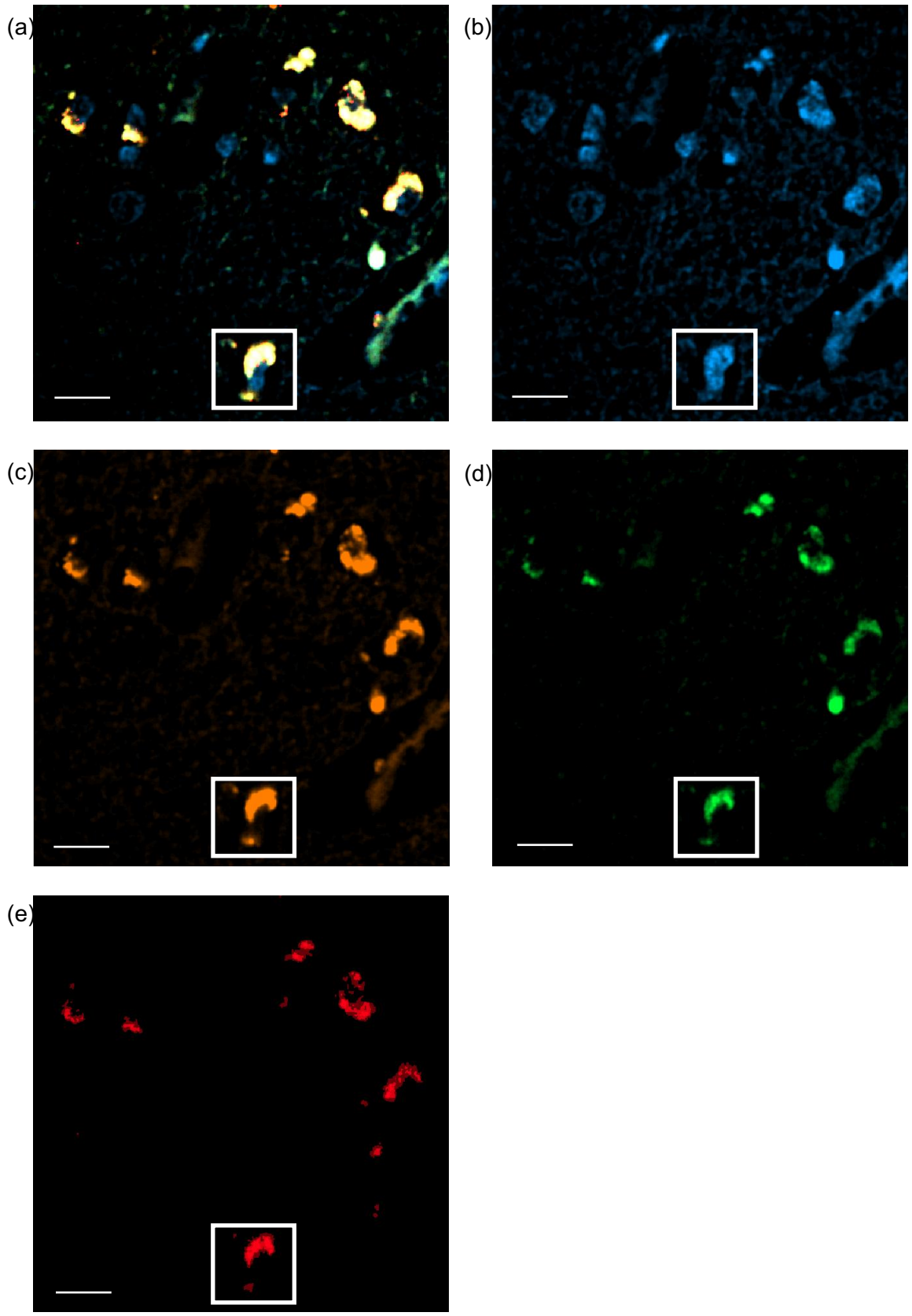

Figure 31. Multiplexing temporal lobe confocal images of DAPI, calcification, pTau, and neurons at intermediate Braak stages (P1/11) at 40x magnification, with the scale bar = 20um. (a) Overlapped image. (b) Blue-DAPI. (c) Orange-pTau. (d) Green-Neu. (e) Red-Calcification

For the late-stage Alzheimer's disease (AD) samples shown in Figure 32, the patient had been clinically diagnosed with AD. The observed patterns diverged notably from those seen in earlier stages. There was a substantial increase in the presence of calcified deposits, evident from the prominent red fluorescence in both Figure 32(a) and Figure 32(e), which aligns with the SEM quantification results shown in Chapter 4.3.3.

Within the regions highlighted by white boxes, strong calcification signals were localised to the nuclei, indicating that mineral deposition advances with disease progression, not only in quantity but also in spatial distribution. This suggests a pathological shift from peripheral or axonal mineralisation in earlier stages to more central, possibly nuclear, deposition in late-stage AD. Such nuclear involvement may signify severe cellular dysfunction, further contributing to neurodegeneration.

In addition, the immunofluorescence images revealed a more scattered pattern in both the pTau (Figure 32(c)) and calcification (Figure 32(e)) channels. Despite the diffuse nature of the pTau signal, a relatively high level of colocalisation between pTau and calcification remained when compared to other markers. This spatial pattern is consistent with the pathological redistribution of tau during AD progression. In healthy neurons, tau is predominantly localised in axons, but in AD, tau becomes hyperphosphorylated, detaches from microtubules, and mislocalises to the soma, dendrites, and even extracellular compartments. This mislocalisation promotes the formation of neurofibrillary tangles (NFTs), a pathological hallmark of AD, which disrupts neuronal function and leads to cell death. This observation supports **Hypothesis 5**, which proposes that intracellular calcification may act as a nucleation site for neurofibrillary tangle (NFT) formation. However, further investigation is needed to elucidate the extent to which calcification contributes to or drives the aggregation of hyperphosphorylated tau, and to distinguish whether its role is causative or merely correlative in the development of NFTs.

Collectively, these findings from late-stage samples highlight the evolving relationship between tau pathology and brain calcification. As AD progresses, not only does the burden of pTau increase, but its mislocalisation appears to coincide with expanding and intensifying mineralisation, suggesting a potential mechanistic link between the two processes.

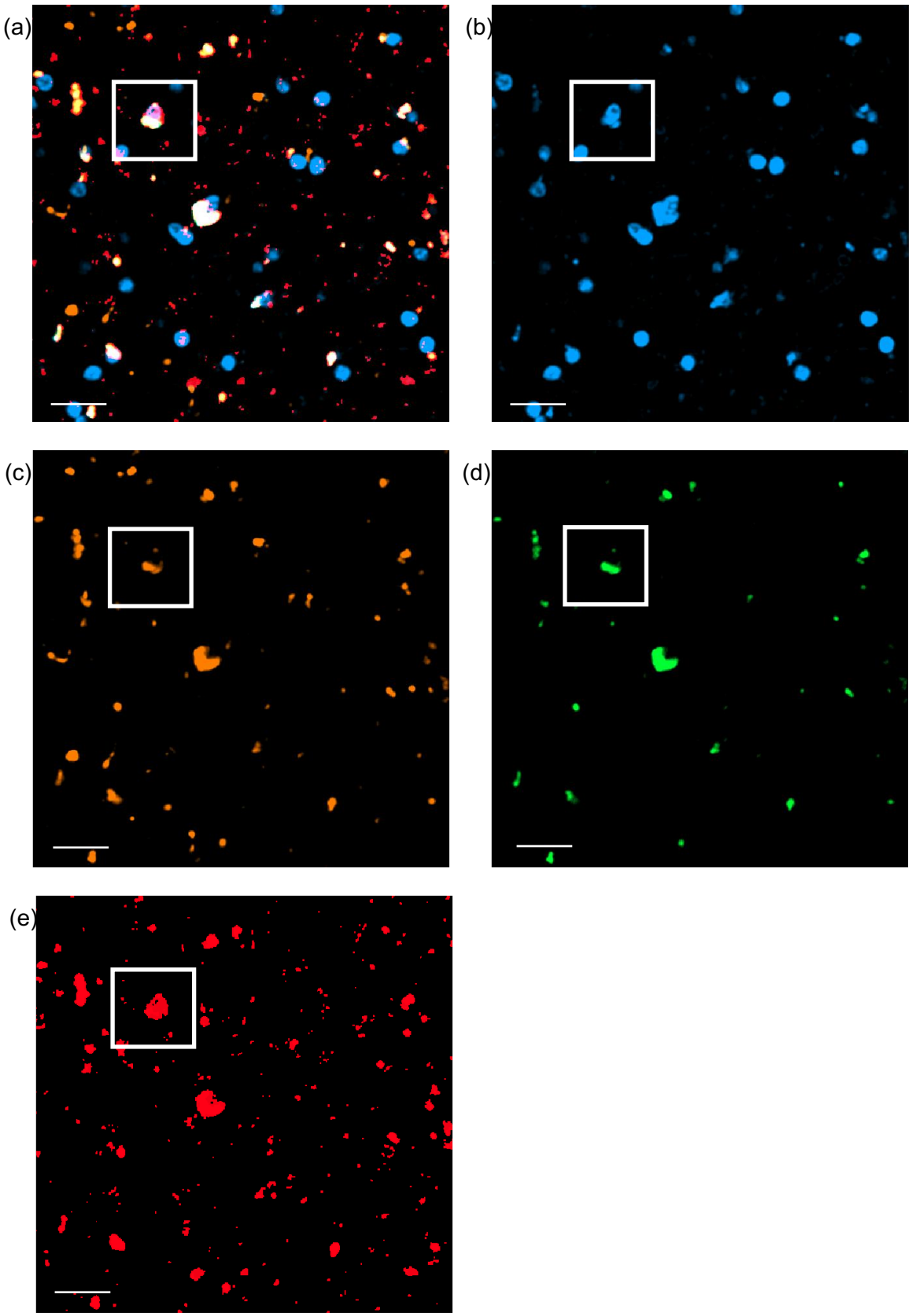

Figure 32. Multiplexing temporal lobe confocal images of DAPI, calcification, pTau, and neurons at late Braak stages (P7/11) at 40x magnification, with the scale bar = 20um. (a) Overlapped image. (b) Blue-DAPI. (c) Orange-pTau. (d) Green-Neu. (e) Red-Calcification

6.3.2 Statistical analysis of neuronal calcification colocalisation

A quantitative analysis was subsequently conducted to deepen the understanding of the relationship between calcification, phosphorylated tau (pTau), and neurons throughout Alzheimer's disease progression. Figure 33 presents a quantitative analysis of calcification overlap rates with phosphorylated tau (pTau) and neuronal markers (NeuN) in the basal ganglia, hippocampus, and temporal lobe across clinical Braak stages (Braak I–II representing early-stage AD, Braak III–IV as intermediate-stage, and Braak V–VI as late-stage AD. The overlap rates were calculated using the method outlined in Chapter 6.2.3). This analysis provides deeper insight into the spatial relationship between protein aggregation, mineral deposition, and neuronal degeneration, offering new perspectives on the potential pathological interplay underlying Alzheimer's disease progression. All the statistical differences obtained are indicated in Figure 33 with coded colour connection lines.

In the basal ganglia region, as illustrated in Figure 33(a), a statistically significant difference was observed between the early-stage CaPT and CaNeu overlap rates ($p < 0.05$). This suggests a stronger spatial, and potentially mechanistic, association between calcification and phosphorylated tau (pTau) compared to neurons at the early stages of Alzheimer's disease, despite both markers demonstrating high colocalisation with calcification. This may indicate that tau pathology is more closely linked to the initial mineralisation processes than general neuronal presence. Furthermore, a highly significant difference was also detected in the late-stage samples ($p < 0.01$), again highlighting a preferential colocalisation of calcification with pTau over NeuN. In contrast, no statistically significant difference was found in the intermediate stage, which may reflect a transitional phase in the disease where both neuronal and tau-associated calcifications coexist without a distinct dominance. This aligns with the findings presented in Chapter 4, where the intermediate stage was identified as a transitional phase during which calcification density remains relatively stable compared to earlier stages. These colocalisation findings indicate that the interaction between calcification and pTau evolves dynamically across AD progression, with potential implications for disease mechanism and biomarker development.

In the hippocampus, as shown in Figure 33(b), a statistically significant difference was observed between the intermediate-stage CaPT and CaNeu overlap rates ($p < 0.05$). This suggests that, in the hippocampus region, calcification becomes more closely associated with phosphorylated tau (pTau) than with neuronal markers

at the intermediate stage. Also, a highly significant difference was observed in the late stage ($p<0.01$). In the temporal lobe region, shown in Figure 33(c), only the late-stage inter-group statistically significant difference ($p<0.01$) was observed.

This consistent difference across three AD symptoms-associated regions suggests that late mineral deposition may be more closely associated with phosphorylated tau aggregates than with intact neurons, which has also been indicated clearly in Figure 32(a). This pattern suggests that phosphorylated tau could actively contribute to the mineralisation process, potentially through altered calcium-binding affinities or by serving as preferential nucleation sites for biomineralisation. Alternatively, calcifications might promote tau hyperphosphorylation, creating a positive feedback loop that exacerbates tau pathology. These findings support emerging theories that link abnormal tau phosphorylation not only to the formation of neurofibrillary tangles, but also to broader biochemical dysregulation, particularly disturbances in calcium homeostasis, which may contribute to or result from pathological calcification processes in Alzheimer's disease.

All three brain regions demonstrated highly significant differences ($p<0.0001$) in overlap rates between the early (Braak I–II) and intermediate (Braak III–IV) stages compared with the late stage (Braak V–VI), for both calcification–phosphorylated tau (CaPT) and calcification–neuron (CaNeu) colocalisation. These findings suggest a stage-dependent decrease in the spatial association between calcification and key pathological markers, reflecting progressive neurodegenerative changes in Alzheimer's disease. The overlap rates of CaPT and CaNeu showed a significant decline in the late stages of AD, coinciding with the onset of major clinical symptoms such as cognitive decline and memory loss.

This decline in overlap is primarily attributed to the expansion of calcified regions, as previously shown in Figure 32(e). In advanced disease stages, calcifications increasingly appear extracellular and spatially diffuse, indicating a progressive decoupling from specific cellular structures such as neurons and phosphorylated tau (pTau) aggregates. Although pTau and neuronal colocalisation rates remain moderately high, this suggests that they continue to be susceptible to mineral deposition, likely due to ongoing metabolic dysfunction and impaired calcium homeostasis. As Alzheimer's disease (AD) advances, mineralisation becomes less directly tied to tau pathology. Instead, it may reflect broader neurodegenerative changes, including widespread neuronal loss and structural breakdown of the brain

matrix. In this context, calcification may shift from being a targeted, possibly mechanistically linked process to a secondary consequence of global tissue degeneration. This transition highlights the importance of disease stage in interpreting the functional significance of brain calcification and suggests that its pathological role may evolve throughout AD progression.

Cross-regional comparisons for each stage (Braak I-II, Braak III-IV and Braak V-VI group) are presented in Figure 34, highlighting only statistically significant differences observed within the same disease stages. A clear and consistent trend emerges in the spatial distribution of calcification relative to phosphorylated tau (pTau, Figure 34(a)) and neuronal markers (NeuN, Figure 34(b)). Within each Braak group, all three brain regions—basal ganglia, hippocampus, and temporal lobe—exhibit remarkably similar patterns of colocalisation. Notably, no statistically significant differences were detected among regions within the same disease stage. These findings suggest that the spatial relationship between calcification and pTau remains relatively stable across different brain regions at each stage of Alzheimer's disease progression. This uniformity implies a common underlying mechanism of mineral deposition associated with tau pathology, regardless of regional anatomical variation.

The calcification–neuron (CaNeu) association shown in Figure 34(b) follows a broadly similar pattern to the calcification–pTau (CaPT) relationship, with generally consistent colocalisation levels across brain regions at each Braak stage. However, a statistically significant difference was observed in the intermediate stage (Braak III–IV) between the hippocampus and temporal lobe regions. This difference may reflect region-specific vulnerability during the transitional phase of Alzheimer's disease. The hippocampus, typically affected earlier in AD, may undergo more intense neuronal degeneration at this stage, while the temporal lobe shows a different trajectory. These findings suggest that neuronal calcification may be modulated by local factors such as metabolic activity or synaptic density.

Moreover, the colocalisation between calcification and phosphorylated tau (CaPT) remains more stable across disease stages compared to the calcification-neuron (CaNeu) association. This consistent spatial relationship suggests that CaPT may serve as a more reliable and specific indicator of Alzheimer's disease progression. The stronger correlation with pTau highlights the potential of CaPT as an early and efficient predictive marker for AD-related pathology, potentially offering greater diagnostic utility than general neuronal colocalisation.

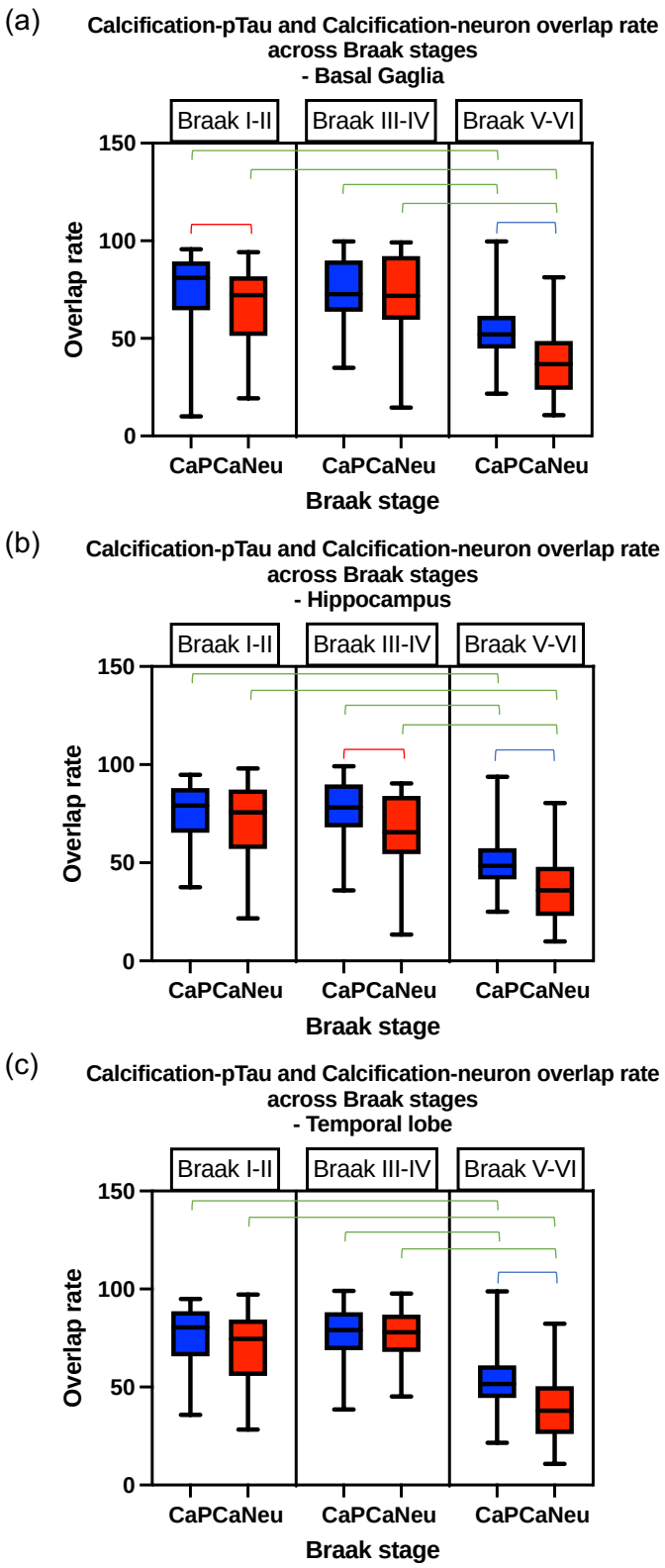

Figure 33. Box chart analysis of the calcification overlap rate across Braak stages. Blue box – Calcification pTau colocalisation rate, red box – calcification and neuron colocalisation rate. Red connection lines indicate statistically significant differences at $p < 0.05$, blue lines indicate $p < 0.01$, and green lines indicate $p < 0.0001$. (a) Basal Ganglia (b) Hippocampus (c) Temporal lobe.

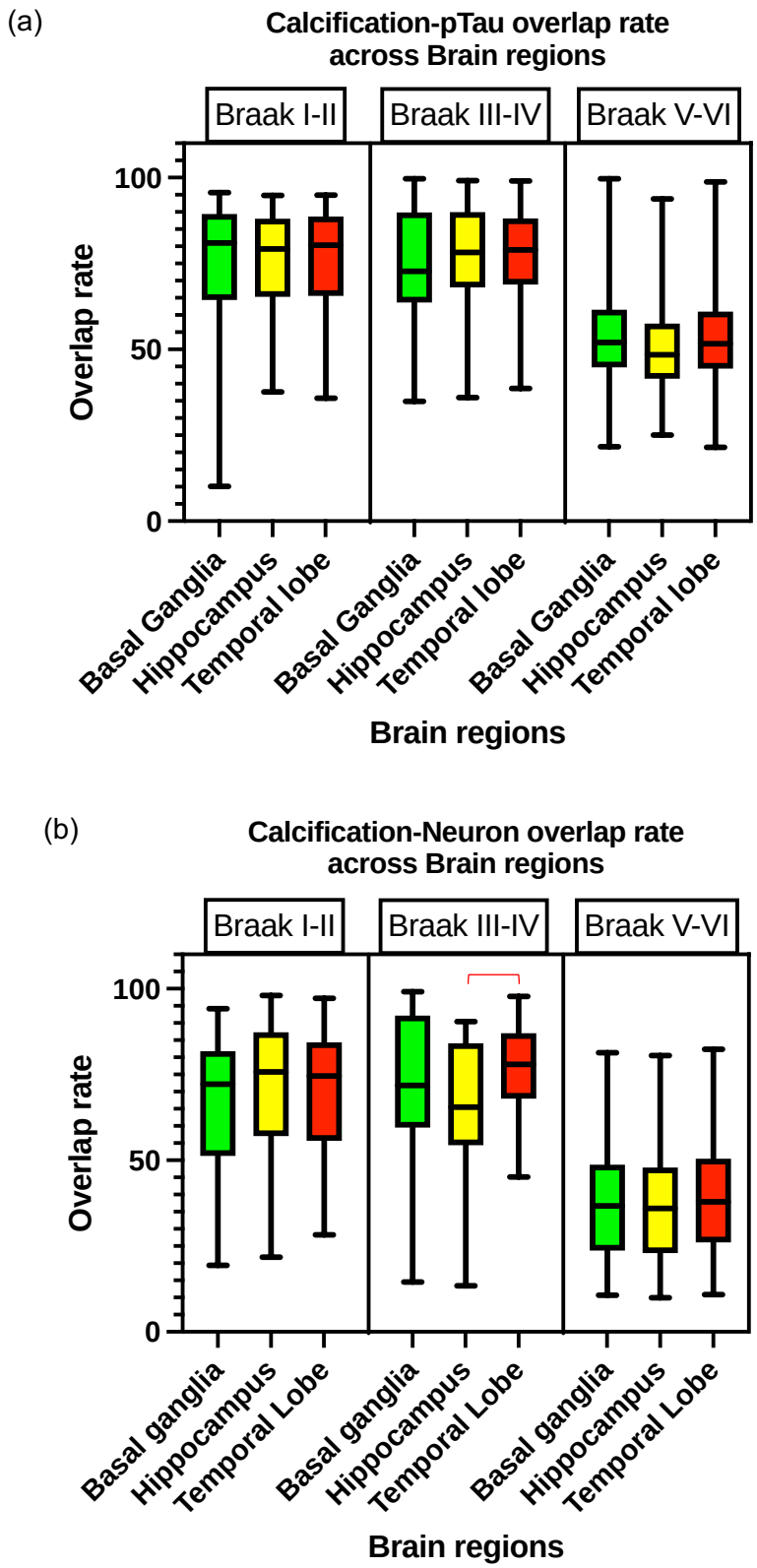

Figure 34. Box chart analysis of the calcification overlap rate across Braak stages. Green – basal ganglia, yellow – hippocampus, red – temporal lobe. Red connection lines indicate statistically significant differences at $p < 0.05$. (a) Calcification and pTau overlap rate across Braak stages. (b) Calcification and Neuron overlap rate across Braak stages. (Cross-stage significant differences are not labelled)

6.4 Conclusion and Future Work

The findings from the colocalisation analysis of calcification, phosphorylated tau (pTau), and neuronal markers provide strong inverse support for Hypothesis 4, which posited that the spatial co-localisation of neuronal cells, hyperphosphorylated tau proteins, and intracellular calcifications diminishes as Alzheimer's disease progresses through the Braak stages. As the disease advances, particularly from intermediate to late stages, a significant decline in the overlap between calcification and both pTau and neuronal markers was observed. This suggests that while early-stage mineralisation is closely associated with intracellular and tau-related pathological processes, late-stage calcifications become increasingly independent, diffusely distributed, and potentially extracellular. These results reinforce the notion that microcalcification may play a dynamic, stage-dependent role in Alzheimer's pathology, with strong cellular associations in the early stages giving way to broader, non-specific accumulation as neurodegeneration intensifies.

Although the calcification–pTau (CaPT) and calcification–neuron (CaNeu) overlaps rates exhibit a broadly similar pattern across Braak stages, the CaPT values are consistently higher than those of CaNeu. This indicates that microcalcifications in Alzheimer's disease (AD) are more closely associated with phosphorylated tau than with general neuronal structures. Such a finding suggests that tau hyperphosphorylation may play a more direct role in initiating or promoting mineralisation than the presence of neuronal cells alone. The stronger spatial association between calcification and pTau supports Hypothesis 5 that tau pathology could be a key driver of intracellular calcium phosphate deposition, highlighting CaPT as a potentially more specific and sensitive indicator of AD progression.

However, additional research is needed to further validate Hypothesis 5. While current findings reveal a strong spatial association between phosphorylated tau and calcification, causality has yet to be fully established. Future studies should aim to dissect the mechanistic relationship between tau hyperphosphorylation and mineralisation at the molecular level—such as determining whether tau aggregates directly nucleate calcium phosphate formation or if altered cellular conditions caused by tau pathology indirectly facilitate mineral deposition. Advanced imaging techniques, in vitro tau manipulation models, and temporal studies tracking early tau aggregation and mineralisation events could provide critical insights. Clarifying this relationship

may not only solidify the role of tau in pathological calcification but also open avenues for therapeutic interventions targeting early mineralisation processes as a strategy to slow AD progression.

Chapter 7: Conclusion

7.1 Summary of results

This work has generated new evidence on the presence of microcalcifications in brain tissues from both clinically diagnosed Alzheimer's disease (AD) patients and age-matched individuals who had not yet received an AD diagnosis but exhibited pathological Braak staging. The results are structured according to the primary research hypotheses and cover mineral composition, regional distribution, and colocalisation with disease-related markers. These findings expand our understanding of early-stage AD pathology and suggest that microcalcification may occur before the onset of clinical symptoms, reinforcing its potential as an early marker of disease progression.

This study represents the first systematic investigation of microcalcification in Alzheimer's disease (AD) concerning the pathological staging system known as the Braak stages. The results demonstrate a clear increase in calcification density with advancing disease severity, revealing strong and statistically significant correlations with Braak stage progression. These findings establish a robust association between microcalcification and the pathological development of AD, advancing the role of calcification in AD progression.

Moreover, the in vitro simulation model successfully reproduced calcium phosphate deposition in mouse brain tissue, closely mimicking the intracellular calcification patterns observed in human Braak-staged samples. However, the results from the protein-level simulation experiments were inconclusive, with no definitive evidence supporting protein-driven mineralisation under the conditions tested. These findings highlight the importance of intracellular calcification in disease progression. Nonetheless, the presence of dense structures in protein simulations suggests a potential association between protein aggregation and mineral deposition. These findings underscore the importance of intracellular calcification in the progression of Alzheimer's disease and highlight the need for further investigation into its mechanistic links with protein pathology.

Finally, the marked decline in the colocalisation of calcification with phosphorylated tau (pTau) and neuronal markers during the late stages of Alzheimer's disease suggests a progressive spatial dissociation between mineral deposits and cellular or protein structures. This reduction in colocalisation, when considered

alongside the significant increase in overall calcification density, points to a potential shift in the underlying mechanisms driving mineralisation and tau aggregation. Rather than proceeding through a single, unified pathway, these findings imply that calcification and pTau pathology may become increasingly independent processes as the disease advances. This divergence highlights the complexity of Alzheimer's progression and unveils new avenues for exploring disease-specific mechanisms of neurodegeneration and pathological mineralisation.

7.2 Limitations and challenges

This study faced several challenges and limitations, some of which were addressed during the research process, while others remain unresolved and warrant further attention.

One significant limitation lies in the imbalanced sample distribution across Braak stages, which constrained the statistical robustness of stage-specific analyses. Although meaningful correlations were established between calcification density and Alzheimer's disease progression, the limited number of samples in a single stage reduced the power of inferential statistics. For instance, only a single Braak stage IV sample was available for the calcification density analysis in the basal ganglia, hippocampus, and temporal lobe regions. This uneven distribution restricts the ability to generalise trends or detect subtle transitions between intermediate disease stages. For example, several close 0.05 significant differences were obtained during the study. Future studies with larger, more balanced cohorts across all Braak stages are necessary to validate the current findings and refine our understanding of stage-dependent pathological mineralisation. Additionally, a major challenge arose from the limited availability of age-matched samples across UK brain banks. This scarcity constrained the selection of appropriate control groups and introduced unavoidable variability in age distribution, making it difficult to isolate age-specific effects from underlying pathological changes.

Moreover, in the simulation model, the use of an artificial interstitial (interneuron) fluid was initially proposed as a secondary simulation medium to replicate the in vivo extracellular environment of the brain more closely. The interstitial fluid requires careful regulation of multiple ions—including calcium, magnesium, phosphate, and bicarbonate—at physiologically relevant concentrations and ratios. Even minor deviations can lead to precipitation artefacts or interfere with protein interactions, compromising the validity of the model. As a result, this aspect of the study was not implemented, representing a missed opportunity to explore a potentially important aspect of mineralisation dynamics. Future development of more robust formulations or microfluidic systems capable of maintaining ionic homeostasis could enable more physiologically relevant simulations and deepen our understanding of calcification processes in Alzheimer's disease.

Furthermore, the protein-level simulation did not yield conclusive results, primarily due to limited observable calcification and the presence of potential sample contamination. Despite using various tau protein isoforms and phosphorylation variants, mineral deposition remained minimal or inconsistent, making it difficult to establish a definitive correlation between tau proteins and calcium phosphate nucleation. In addition, suspected microbial or particulate contamination in some samples introduced further ambiguity in interpreting the high-density structures observed under transmission electron microscopy (TEM). These limitations hindered the ability to confidently attribute mineralisation to specific protein-driven mechanisms. Future optimisation of protein concentration, simulation conditions, and contamination control—possibly through sterile handling, microfluidic environments, or more precise ion-buffering systems—will be essential for accurately investigating the role of tau and phosphorylated tau in intracellular calcification pathways relevant to Alzheimer's disease.

The SDS-PAGE analysis was constrained by the discontinuation of the tau-441 protein previously supplied by Abcam, which had originally been selected as the primary control. The unavailability of this reference material introduced challenges in ensuring experimental consistency, as alternative commercial sources may differ in purity, post-translational modifications, or buffer composition. Furthermore, the need to reformulate the control strategy led to delays and incompletion in method standardisation and limited the robustness of the protein characterisation.

7.3 Scientific contribution

This work represents the first comprehensive investigation into the relationship between brain calcification and the pathological Braak staging system, which is widely used to assess the pathological progression of Alzheimer's disease (AD). This study provides new insights into the spatial distribution, morphological characteristics, and stage-dependent changes of calcium phosphate deposits in AD-affected brains. Importantly, the study establishes a clear correlation between calcification density and advancing Braak stages, supporting that mineralisation is not incidental but may reflect an underlying pathological process linked to disease severity.

In addition, this research contributes novel evidence showing that microcalcification is present even in early Braak-staged samples, suggesting its potential as an early biomarker for AD. The application of high-resolution imaging and immunofluorescence colocalisation techniques has revealed strong spatial associations between calcification, phosphorylated tau (pTau), and neuronal cells during early and intermediate stages, providing mechanistic insights into the interplay between protein aggregation and mineral deposition.

In summary, this work not only highlights the pathological relevance of brain calcification in Alzheimer’s disease but also opens new directions for research into its diagnostic and therapeutic implications.

7.4 Future work

Building on the findings of this study, future research should focus on three key areas to further investigate the role of microcalcification in Alzheimer's disease (AD) pathology and expand the mechanistic understanding of its association with tau pathology.

1. Increasing Sample Size and Regional Diversity

One of the primary limitations of the current study was the imbalanced distribution of samples across Braak stages, particularly the underrepresentation of Braak stage IV. This limited the statistical power and may have prevented some observed trends from reaching conventional significance thresholds (e.g., $p \approx 0.05$). Future work should incorporate a larger and more evenly distributed cohort of human brain specimens to increase statistical robustness and validate the observed trends in calcification density and distribution. A well-balanced sample set will also improve the reliability of group comparisons and strengthen confidence in stage-dependent interpretations of mineral accumulation.

Additionally, the inclusion of more brain regions—especially those affected in other neurodegenerative conditions—would allow for a broader understanding of whether microcalcification is specific to Alzheimer's disease or part of a more generalised neurodegenerative process. Investigating regions implicated in diseases such as Parkinson's, Huntington's, or frontotemporal dementia may help determine whether calcification is a disease-specific biomarker or a shared pathological feature across disorders.

2. Advancing Protein-Level Mineralisation Analysis

Although the in vitro simulation model successfully reproduced AD-like mineralisation in brain tissues, protein-level simulations yielded inconclusive results due to limited mineral deposition and possible sample contamination. To address this, future work should employ more advanced techniques to better characterise mineral-protein interactions. For example, cryo-electron microscopy, immunogold labelling, and correlative light and electron microscopy (CLEM) could provide higher resolution and more specific localisation of mineral phases within protein aggregates.

Furthermore, post-incubation validation of protein integrity and phosphorylation status—via methods such as Western blotting or mass spectrometry—should be included to assess whether mineralisation conditions selectively degrade or preserve

specific protein species. Improved sample purity, refined incubation protocols, and real-time tracking of mineralisation would allow more precise characterisation of the interaction between tau proteins and calcium phosphate. These improvements may clarify whether specific tau variants or phosphorylation states preferentially initiate or promote mineralisation under near-physiological conditions.

3. Mechanistic Investigation of Tau-Driven Mineralisation

While current results support Hypothesis 5—suggesting a strong spatial association between phosphorylated tau (pTau) and intracellular calcification—the directionality and causality of this relationship remain unresolved. Future studies should aim to dissect the molecular mechanisms underlying this association. One critical question is whether hyperphosphorylated tau directly nucleates calcium phosphate crystals or whether tau pathology merely creates a cellular environment conducive to mineral deposition through altered calcium homeostasis or oxidative stress.

To address this, research could utilise tau overexpression or knockdown models in vitro, combined with mineralisation assays, to track the temporal sequence of tau aggregation and mineral deposition. Additional investigations using genetically engineered cell lines or animal models with inducible tau phosphorylation could provide mechanistic insights into how tau pathology influences the mineralisation process. Such studies would help determine whether calcification is a downstream consequence of tau dysfunction or an active participant in neuronal degeneration.

Ultimately, a clearer understanding of the tau-calcification relationship could provide new biomarkers for early-stage AD or identify novel therapeutic targets aimed at modulating mineralisation processes to slow disease progression.

Appendix

Collaboration work

Partial cohort of samples analysed in this study was also examined in the previously published paper *'Nuclear and cellular, micro- and nano-calcification in Alzheimer's disease patients and correlation to phosphorylated Tau'*. In that earlier work, the samples were categorised based on clinical diagnosis, distinguishing between clinically confirmed Alzheimer's disease and non-clinical but with pathological indication cases. The primary aim was to describe calcification features in relation to clinical AD status.

In contrast, the present study adopts a fundamentally different analytical framework by grouping samples according to Braak stages, a pathological staging system that reflects the progression of Tau pathology within the brain. This shift from a clinical to a neuropathological classification enables a more granular investigation into how calcification relates to disease progression at the tissue and cellular levels. By aligning the analysis with Braak staging, additional samples were applied in this study, and places greater emphasis on mechanistic insights and the temporal evolution of pathology, thereby extending and deepening the interpretations drawn from the previous work.

Reference

1. Association, A.s., *2024 ALZHEIMER'S DISEASE FACTS AND FIGURES.* 2024.
2. Ballard, C., et al., *Alzheimer's disease.* The Lancet, 2011. **377**(9770): p. 1019-1031.
3. Barbe, C., et al., *Impact of functional alterations on quality of life in patients with Alzheimer's disease.* Aging & Mental Health, 2017. **21**(5): p. 571-576.
4. Swerdlow, R.H., *Is aging part of Alzheimer's disease, or is Alzheimer's disease part of aging?* Neurobiology of Aging, 2007. **28**(10): p. 1465-1480.
5. Alzheimer, A., *Uber eigenartige Erkrankung der Hirnrinde.* All Z Psychiatr, 1907. **64**: p. 146-148.
6. Arvanitakis, Z., R.C. Shah, and D.A. Bennett, *Diagnosis and Management of Dementia: Review.* JAMA, 2019. **322**(16): p. 1589-1599.
7. Speechly, C.M., C. Bridges-Webb, and E. Passmore, *The pathway to dementia diagnosis.* Medical Journal of Australia, 2008. **189**(9): p. 487-489.
8. WHO, *Global action plan on the public health response to dementia 2017-2025.* 2017.
9. Edwards, S., et al., *Real world outcomes, healthcare utilisation and costs of Alzheimer's disease in England.* Aging and Health Research, 2024. **4**(1): p. 100180.
10. Lippa, C.F., et al., *Alzheimer's disease and aging: Effects on perforant pathway perikarya and synapses.* Neurobiology of Aging, 1992. **13**(3): p. 405-411.
11. Hughes, J.C., *Thinking through dementia*. 2011: Oxford University Press.
12. Blennow, K., M.J. de Leon, and H. Zetterberg, *Alzheimer's disease.* The Lancet, 2006. **368**(9533): p. 387-403.
13. Dauphinot, V., et al., *Economic and caregiver impact of Alzheimer's disease across the disease spectrum: a cohort study.* Alzheimer's Research & Therapy, 2022. **14**(1): p. 34.
14. Prince, M., et al., *World Alzheimer Report 2016.Improving healthcare for people living with dementia: Coverage, Quality and costs now and in the future*. 2016, Alzheimer's Disease International.
15. Nichols, E., et al., *Estimation of the global prevalence of dementia in 2019 and forecasted prevalence in 2050: an analysis for the Global Burden of Disease Study 2019.* The Lancet Public Health, 2022. **7**(2): p. e105-e125.
16. Niu, H., Álvarez-Álvarez, I., Guillén-Grima, F., & Aguinaga-Ontoso, I. , *Prevalence and incidence of Alzheimer's disease in Europe: A meta-analysis.* Neurología (English Edition, 2017. **32(8), 523-532**.
17. Froelich, L., et al., *Quality of life and caregiver burden of Alzheimer's Disease among community dwelling patients in Europe: Variation by disease severity and progression.* Journal of Alzheimer's Disease Reports, 2021. **5**(1): p. 791-804.
18. Robinson, K.M., P. Adkisson, and S. Weinrich, *Problem behaviour, caregiver reactions, and impact among caregivers of persons with Alzheimer's disease.* Journal of Advanced Nursing, 2001. **36**(4): p. 573-582.
19. Alavi Naini, S.M. and N. Soussi-Yanicostas, *Tau Hyperphosphorylation and Oxidative Stress, a Critical Vicious Circle in Neurodegenerative Tauopathies?* Oxidative Medicine and Cellular Longevity, 2015. **2015**(1): p. 151979.

20. Shin, R.W., et al., *Increased tau accumulation in senile plaques as a hallmark in Alzheimer's disease.* Am J Pathol, 1989. **134**(6): p. 1365-71.
21. Wang, J.-Z., et al., *Abnormal Hyperphosphorylation of Tau: Sites, Regulation, and Molecular Mechanism of Neurofibrillary Degeneration.* Journal of Alzheimer's Disease, 2013. **33**: p. S123-S139.
22. Behrouz, N., et al., *The Immunohistochemical Evidence of Amyloid Diffuse Deposits As a Pathological Hallmark in Alzheimer's Disease.* Journal of Gerontology, 1991. **46**(6): p. B209-B212.
23. Takeda, S., et al., *Plasma β-amyloid as potential biomarker of Alzheimer disease: possibility of diagnostic tool for Alzheimer disease.* Molecular BioSystems, 2010. **6**(10): p. 1760-1766.
24. Lue, L.-F., A. Guerra, and D.G. Walker, *Amyloid beta and tau as Alzheimer's disease blood biomarkers: promise from new technologies.* Neurology and therapy, 2017. **6**: p. 25-36.
25. Al Mamun, A., et al., *Toxic tau: structural origins of tau aggregation in Alzheimer's disease.* Neural Regeneration Research, 2020. **15**(8): p. 1417-1420.
26. Guo, T., W. Noble, and D.P. Hanger, *Roles of tau protein in health and disease.* Acta Neuropathologica, 2017. **133**(5): p. 665-704.
27. Connett, P., et al. *Mineralization in biological systems*. in *Inorganic elements in biochemistry*. 1983. Springer.
28. Giachelli, C.M., *Ectopic calcification: gathering hard facts about soft tissue mineralization.* The American journal of pathology, 1999. **154**(3): p. 671-675.
29. Nancollas, G.H., *The mechanism of biological mineralization.* Journal of Crystal Growth, 1977. **42**: p. 185-193.
30. Tsolaki, E. and S. Bertazzo, *Pathological Mineralization: The Potential of Mineralomics.* Materials, 2019. **12**(19): p. 3126.
31. Vidavsky, N., J.A.M.R. Kunitake, and L.A. Estroff, *Multiple Pathways for Pathological Calcification in the Human Body.* Advanced Healthcare Materials, 2021. **10**(4): p. 2001271.
32. Clarke, B., *Normal bone anatomy and physiology.* Clin J Am Soc Nephrol, 2008. **3 Suppl 3**(Suppl 3): p. S131-9.
33. Chhiber, N., et al., *Mineralization in health and mechanism of kidney stone formation.* International Journal of Pharmaceutical Science Invention, 2014. **3**(1): p. 25-31.
34. Zhao, Y., et al., *Characterization of Dystrophic Calcification Induced in Mice by Cardiotoxin.* Calcified Tissue International, 2009. **85**(3): p. 267-275.
35. Fleisch, H., et al., *Chapter 78 - Bisphosphonates: Mechanisms of Action*, in *Principles of Bone Biology (Second Edition)*, J.P. Bilezikian, L.G. Raisz, and G.A. Rodan, Editors. 2002, Academic Press: San Diego. p. 1361-XLIII.
36. WELLS, H.G., *METASTATIC CALCIFICATION.* Archives of Internal Medicine, 1915. **XV**(4): p. 574-580.
37. Aikawa, E. and J.D. Hutcheson, *Cardiovascular calcification and bone mineralization*. 2020: Springer.
38. Bos, D., et al., *Calcification in major vessel beds relates to vascular brain disease.* Arteriosclerosis, thrombosis, and vascular biology, 2011. **31**(10): p. 2331-2337.
39. Thompson, B. and D.A. Towler, *Arterial calcification and bone physiology: role of the bone–vascular axis.* Nature Reviews Endocrinology, 2012. **8**(9): p. 529-543.

40. Cooke, C.A., C. McAvoy, and R. Best, *Idiopathic sclerochoroidal calcification.* British Journal of Ophthalmology, 2003. **87**(2): p. 245-246.
41. Kobayashi, S., et al., *Idiopathic nonarteriosclerotic cerebral calcification (Fahr's disease): an electron microscopic study.* Acta neuropathologica, 1987. **73**: p. 62-66.
42. Mufaddel, A.A. and G.A. Al-Hassani, *Familial idiopathic basal ganglia calcification (Fahr's disease).* Neurosciences Journal, 2014. **19**(3): p. 171-177.
43. Mahlberg, R., et al., *Pineal calcification in Alzheimer's disease: an in vivo study using computed tomography.* Neurobiology of aging, 2008. **29**(2): p. 203-209.
44. Friedland, R.P., J.S. Luxenberg, and E. Koss, *A Quantitative Study of Intracranial Calcification in Dementia of the Alzheimer Type.* International Psychogeriatrics, 1990. **2**(1): p. 37-43.
45. Román, G. and B. Pascual, *Contribution of neuroimaging to the diagnosis of Alzheimer's disease and vascular dementia.* Archives of medical research, 2012. **43**(8): p. 671-676.
46. Deng, H., W. Zheng, and J. Jankovic, *Genetics and molecular biology of brain calcification.* Ageing Research Reviews, 2015. **22**: p. 20-38.
47. Chew, A.P.T., et al., *Hippocampal Calcification Prevalence at CT: A Retrospective Review.* Radiology, 2012. **265**(2): p. 504-510.
48. Mahy, N., et al., *Basal ganglia calcification induced by excitotoxicity: an experimental model characterised by electron microscopy and X-ray microanalysis.* Acta Neuropathologica, 1999. **98**(3): p. 217-225.
49. Bartnicka, J.J. and P.J. Blower, *Insights into Trace Metal Metabolism in Health and Disease from PET: "PET Metallomics".* Journal of Nuclear Medicine, 2018. **59**(9): p. 1355-1359.
50. Dixon, S.J. and B.R. Stockwell, *The role of iron and reactive oxygen species in cell death.* Nature Chemical Biology, 2014. **10**(1): p. 9-17.
51. Bulk, M., et al., *Cerebral amyloid angiopathy with vascular iron accumulation and calcification: a high-resolution magnetic resonance imaging histopathology study.* Stroke, 2018. **49**(9): p. 2081-2087.
52. Jakaria, M., et al., *Ferroptosis as a mechanism of neurodegeneration in Alzheimer's disease.* Journal of Neurochemistry, 2021. **159**(5): p. 804-825.
53. Xie, Y., et al., *Ferroptosis: process and function.* Cell Death & Differentiation, 2016. **23**(3): p. 369-379.
54. Anekonda, T.S. and J.F. Quinn, *Calcium channel blocking as a therapeutic strategy for Alzheimer's disease: The case for isradipine.* Biochimica et Biophysica Acta (BBA) - Molecular Basis of Disease, 2011. **1812**(12): p. 1584-1590.
55. Gleichmann, M. and M.P. Mattson, *Neuronal calcium homeostasis and dysregulation.* Antioxidants & redox signaling, 2011. **14**(7): p. 1261-1273.
56. Schober, R., et al., *Senile plaque calcification of the lamina circumvoluta medullaris in Alzheimer's disease.* Neuropathology, 2021. **41**(5): p. 366-370.
57. Guan, P.-P., L.-L. Cao, and P. Wang, *Elevating the Levels of Calcium Ions Exacerbate Alzheimer's Disease via Inducing the Production and Aggregation of β-Amyloid Protein and Phosphorylated Tau.* International Journal of Molecular Sciences, 2021. **22**(11): p. 5900.
58. Bassett, D.S. and M.S. Gazzaniga, *Understanding complexity in the human brain.* Trends in cognitive sciences, 2011. **15**(5): p. 200-209.

59. Carter, R., *The brain book: An illustrated guide to its structure, functions, and disorders*. 2019: Dorling Kindersley Ltd.
60. Himmler, A., et al., *Tau consists of a set of proteins with repeated C-terminal microtubule-binding domains and variable N-terminal domains.* Molecular and cellular biology, 1989. **9**(4): p. 1381-1388.
61. Brion, J.P., et al., *Tau in Alzheimer neurofibrillary tangles. N-and C-terminal regions are differentially associated with paired helical filaments and the location of a putative abnormal phosphorylation site.* Biochemical journal, 1991. **273**(1): p. 127-133.
62. Avila, J., et al., *Tau structures.* Frontiers in aging neuroscience, 2016. **8**: p. 262.
63. AVILA, J., et al., *Role of Tau Protein in Both Physiological and Pathological Conditions.* Physiological Reviews, 2004. **84**(2): p. 361-384.
64. Dujardin, S. and B.T. Hyman, *Tau prion-like propagation: state of the art and current challenges.* Tau Biology, 2020: p. 305-325.
65. Brat, D.J., et al., *Tau-associated neuropathology in ganglion cell tumours increases with patient age but appears unrelated to ApoE genotype.* Neuropathology and applied neurobiology, 2001. **27**(3): p. 197-205.
66. Goedert, M. and M.G. Spillantini, *Propagation of Tau aggregates.* Molecular brain, 2017. **10**: p. 1-9.
67. Colbran, R.J., *Protein phosphatases and calcium/calmodulin-dependent protein kinase II-dependent synaptic plasticity.* Journal of Neuroscience, 2004. **24**(39): p. 8404-8409.
68. Llorens-Marítin, M., et al., *GSK-3β, a pivotal kinase in Alzheimer disease.* Frontiers in molecular neuroscience, 2014. **7**: p. 46.
69. Pei, J.-J., et al., *Distribution of active glycogen synthase kinase 3β (GSK-3β) in brains staged for Alzheimer disease neurofibrillary changes.* Journal of neuropathology and experimental neurology, 1999. **58**(9): p. 1010-1019.
70. Martin, L., et al., *Tau protein kinases: involvement in Alzheimer's disease.* Ageing research reviews, 2013. **12**(1): p. 289-309.
71. Iqbal, K., C.-X. Gong, and F. Liu, *Hyperphosphorylation-induced tau oligomers.* Frontiers in neurology, 2013. **4**: p. 112.
72. Shahani, N. and R. Brandt, *Functions and malfunctions of the tau proteins.* Cellular and Molecular Life Sciences CMLS, 2002. **59**(10): p. 1668-1680.
73. Mandelkow, E.-M., et al., *Tau domains, phosphorylation, and interactions with microtubules.* Neurobiology of aging, 1995. **16**(3): p. 355-362.
74. Makrides, V., et al., *Evidence for two distinct binding sites for tau on microtubules.* Proceedings of the national academy of sciences, 2004. **101**(17): p. 6746-6751.
75. Weingarten, M.D., et al., *A protein factor essential for microtubule assembly.* Proceedings of the National Academy of Sciences, 1975. **72**(5): p. 1858-1862.
76. Bettens, K., K. Sleegers, and C. Van Broeckhoven, *Genetic insights in Alzheimer's disease.* The lancet neurology, 2013. **12**(1): p. 92-104.
77. Neuner, S.M., T. Julia, and A.M. Goate, *Genetic architecture of Alzheimer's disease.* Neurobiology of disease, 2020. **143**: p. 104976.
78. De Brouwer, E.J., et al., *Hippocampal calcifications: risk factors and association with cognitive function.* Radiology, 2018. **288**(3): p. 815-820.
79. Ju, Y. and K.Y. Tam, *Pathological mechanisms and therapeutic strategies for Alzheimer's disease.* Neural Regeneration Research, 2022. **17**(3): p. 543-549.

80. Kueper, J.K., M. Speechley, and M. Montero-Odasso, *The Alzheimer's disease assessment scale–cognitive subscale (ADAS-Cog): modifications and responsiveness in pre-dementia populations. a narrative review.* Journal of Alzheimer's Disease, 2018. **63**(2): p. 423-444.
81. Heiko Braak, E.B., *Staging of Alzheimer-related Cortical Destruction.* International Psychogeriatrics, 1997. **9**(S1): p. 257-261.
82. Tahami Monfared, A.A., et al., *Alzheimer's disease: epidemiology and clinical progression.* Neurology and therapy, 2022. **11**(2): p. 553-569.
83. Bolognin, S., et al., *Chelation therapy for neurodegenerative diseases.* Medicinal Research Reviews, 2009. **29**(4): p. 547-570.
84. Jann, M.W., *Rivastigmine, a new-generation cholinesterase inhibitor for the treatment of Alzheimer's disease.* Pharmacotherapy: The Journal of Human Pharmacology and Drug Therapy, 2000. **20**(1): p. 1-12.
85. Aisen, P.S., *The development of anti-amyloid therapy for Alzheimer's disease: from secretase modulators to polymerisation inhibitors.* CNS drugs, 2005. **19**: p. 989-996.
86. Srivastava, S., R. Ahmad, and S.K. Khare, *Alzheimer's disease and its treatment by different approaches: A review.* European Journal of Medicinal Chemistry, 2021. **216**: p. 113320.
87. Braak, H. and E. Braak, *Neuropathological stageing of Alzheimer-related changes.* Acta neuropathologica, 1991. **82**(4): p. 239-259.
88. Braak, H. and K. Del Tredici, *The preclinical phase of the pathological process underlying sporadic Alzheimer's disease.* Brain, 2015. **138**(10): p. 2814-2833.
89. Braak, H., et al., *Stages of the pathologic process in Alzheimer disease: age categories from 1 to 100 years.* Journal of Neuropathology & Experimental Neurology, 2011. **70**(11): p. 960-969.
90. Lowe, V.J., et al., *Widespread brain tau and its association with ageing, Braak stage and Alzheimer's dementia.* Brain, 2018. **141**(1): p. 271-287.
91. Isaacson, R., *The limbic system*. 2013: Springer Science & Business Media.
92. Pini, L., et al., *Brain atrophy in Alzheimer's Disease and aging.* Ageing Research Reviews, 2016. **30**: p. 25-48.
93. Parra Bravo, C., S.A. Naguib, and L. Gan, *Cellular and pathological functions of tau.* Nature Reviews Molecular Cell Biology, 2024.
94. Balsis, S., et al., *How do scores on the ADAS-Cog, MMSE, and CDR-SOB correspond?* The Clinical Neuropsychologist, 2015. **29**(7): p. 1002-1009.
95. Gold, G., et al., *Clinical validity of Braak neuropathological staging in the oldest-old.* Acta neuropathologica, 2000. **99**: p. 579-582.
96. Galasko, D., et al., *The Mini-Mental State Examination in the early diagnosis of Alzheimer's disease.* Archives of neurology, 1990. **47**(1): p. 49-52.
97. Demer, L.L. and Y. Tintut, *Vascular calcification: pathobiology of a multifaceted disease.* Circulation, 2008. **117**(22): p. 2938-2948.
98. Nag, S., J.L. Takahashi, and D.W. Kilty, *Role of vascular endothelial growth factor in blood-brain barrier breakdown and angiogenesis in brain trauma.* Journal of Neuropathology & Experimental Neurology, 1997. **56**(8): p. 912-921.
99. Greenberg, S.M., et al., *Detection of isolated cerebrovascular β-amyloid with Pittsburgh compound B.* Annals of Neurology: Official Journal of the American Neurological Association and the Child Neurology Society, 2008. **64**(5): p. 587-591.

100. Hall, B., et al., *In vivo tau PET imaging in dementia: pathophysiology, radiotracer quantification, and a systematic review of clinical findings.* Ageing research reviews, 2017. **36**: p. 50-63.
101. Jack Jr, C.R., et al., *Longitudinal tau PET in ageing and Alzheimer's disease.* Brain, 2018. **141**(5): p. 1517-1528.
102. Beauchamp, M.H., et al., *Detecting traumatic brain lesions in children: CT versus MRI versus susceptibility weighted imaging (SWI).* Journal of neurotrauma, 2011. **28**(6): p. 915-927.
103. Karch, C.M., A.T. Jeng, and A.M. Goate, *Calcium phosphatase calcineurin influences tau metabolism.* Neurobiology of Aging, 2013. **34**(2): p. 374-386.
104. Prvulovic, D. and H. Hampel, *Amyloid β (Aβ) and phospho-tau (p-tau) as diagnostic biomarkers in Alzheimer's disease.* Clinical chemistry and laboratory medicine, 2011. **49**(3): p. 367-374.
105. Stokes, L., H. Combes, and G. Stokes, *The dementia diagnosis: a literature review of information, understanding, and attributions.* Psychogeriatrics, 2015. **15**(3): p. 218-225.
106. Gomes, C.S.F. and E.A.F. Silva, *Health Benefits and Risks of Minerals: Bioavailability, Bio-Essentiality, Toxicity, and Pathologies*, in *Minerals latu sensu and Human Health: Benefits, Toxicity and Pathologies*, C. Gomes and M. Rautureau, Editors. 2021, Springer International Publishing: Cham. p. 81-179.
107. Tran, D., et al., *Iron and Alzheimer's Disease: From Pathology to Imaging.* Frontiers in Human Neuroscience, 2022. **16**.
108. Brini, M., et al., *Intracellular calcium homeostasis and signaling.* Metallomics and the Cell, 2013: p. 119-168.
109. Cascella, R. and C. Cecchi, *Calcium dyshomeostasis in Alzheimer's disease pathogenesis.* International journal of molecular sciences, 2021. **22**(9): p. 4914.
110. Peng, T.I. and M.J. Jou, *Oxidative stress caused by mitochondrial calcium overload.* Annals of the New York Academy of Sciences, 2010. **1201**(1): p. 183-188.
111. Orrenius, S., et al., *Calcium ions and oxidative cell injury.* Annals of Neurology: Official Journal of the American Neurological Association and the Child Neurology Society, 1992. **32**(S1): p. S33-S42.
112. Fantoni, E.R., et al., *Design, synthesis and evaluation in an LPS rodent model of neuroinflammation of a novel 18 F-labelled PET tracer targeting P2X7.* EJNMMI research, 2017. **7**: p. 1-12.
113. Tarkin, J.M., et al., *Detection of atherosclerotic inflammation by 68Ga-DOTATATE PET compared to [18F] FDG PET imaging.* Journal of the American College of Cardiology, 2017. **69**(14): p. 1774-1791.
114. Bos, D., et al., *Atherosclerotic calcification relates to cognitive function and to brain changes on magnetic resonance imaging.* Alzheimer's & Dementia, 2012. **8**: p. S104-S111.
115. Hagberg, G.E., et al., *Diffusion properties of conventional and calcium-sensitive MRI contrast agents in the rat cerebral cortex.* Contrast Media & Molecular Imaging, 2014. **9**(1): p. 71-82.
116. Wu, Z., et al., *Identification of calcification with MRI using susceptibility-weighted imaging: a case study.* Journal of Magnetic Resonance Imaging: An Official Journal of the International Society for Magnetic Resonance in Medicine, 2009. **29**(1): p. 177-182.

117. LaFerla, F.M., *Calcium dyshomeostasis and intracellular signalling in Alzheimer's disease.* Nature Reviews Neuroscience, 2002. **3**(11): p. 862-872.
118. Mattson, M.P., et al., *Comparison of the effects of elevated intracellular aluminum and calcium levels on neuronal survival and tau immunoreactivity.* Brain research, 1993. **602**(1): p. 21-31.
119. Müller, W.E., et al., *Inorganic polymeric phosphate/polyphosphate as an inducer of alkaline phosphatase and a modulator of intracellular Ca2+ level in osteoblasts (SaOS-2 cells) in vitro.* Acta Biomaterialia, 2011. **7**(6): p. 2661-2671.
120. Yoshikuni, Y., et al., *Effect of phosphoproteins on intracellular calcification of bacteria.* European Journal of Oral Sciences, 2023. **131**(3): p. e12929.
121. Newton, A.C., *Protein kinase C: structure, function, and regulation.* Journal of biological chemistry, 1995. **270**(48): p. 28495-28498.
122. Tsolaki, E., et al., *Nuclear and cellular, micro and nano calcification in Alzheimer's disease patients and correlation to phosphorylated Tau.* Acta Biomaterialia, 2022. **143**: p. 138-144.
123. Chen, F., P.W. Tillberg, and E.S. Boyden, *Expansion microscopy.* Science, 2015. **347**(6221): p. 543-548.
124. Peter J. Goodhew, J.H., *Electron Microscopy and Analysis*. 2000, London: CRC Press.
125. Schöll, M., et al., *Biomarkers for tau pathology.* Molecular and Cellular Neuroscience, 2019. **97**: p. 18-33.
126. Furcila, D., et al., *Subregional density of neurons, neurofibrillary tangles and amyloid plaques in the hippocampus of patients with Alzheimer's disease.* Frontiers in neuroanatomy, 2019. **13**: p. 99.
127. Kosaka, K., *Diffuse neurofibrillary tangles with calcification: a new presenile dementia.* Journal of Neurology, Neurosurgery & Psychiatry, 1994. **57**(5): p. 594-596.
128. Bading, H., *Nuclear calcium signalling in the regulation of brain function.* Nature Reviews Neuroscience, 2013. **14**(9): p. 593-608.
129. Matsuda, H., Y. Shigemoto, and N. Sato, *Neuroimaging of Alzheimer's disease: focus on amyloid and tau PET.* Japanese journal of radiology, 2019. **37**: p. 735-749.
130. Bazin, D., et al., *Characterization and some physicochemical aspects of pathological microcalcifications.* Chemical Reviews, 2012. **112**(10): p. 5092-5120.
131. Everett, J., et al., *Nanoscale synchrotron X-ray speciation of iron and calcium compounds in amyloid plaque cores from Alzheimer's disease subjects.* Nanoscale, 2018. **10**(25): p. 11782-11796.
132. Ashraf, A., et al., *Pattern of altered plasma elemental phosphorus, calcium, zinc, and iron in Alzheimer's disease.* Scientific reports, 2019. **9**(1): p. 3147.
133. Xia, Q., et al., *Phosphoproteomic analysis of human brain by calcium phosphate precipitation and mass spectrometry.* Journal of proteome research, 2008. **7**(7): p. 2845-2851.
134. Sugiura, A., M. Kitamura, and Y. Hasegawa, *Calcium carbonate supplementation causes motor dysfunction.* Experimental Animals, 2022. **71**(3): p. 399-410.
135. Ehmann, W., et al., *Brain trace elements in Alzheimer's disease.* Neurotoxicology, 1986. **7**(1): p. 195-206.

136. Tyczyńska, M., et al., *Trace elements in Alzheimer's disease and dementia: the current state of knowledge.* Journal of clinical medicine, 2024. **13**(8): p. 2381.
137. Schlieper, G., et al., *Ultrastructural analysis of vascular calcifications in uremia.* Journal of the American Society of Nephrology, 2010. **21**(4): p. 689-696.
138. Chin, D.D., et al., *Hydroxyapatite-binding micelles for the detection of vascular calcification in atherosclerosis.* Journal of Materials Chemistry B, 2019. **7**(41): p. 6449-6457.
139. Wu, M., C. Rementer, and C.M. Giachelli, *Vascular Calcification: An Update on Mechanisms and Challenges in Treatment.* Calcified Tissue International, 2013. **93**(4): p. 365-373.
140. Azari, F., et al., *Intracellular precipitation of hydroxyapatite mineral and implications for pathologic calcification.* Journal of structural biology, 2008. **162**(3): p. 468-479.
141. Schinke, T., M.D. McKee, and G. Karsenty, *Extracellular matrix calcification: where is the action?* Nature genetics, 1999. **21**(2): p. 150-151.
142. Contreras, L., et al., *Mitochondria: the calcium connection.* Biochimica et Biophysica Acta (BBA)-Bioenergetics, 2010. **1797**(6-7): p. 607-618.
143. El-Hattab, A.W. and F. Scaglia, *Mitochondrial cytopathies.* Cell Calcium, 2016. **60**(3): p. 199-206.
144. Drut, R., R.M. Drut, and M.A. Greco, *Massive myocardial calcification in the perinatal period.* Pediatric and Developmental Pathology, 1998. **1**(5): p. 366-374.
145. Millane, T., et al., *Mitochondrial calcium deposition in association with cyclosporine therapy and myocardial magnesium depletion: a serial histologic study in heart transplant recipients.* The Journal of heart and lung transplantation: the official publication of the International Society for Heart Transplantation, 1994. **13**(3): p. 473-480.
146. Lee, M., et al., *Malakoplakia of the gastrointestinal tract: clinicopathologic analysis of 23 cases.* Diagnostic Pathology, 2020. **15**: p. 1-5.
147. Teplitz, C., *Malakoplakia: pathogenesis and ultrastructural morphogenesis: a problem of altered macrophage (phagolysosomal) response.* Human pathology, 1974. **5**(2): p. 191-207.
148. Colbran, R.J. and A.M. Brown, *Calcium/calmodulin-dependent protein kinase II and synaptic plasticity.* Current opinion in neurobiology, 2004. **14**(3): p. 318-327.
149. Veis, A. and J.R. Dorvee, *Biomineralization mechanisms: a new paradigm for crystal nucleation in organic matrices.* Calcified tissue international, 2013. **93**(4): p. 307-315.
150. Stein-Behrens, B., et al., *Stress exacerbates neuron loss and cytoskeletal pathology in the hippocampus.* Journal of Neuroscience, 1994. **14**(9): p. 5373-5380.
151. Salminen, A., et al., *ER stress in Alzheimer's disease: a novel neuronal trigger for inflammation and Alzheimer's pathology.* Journal of neuroinflammation, 2009. **6**: p. 1-13.
152. Mudher, A., et al., *What is the evidence that tau pathology spreads through prion-like propagation?* Acta neuropathologica communications, 2017. **5**(1): p. 99.

153. Baino, F. and S. Yamaguchi, *The use of simulated body fluid (SBF) for assessing materials bioactivity in the context of tissue engineering: review and challenges.* Biomimetics, 2020. **5**(4): p. 57.
154. Bohner, M. and J. Lemaitre, *Can bioactivity be tested in vitro with SBF solution?* Biomaterials, 2009. **30**(12): p. 2175-2179.
155. Russell, R., et al., *Calcium in mineralized tissues and pathological calcification.* British medical bulletin, 1986. **42**(4): p. 435-446.
156. Rolls, E.T., *Limbic systems for emotion and for memory, but no single limbic system.* cortex, 2015. **62**: p. 119-157.
157. Andersen, P., et al., *The hippocampus book*. 2006: Oxford university press.
158. Wegiel, J., et al., *Vascular fibrosis and calcification in the hippocampus in aging, Alzheimer disease, and Down syndrome.* Acta Neuropathologica, 2002. **103**(4): p. 333-343.
159. Donzuso, G., et al., *Basal ganglia calcifications (Fahr's syndrome): related conditions and clinical features.* Neurological sciences, 2019. **40**: p. 2251-2263.
160. Adams, L.C., et al., *Diagnostic performance of susceptibility-weighted magnetic resonance imaging for the detection of calcifications: A systematic review and meta-analysis.* Scientific Reports, 2017. **7**(1): p. 15506.
161. Catafau, A.M. and S. Bullich, *Amyloid PET imaging: applications beyond Alzheimer's disease.* Clinical and translational imaging, 2015. **3**: p. 39-55.
162. Rungby, J., et al., *The von Kossa reaction for calcium deposits: silver lactate staining increases sensitivity and reduces background.* The Histochemical Journal, 1993. **25**: p. 446-451.
163. Symonds, D.A., *Use of the von Kossa stain in identifying occult calcifications in breast biopsies.* American journal of clinical pathology, 1990. **94**(1): p. 44-48.
164. Schneider, M.R., *Von Kossa and his staining technique.* Histochemistry and cell biology, 2021. **156**(6): p. 523-526.
165. Kayani, I., et al., *A comparison of 68Ga-DOTATATE and 18F-FDG PET/CT in pulmonary neuroendocrine tumors.* Journal of Nuclear Medicine, 2009. **50**(12): p. 1927-1932.
166. Pauleit, D., et al., *Comparison of 18F-FET and 18F-FDG PET in brain tumors.* Nuclear medicine and biology, 2009. **36**(7): p. 779-787.
167. Chen, I.H., W. Yang, and M.A. Meyers, *Alligator osteoderms: mechanical behavior and hierarchical structure.* Mater Sci Eng C Mater Biol Appl, 2014. **35**: p. 441-8.
168. Burns, A., et al., *The effects of donepezil in Alzheimer's disease–results from a multinational Trial1.* Dementia and geriatric cognitive disorders, 1999. **10**(3): p. 237-244.
169. Shigeta, M. and A. Homma, *Donepezil for Alzheimer's disease: pharmacodynamic, pharmacokinetic, and clinical profiles.* CNS Drug Reviews, 2001. **7**(4): p. 353-368.
170. Pathak, C. and U.D. Kabra, *A comprehensive review of multi-target directed ligands in the treatment of Alzheimer's disease.* Bioorganic Chemistry, 2024. **144**: p. 107152.
171. Vaz, M. and S. Silvestre, *Alzheimer's disease: Recent treatment strategies.* European Journal of Pharmacology, 2020. **887**: p. 173554.
172. Scott, L.J. and K.L. Goa, *Galantamine: a review of its use in Alzheimer's disease.* Drugs, 2000. **60**: p. 1095-1122.

173. Muir, J.L., *Acetylcholine, aging, and Alzheimer's disease.* Pharmacology Biochemistry and Behavior, 1997. **56**(4): p. 687-696.
174. Van Gool, W., P. Aisen, and P. Eikelenboom, *Anti-inflammatory therapy in Alzheimer's disease: is hope still alive?* Journal of neurology, 2003. **250**: p. 788-792.
175. *Bisphosphonates*, in *Bisphosphonates in Medical Practice: Actions — Side Effects — Indications — Strategies*, R. Bartl, et al., Editors. 2007, Springer Berlin Heidelberg: Berlin, Heidelberg. p. 33-70.
176. Shaw, N.J. and N.J. Bishop, *Bisphosphonate treatment of bone disease.* Archives of Disease in Childhood, 2005. **90**(5): p. 494-499.
177. Hare, D.J., et al., *Lead and manganese levels in serum and erythrocytes in Alzheimer's disease and mild cognitive impairment: results from the Australian Imaging, Biomarkers and Lifestyle Flagship Study of Ageing†.* Metallomics, 2016. **8**(6): p. 628-632.
178. Zhou, W., et al., *Fundamentals of scanning electron microscopy (SEM)*, in *Scanning microscopy for nanotechnology: techniques and applications*. 2006, Springer. p. 1-40.
179. Mohammed, A. and A. Abdullah. *Scanning electron microscopy (SEM): A review*. in *Proceedings of the 2018 international conference on hydraulics and pneumatics—HERVEX, Băile Govora, Romania*. 2018.
180. Vernon-Parry, K.D., *Scanning electron microscopy: an introduction.* III-Vs review, 2000. **13**(4): p. 40-44.
181. Cazaux, J., *Recent developments and new strategies in scanning electron microscopy.* Journal of microscopy, 2005. **217**(1): p. 16-35.
182. *SEM vs TEM*. Technology Networks Analysis and Separations. Jan 24, 2024; Available from: https://www.technologynetworks.com/analysis/articles/sem-vs-tem-331262.
183. Akhtar, K., et al., *Scanning electron microscopy: Principle and applications in nanomaterials characterization*, in *Handbook of materials characterization*. 2018, Springer. p. 113-145.
184. Leamy, H., *Charge collection scanning electron microscopy.* Journal of Applied Physics, 1982. **53**(6): p. R51-R80.
185. Kannan, M., *Scanning electron microscopy: Principle, components and applications.* A textbook on fundamentals and applications of nanotechnology, 2018: p. 81-92.
186. Mehta, R., *Interactions, imaging and spectra in SEM*. 2012: INTECH Open Access Publisher.
187. Cazaux, J., *From the physics of secondary electron emission to image contrasts in scanning electron microscopy.* Journal of electron microscopy, 2012. **61**(5): p. 261-284.
188. Seiler, H., *Secondary electron emission in the scanning electron microscope.* Journal of Applied Physics, 1983. **54**(11): p. R1-R18.
189. Zhang, X., et al., *Simultaneous scanning electron microscope imaging of topographical and chemical contrast using in-lens, in-column, and everhart–thornley detector systems.* Microscopy and Microanalysis, 2016. **22**(3): p. 565-575.
190. Griffin, B.J., *A comparison of conventional Everhart-Thornley style and in-lens secondary electron detectors—a further variable in scanning electron microscopy.* Scanning, 2011. **33**(3): p. 162-173.

191. Lloyd, G.E., *Atomic number and crystallographic contrast images with the SEM: a review of backscattered electron techniques.* Mineralogical Magazine, 1987. **51**(359): p. 3-19.
192. Koga, D., et al., *Applications of scanning electron microscopy using secondary and backscattered electron signals in neural structure.* Frontiers in neuroanatomy, 2021. **15**: p. 759804.
193. Tsolaki, E., et al., *Density-Dependent Colour Scanning Electron Microscopy (DDC-SEM). Applications in the study of calcified tissues and visual impact.* bioRxiv, 2024: p. 2024.09. 16.613182.
194. Girão, A.V., G. Caputo, and M.C. Ferro, *Application of scanning electron microscopy–energy dispersive X-ray spectroscopy (SEM-EDS)*, in *Comprehensive analytical chemistry*. 2017, Elsevier. p. 153-168.
195. Allen, L.J., et al., *Chemical mapping at atomic resolution using energy-dispersive x-ray spectroscopy.* MRS bulletin, 2012. **37**(1): p. 47-52.
196. Mishra, R.K., A.K. Zachariah, and S. Thomas, *Energy-dispersive X-ray spectroscopy techniques for nanomaterial*, in *Microscopy methods in nanomaterials characterization*. 2017, Elsevier. p. 383-405.
197. Echlin, P., *Handbook of sample preparation for scanning electron microscopy and X-ray microanalysis*. 2011: Springer Science & Business Media.
198. Mehdizadeh, K.A., et al., *How to prepare biological samples and live tissues for scanning electron microscopy (SEM).* 2014.
199. Goldstein, J.I., et al., *Coating and conductivity techniques for SEM and microanalysis*, in *Scanning Electron Microscopy and X-Ray Microanalysis: A Text for Biologists, Materials Scientists, and Geologists*. 1992, Springer. p. 671-740.
200. Evans, J.E. and N.D. Browning, *Enabling direct nanoscale observations of biological reactions with dynamic TEM.* Microscopy, 2013. **62**(1): p. 147-156.
201. Kannan, M., *Transmission electron microscope—principle, components and applications.* A textbook on fundamentals and applications of nanotechnology, 2018: p. 93-102.
202. Orlova, E., *Principles of TEM image formation.* 2004.
203. Weirich, T.E., et al., *Structures of nanometre-size crystals determined from selected-area electron diffraction data.* Foundations of Crystallography, 2000. **56**(1): p. 29-35.
204. Pennycook, S.J. and P.D. Nellist, *Scanning transmission electron microscopy: imaging and analysis*. 2011: Springer Science & Business Media.
205. Stevenson, H.P., et al., *Use of transmission electron microscopy to identify nanocrystals of challenging protein targets.* Proceedings of the National Academy of Sciences, 2014. **111**(23): p. 8470-8475.
206. Zuo, J., et al., *Coherent nano-area electron diffraction.* Microscopy research and technique, 2004. **64**(5-6): p. 347-355.
207. Tizro, P., C. Choi, and N. Khanlou, *Sample preparation for transmission electron microscopy.* Biobanking: methods and protocols, 2018: p. 417-424.
208. Arnold, S.A., et al., *Miniaturizing EM sample preparation: opportunities, challenges, and "visual proteomics".* Proteomics, 2018. **18**(5-6): p. 1700176.
209. Pawley, J., *Handbook of Biological Confocal Microscopy*. 2006: Springer US.
210. Grienberger, C. and A. Konnerth, *Imaging calcium in neurons.* Neuron, 2012. **73**(5): p. 862-885.
211. Fine, A., et al., *Confocal microscopy: applications in neurobiology.* Trends in neurosciences, 1988. **11**(8): p. 346-351.

212. Frost, B., R.L. Jacks, and M.I. Diamond, *Propagation of tau misfolding from the outside to the inside of a cell.* Journal of biological chemistry, 2009. **284**(19): p. 12845-12852.
213. Reilly, W.M. and C.J. Obara, *Advances in Confocal Microscopy and Selected Applications*, in *Confocal Microscopy: Methods and Protocols*, J. Brzostowski and H. Sohn, Editors. 2021, Springer US: New York, NY. p. 1-35.
214. *Institute for Molecular Bioscience – University of Queensland.* [cited 2025 19 July]; Available from: https://imb.uq.edu.au/microscopy-confocal
215. Gratton, E. and M.J. VandeVen, *Laser sources for confocal microscopy*, in *Handbook of biological confocal microscopy*. 2006, Springer. p. 53-67.
216. Denk, W., D.W. Piston, and W.W. Webb, *Two-photon molecular excitation in laser-scanning microscopy*, in *Handbook of biological confocal microscopy*. 1995, Springer. p. 445-458.
217. Spibey, C.A., P. Jackson, and K. Herick, *A unique charge-coupled device/xenon arc lamp based imaging system for the accurate detection and quantitation of multicolour fluorescence.* Electrophoresis, 2001. **22**(5): p. 829-836.
218. Donaldson, J.G., *Immunofluorescence staining.* Current protocols in cell biology, 2015. **69**(1): p. 4.3. 1-4.3. 7.
219. Miller, D.M. and D.C. Shakes, *Immunofluorescence microscopy.* Methods in cell biology, 1995. **48**: p. 365-394.
220. Kienberger, F., et al., *Single molecule studies of antibody–antigen interaction strength versus intra-molecular antigen stability.* Journal of molecular biology, 2005. **347**(3): p. 597-606.
221. Zaqout, S., L.-L. Becker, and A.M. Kaindl, *Immunofluorescence staining of paraffin sections step by step.* Frontiers in neuroanatomy, 2020. **14**: p. 582218.
222. Benesty, J., et al., *Pearson correlation coefficient*, in *Noise reduction in speech processing*. 2009, Springer. p. 1-4.
223. Sedgwick, P., *Pearson's correlation coefficient.* Bmj, 2012. **345**.
224. Ali Abd Al-Hameed, K., *Spearman's correlation coefficient in statistical analysis.* International Journal of Nonlinear Analysis and Applications, 2022. **13**(1): p. 3249-3255.
225. De Winter, J.C., S.D. Gosling, and J. Potter, *Comparing the Pearson and Spearman correlation coefficients across distributions and sample sizes: A tutorial using simulations and empirical data.* Psychological methods, 2016. **21**(3): p. 273.
226. Nachar, N., *The Mann-Whitney U: A test for assessing whether two independent samples come from the same distribution.* Tutorials in quantitative Methods for Psychology, 2008. **4**(1): p. 13-20.
227. Zimmerman, D.W., *Comparative power of Student t test and Mann-Whitney U test for unequal sample sizes and variances.* The Journal of Experimental Education, 1987. **55**(3): p. 171-174.
228. Oyane, A., et al., *Preparation and assessment of revised simulated body fluids.* Journal of Biomedical Materials Research Part A: An Official Journal of The Society for Biomaterials, The Japanese Society for Biomaterials, and The Australian Society for Biomaterials and the Korean Society for Biomaterials, 2003. **65**(2): p. 188-195.